

11/83
JULY 1983

Indian J Pure & Appl Phys, Vol 21 No. 7 pp 383-434

CODEN: IJQPAU ISSN: 0019-5596
21(7) 383-434 (1983)

INDIAN JOURNAL OF PURE & APPLIED PHYSICS



Published by
PUBLICATIONS & INFORMATION DIRECTORATE, CSIR
NEW DELHI
in association with
THE INDIAN NATIONAL SCIENCE ACADEMY, NEW DELHI

EC-85

Programmable Desk-top Computing System



Combines conventional algebraic language and flexible programmability to meet the computation needs of professionals

An engineer, a statistician, an economist, a finance executive, a scientist — the computation needs of each may be different from the others. EC 85, a powerful desk-top computing system featuring conventional algebraic language and flexible programmability, is specially designed to meet a wide range of challenging computation problems confronted by professionals. The basic system comprises the complete scientific and statistical keyboard, a display, a printer and powerful programmable facility up to 2000 programme steps and 200 memory data registers. What's more, it's compatible with a wide range of peripherals. And fully open for expansion in respect of programme steps and data registers. In short, it's a system that can suitably expand and keep pace with your expanding computation needs and requirements.

Salient features:

- Easy-to-use key step programme technique
- Expandable up to 6000 steps and 700 data registers
- Provided with 9 different types of jump options
- Facility for programme debugging
- A wide range of options and peripherals



Electronics Corporation of India Limited

(A Govt. of India — Dept. of Atomic Energy—Enterprise)

INSTRUMENTS GROUP — MARKETING, HYDERABAD 500 762.

Tel: 78311 Telex: 0155 - 254 ECIL HD.

Branches: BANGALORE BOMBAY CALCUTTA MADRAS NEW DELHI

Phones: 77072 4227760 240273 442339 311007

Indian Journal of Pure & Applied Physics

EDITORIAL BOARD

Prof. D Basu
Indian Association for
the Cultivation of Science
Calcutta

Prof. B Buti
Physical Research Laboratory
Ahmedabad

Prof. S C Dutta Roy
Indian Institute of Technology
New Delhi

Dr R Hradaynath
Instruments Research & Development
Establishment Dehra Dun

Prof. D Premaswarup
Nagarjuna University
Nagarjuna Nagar

Prof. A N Mitra
Indian National Science Academy
New Delhi/University of Delhi
Delhi

Prof. Probir Roy
Tata Institute of Fundamental
Research
Bombay

Prof. E S Raja Gopal
Indian Institute of Science
Bangalore

Prof. G Rajasekaran
Madras University
Madras

Dr A P B Sinha
National Chemical Laboratory
Pune

Prof. C V Vishveshwara
Raman Research Institute
Bangalore

Prof. M S Sodha
Indian National Science Academy
New Delhi/Indian Institute of
Technology New Delhi

Shri Y.R. Chadha, Editor-in-Chief, *Ex-officio Secretary*

EDITORIAL STAFF

Editors

D S Sastry, K S Rangarajan & R P Goel

Assistant Editors

G N Sarma, J B Dhawan & Tarun Banerjee

Scientific Assistant

(Mrs) Poonam Bhatt

Published by the Publications & Information Directorate, CSIR, Hillside Road, New Delhi 110 012

Editor-in-Chief : Y R Chadha

The Indian Journal of Pure & Applied Physics is issued monthly. The Directorate assumes no responsibility for the statements and opinions advanced by contributors. The editorial staff in its work of examining papers received for publication is assisted, in an honorary capacity, by a large number of distinguished scientists, working in various parts of India.

Communications regarding contributions for publication in the journal should be addressed to the Editor, Indian Journal of Pure & Applied Physics, Publications & Information Directorate, Hillside Road, New Delhi 110012.

Correspondence regarding subscriptions and advertisements should be addressed to the Sales & Distribution Officer, Publications & Information Directorate, New Delhi 110012.

Annual Subscription
Rs. 120.00 £20.00 \$45.00

Single Copy
Rs. 12.00 £2.00 \$4.50

50% Discount is admissible to research workers and students and 25% discount to non-research individuals, on annual subscription. Payments in respect of subscriptions and advertisements may be sent by cheque, bank draft, money order or postal order marked payable *only* to **Publications & Information Directorate, New Delhi 110 012**. Claims for missing numbers of the journal will be allowed only if received within 3 months of the date of issue of the journal plus the time normally required for postal delivery of the journal and the claim.

Announcement

XIII International Conference on Quantum Electronics

(18-21 June 1984)

The Thirteenth International Quantum Electronics Conference (IQEC-84) sponsored by the American Physical Society will be held during 18-21 June 1984 at the Anaheim Mariott Hotel and Anaheim Convention Center, Anaheim, California, USA, along with the 4th Conference on Lasers and Electro-Optics (CLEO-84) organized by the Optical Society of America and the Quantum Electronics & Applications Society of IEEE, USA. These conferences will be composed of plenary, invited, contributed, poster and post-deadline papers and special symposia on specific topics.

Original papers reporting new technical advances to the areas covered by the technical sessions are invited and the author is expected to submit a 35-word abstract and 200-500 word summary before 6 Jan 1984. Full details regarding format for the abstract and the paper and about the technical sessions can be had from:

Optical Society of America
1816 Jefferson Place N.W.
Washington DC 20036
(202) 223-8130 USA

Indian Journal of Pure & Applied Physics

VOLUME 21

NUMBER 7

JULY 1983

CONTENTS

Solid State Physics

Performance of Silicon Surface Barrier Detectors (*p*- & *n*-Type) under Identical Quenchants.
Postetch Ambients and Encapsulation
A K Batra*

Effect of Additives and Dopants on the Growth of KDP Crystals 388
 Kolluri V Ramanajah* & K B Varma

Lateral Self-Diffusion in Indium Thin Films 391
J J B Prasad & K V Reddy*

Behaviour of Large-grain Polycrystalline *n*-InP Grown by SSD Technique 395
J N Roy, S Basu*, D N Bose & A J Singh

Chemical Physics

Conductivity of Magnesium Valerate Solutions in Binary Liquid Mixtures 398
S N Gour, Umesh Kumar & R P Varma*

Excitation of Hydrogen Atom to the $n=2$ State by Helium-Ion Impact 401
 Shyamal Datta, Kanika Roy & S C Mukherjee*

Mathematical & Theoretical Physics

Nonperturbative Solutions for Screened Coulomb Potentials 404
 A P Kajiwadkar & J K Sharma*

Random Electrodynamics of Nonlinear System: Part I—Quartic Anharmonic Oscillator 408
S. Sachidanandam & J. V. V. Raghavacharyulu*

Spectroscopy

Evaluation of Spectroscopic Parameters for the Pr^{3+} Ion in a Laser Liquid 413
 S. V. J. Lakshman* & S. Buddhudu

NOTES

Effect of Thickness on the Electrical Properties of AlSb Thin Films 418
 S. M. Patel & A. M. Biradar*

Thickness Dependence of Electrical Resistivity of Vacuum-deposited Selenium Films 420

Preparation of Multialkali Antimonide Photocathode 422
 R. J. Verma* & R. C. Bapna

CONTENTS

Modified Gell-Mann-Okubo Mass Formula in the (8.8) Model T N Tiwari*, C V Sastry & (Mrs) Saroj Sharma	425
Charmed Baryon Magnetic Moments in Broken SU(8) Model K P Tiwari & C P Singh*	427
EPR of Cu ²⁺ in MgSeO ₄ .6 H ₂ O Single Crystals V K Jain	430
Twyman Green Interferometer with Curved Mirrors M V R K Murty & R P Shukla*	432
Papers Accepted for Publication	434

The author to whom all correspondence is to be addressed is indicated by the () mark.

Performance of Silicon Surface Barrier Detectors (*p*- & *n*-Type) under Identical Quenchants, Postetch Ambients and Encapsulation

A K BATRA*

Department of Physics, Haryana Agricultural University, Regional Campus, Kaul 132021 (Kurukshetra)

Received 12 October 1981; revised received 7 June 1983

p- & *n*-Type silicon surface barrier detectors (*p*-SSBD & *n*-SSBD) have been fabricated by varying the three significant parameters viz., quenchants, postetch ambients and encapsulations. Postetch exposures of two days' duration to deionized water for *n*-type and that to dust-free air for *p*-type have been found essential for SSBD technology. Quenchant experimentations lead to their ranking in decreasing order of superiority as HNO_3 , H_2O , HF in *n*-SSBD and HNO_3 , HF, H_2O in *p*-SSBD. Stain film left as a result of quenching appears to have excess of chemisorbed fluoride group. Encapsulation of edges and free rear surface both in *p*- and *n*-SSBD reduces the leakage current. It has been applied prior to ambient exposure in *p*-SSBD and after this exposure in *n*-SSBD. Leakage currents of less than $1 \times 10^{-8}\text{ A}$ (*n*-SSBD) and $2 \times 10^{-8}\text{ A}$ (*p*-SSBD) have been obtained for reverse biases up to 100 V. The sample detectors yield energy resolutions of 30 keV fwhm (*n*-SSBD) and 50 keV fwhm (*p*-SSBD) for 5.47 MeV α -particles. Results indicate dominant dependence of SSBD technology on chemisorbed water and oxygen coverages at different stages of fabrication.

1 Introduction

Interfacial layers on silicon produced as a result of chemisorption are the decisive factor in SSBD technology. Quenchant, postetch ambients and encapsulation are the three fabrication parameters which control the composition and thickness of these layers and hence the detector response. Considerable investigations have been attempted on *n*-SSBD with reports suggesting a number of contradictory schedules. Successful barrier formations on *p*-type silicon have also been reported¹⁻⁴ but detailed scientific explanation is not attempted in them. It is felt that comparative evaluations of these fabrication parameters on *p*- and *n*-type silicon will afford a reliable technique to probe into the unresolved problems, besides leading to optimization of fabrication schedules of these detectors.

1.1 Quenchant

Etching and quenching leaves the first residual layer called stain film, the composition and thickness of which seem to be controlled by the quenchant. Deionized water has been commonly used as quenchant for *n*-SSBD but its universality is questioned by Goradia⁵ who claimed that HF and HNO_3 quenchings, too, produce good detectors. Archer's results⁶ indicate that this stain film consists of restructured silicon or silicon hydride and their thickness lies in the range 10-20 Å for HNO_3 and 100-200 Å for H_2O quenchants. Still thicker films are claimed⁵ to be present when quenched in HF. Goradia⁵ assumed the chemistry of this film to be as above and correlated their increasing thickness with improvement in detector response. Hence the

superiority of quenchants in decreasing order as advanced by him is HF, H_2O , HNO_3 for *n*-SSBD. Clansenn⁷, however, predicted this stain film to be consisting of some chemisorbed fluoride group. Walter and Boshart⁸ correlated stain film presence to deterioration in *n*-SSBD and suggested its removal by surface treatments. Obviously, this reasoning would lead to complete reversal of quenchant rankings advanced by Goradia⁵. So this controversy needs investigation as the results will suggest the best suited quenchant, besides establishing the chemistry of the stain film. In case of *p*-SSBD it is HNO_3 which is universally accepted as quenchant¹⁻⁴, but the explanation for this has not been attempted in these reports. The relative superiorities of other quenchants and the influence of this stain film are yet to be explored for *p*-SSBD.

1.2 Postetch Ambients

These are characterized by the gases and vapours present in atmosphere or to which the etched specimens are exposed intentionally. In *n*-SSBD some reports suggest a definite improvement in the quality when the specimens are exposed to either water or dust free air. But the controversy exists regarding the stage at which these exposures are to be given. Goradia⁵ claims that only the postetch exposure to moisture is sufficient whereas Siffert and Coche⁹ emphasize the necessity of post-evaporation exposures to air only. In view of this controversy and the attempted encapsulations at different stages, the study of these exposures becomes necessary. In case of *p*-SSBD, the postetch exposures to atmosphere or deionized water are reported to be minimized^{1,3,4}. However, thick

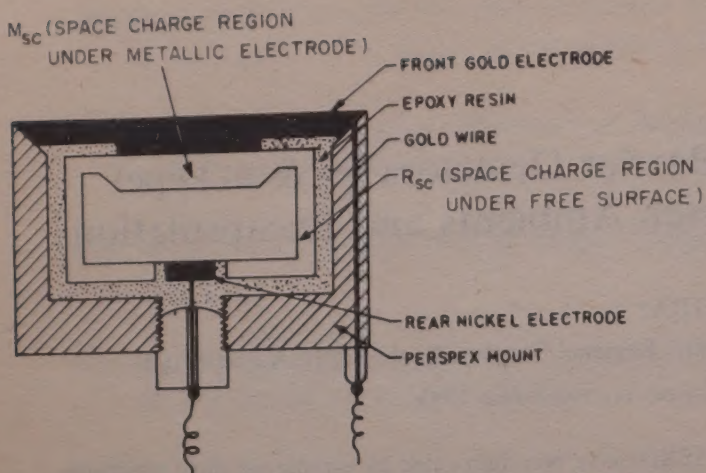


Fig. 1—Metal-silicon surface barrier detector

oxygen coverages on *p*-type silicon at this stage have been obtained by some workers, viz. Mathew *et al.*¹ by HNO_3 at quenching stage, Maksimov *et al.*² by storage in discharge tube and Protsenko *et al.*³ by treating it with HNO_3 . These coverages can also be obtained by exposing the surface to dry and dust-free air. Our attempt has been to evaluate the utility of such an exposure for different quenchants and different encapsulations.

1.3 Encapsulation

A major source of leakage current in SSBD is the surface leakage current. It flows due to the shunt path provided by the two space charge regions, i.e. one under the front metallic electrode (M_{sc}) characterized by diffusion potential V_d and the other under free surface, i.e. edges and rear side (R_{sc}) characterized by surface potential V_s (Fig. 1). Reports have appeared regarding control of this current either by encapsulation¹⁰ or by certain surface treatments⁵. It is claimed⁵ that in *n*-SSBD if the M_{sc} - R_{sc} junction is reverse biased by keeping $|V_d|$ larger than $|V_s|$, then the difference $|V_d - V_s|$ controls this leakage current. In the present work attempts have been made to incorporate both the encapsulation technique and the postetch exposures to suitable ambients for minimizing this current in *n*-SSBD. Reports so far do not mention encapsulation to *p*-SSBD; so investigations have been made to test its utility in them also. Ambient sensitivity of completed detectors is well known. The role of encapsulation in its control has also been explored.

2 Experimental Details

From 10 $\text{k}\Omega\text{-cm}$ resistivity silicon of $\langle 111 \rangle$ orientation, round slices of surface area 3 cm^2 and thickness 1 mm were obtained. The same ingot was used to ensure identical bulk properties. Lapped slices were nickel plated to obtain back contact by soldering tinned copper wire. The slice was cleaned in ultrasonic trichloroethylene (Electronic Grade) bath followed by

thorough rinse in deionized water. Hence three different procedures were adopted to test the utility of encapsulation. The first (E_1) consisted in encapsulating the entire back portion, the edges and the small periphery of the front of the specimen in picine. These portions were thus protected from etching. In the second technique (E_2), these portions of specimen were exposed to etching. But encapsulation was applied to *p*-type wafer just after etching whereas for *n*-type it was employed after postetch ambient exposure. In the third procedure (E_3), the completed detector i.e. after the front metallic evaporation, was mounted on perspex disc by using picine at the small periphery of the rear side and thus most of the R_{sc} region was kept exposed to laboratory ambients. The results indicated the superiority of E_2 over other procedures and so it was followed in the present work.

The specimen was then etched in CP-4A etchant with acids of electronic grade. Quenchings were carried out separately for different samples by gradual addition of each of the quenchants HF, HNO_3 and deionized water. The specimen at this stage was flushed inside the etching solution by a stream of deionized water and was thereafter thoroughly rinsed in it. For studying the influence of ambients, identically quenched *n*-type specimen were subjected to minimum possible exposure to any ambient, one day exposure to dust-free air and exposures to deionized water for different durations. The deionized water was changed six hourly. The postetch exposure schedule selected for *p*-type specimen was: (a) minimum possible, (b) one day to deionized water and (c) to dry and dust-free air for different durations. Gold was then vacuum evaporated for front contact in both *p*- and *n*-type specimens. *I-V* characteristics were recorded using a Phillips GM 6020 microvoltmeter and employing short-shielded cables. Some of the detectors were tested in α -spectroscopy experimentation. Resolution curves using a thin and uniform ^{241}Am source were plotted at 10^{-2} Torr pressure for N_2 and P_3 detectors at 30 V reverse bias.

3 Results

3.1 *n*-Type Silicon Surface Barrier Detectors

Fig. 2 incorporates the reverse characteristics of these detectors quenched by different agents. Leakage currents below 10^{-8} A up to 100 V reverse bias were obtained both for HNO_3 - and H_2O -quenched detectors. HF quenching led to poor detectors as these recorded threefold larger leakage currents, besides breaking down at low bias of 50 V. HNO_3 appears to be the best suited quenchant. These results indicate superiority of the quenchants in decreasing order as HNO_3 , H_2O , HF. Fig. 3 displays the strong

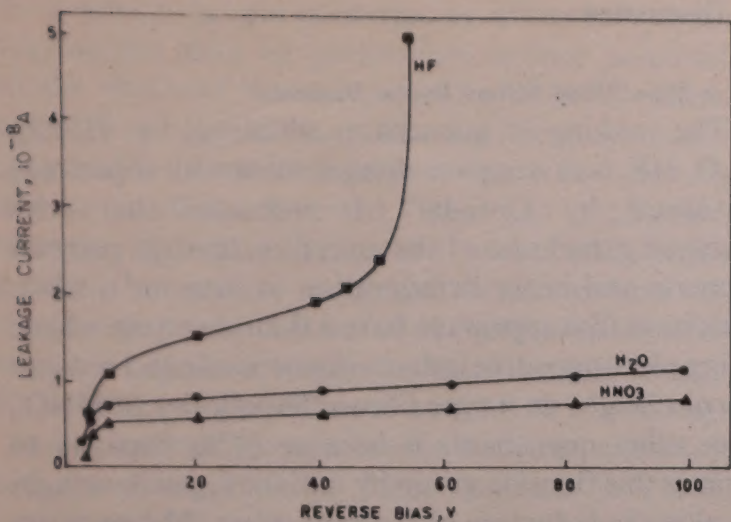


Fig. 2—Reverse characteristics of *n*-SSBD under different quenchants

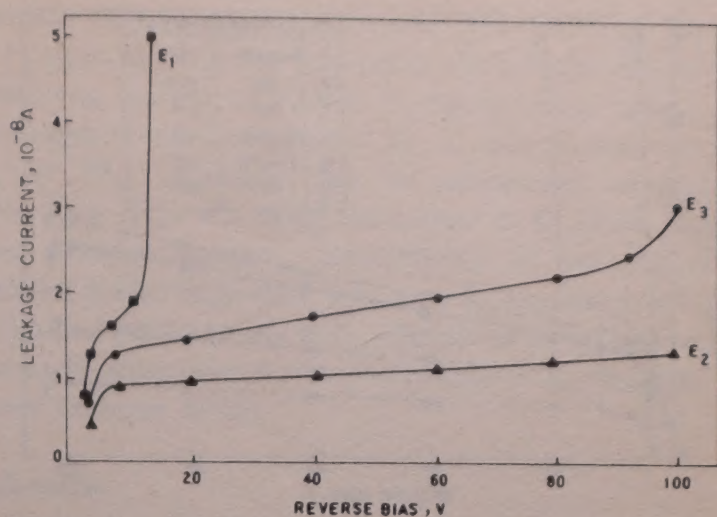


Fig. 4—Reverse characteristics of *n*-SSBD under different encapsulation procedures

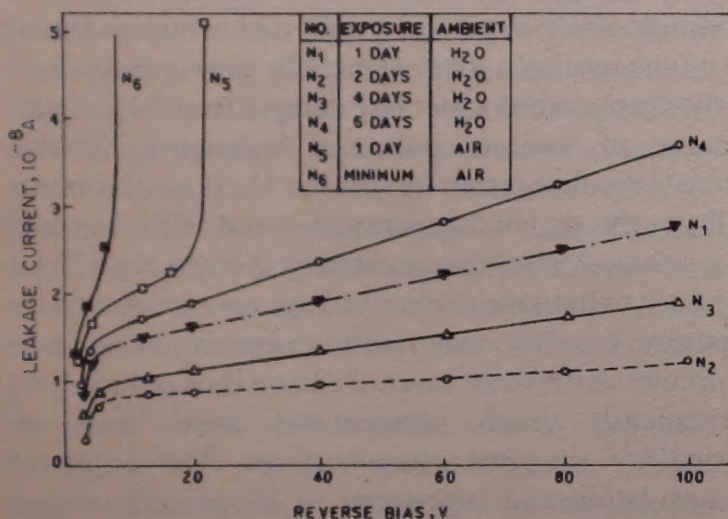


Fig. 3—Reverse characteristics of *n*-SSBD under different ambient schedules

dependence of detector *I-V* characteristics on postetch exposures. Samples in which either this exposure is minimized (N_6) or it is to dry atmosphere (N_5), very weak barriers are formed. The leakage currents observed were of the order of $10^{-7} A$ at 20 V in N_5 and $10^{-7} A$ at 5 V in N_6 . Prolonged exposure to deionized water (N_3 and N_4), too, caused deterioration thus necessitating the optimization of exposure period. The best characteristics were obtained for two days postetch exposure to deionized water (N_2) yielding leakage current less than $10^{-8} A$ for reverse bias up to 100 V. It appears to be an essential step for *n*-SSBD fabrication.

The comparative characteristics of different encapsulation procedures are illustrated in Fig. 4. Encapsulation of edges and rear portion prior to etching (E_1) exhibited marked deterioration ($i \sim 10^{-7} A$ at 10 V) when compared to other techniques. However, of the other two it was second procedure (E_2) which exhibited the lowest leakage current, i.e. less than $10^{-8} A$ up to 100 V. Further, the increase in reverse current on exposure to vacuum was observed

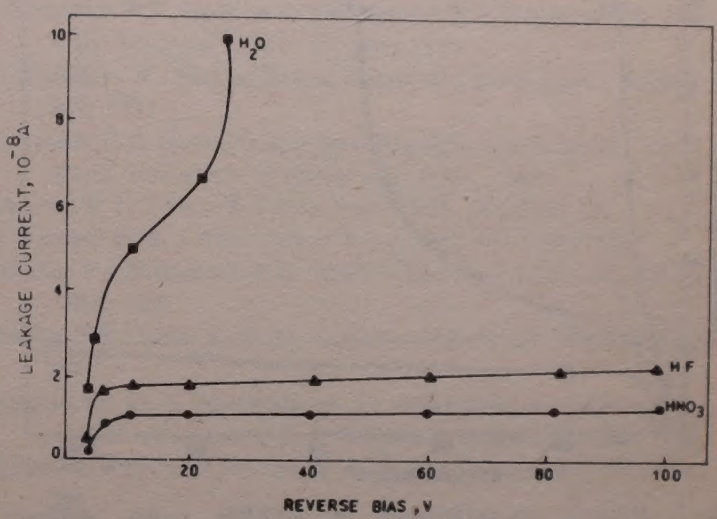


Fig. 5—Reverse characteristics of *p*-SSBD under different quenchants

to be appreciably checked in second procedure (E_2) over others. Hence encapsulation of rear and edges of *n*-type silicon after postetch exposure improves both the reverse characteristics and the ambient insensitivity..

3.2 p-Type Silicon Surface Barrier Detectors

Typical reverse characteristics of *p*-SSBD under different quenchants are illustrated in Fig. 5. No barrier appears to be formed in H_2O quenched sample. Leakage currents of less than $2 \times 10^{-8} A$ were recorded up to 100 V reverse bias for both HNO_3 and HF quenched samples. Of these two, HNO_3 quenched detector exhibited smaller leakage current indicating the ranking of the quenchants in *p*-SSBD as HNO_3, HF, H_2O . Influence of ambient variation schedule on leakage current is represented in Fig. 6. Detector formed with minimum postetch exposure to any ambient (P_1) was of poor quality, recording leakage current of the order of $10^{-7} A$ at 20 V reverse bias. Exposure to deionized water (P_2) damaged the barrier formation on *p*-type silicon contrary to the case

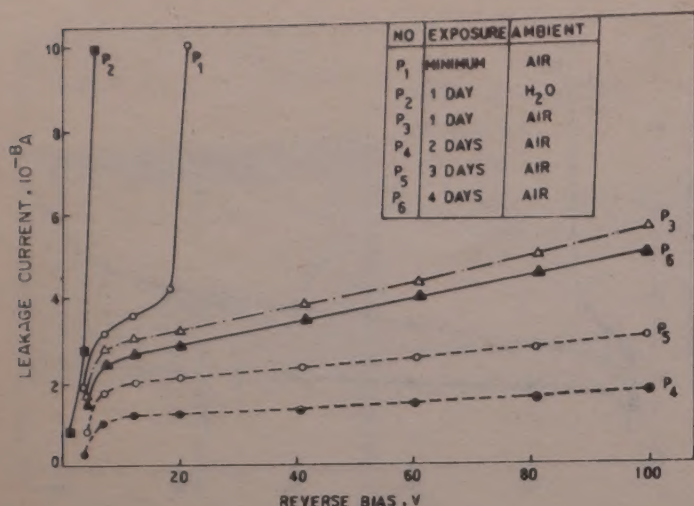


Fig. 6—Reverse characteristics of *p*-SSBD under different ambient schedules

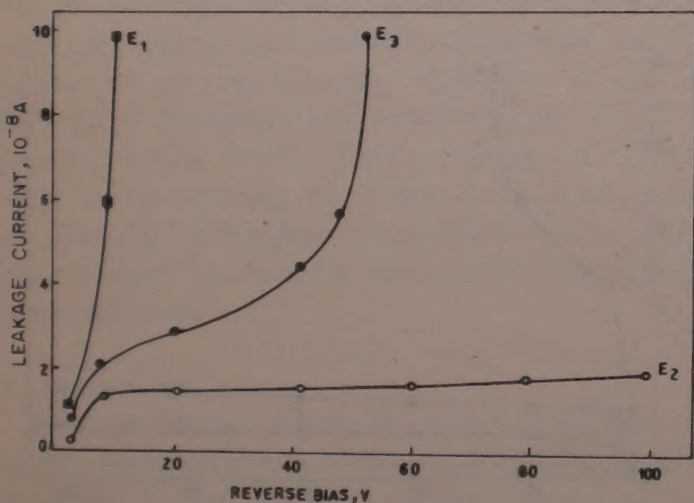


Fig. 7—Reverse characteristics of *p*-SSBD under different encapsulation procedures

of *n*-type silicon. Improvements were observed with increasing exposures to dry air. Deterioration was marked when this period exceeded two days. Hence the optimized two days' exposure to dry and dust-free air appears a suitable substitute to the other procedures of oxidation. Results of encapsulation experiment on *p*-SSBD are consistent with those obtained on *n*-SSBD; (Fig. 7). The first procedure (E₁) did not produce a barrier at all. Of the other two, the second (E₂) appears to be the best suited as it recorded leakage current less than 2×10^{-8} A up to 100 V, whereas in E₃ it exceeded 1×10^{-7} A even at 50 V reverse bias. Second procedure (E₂) also enhanced the ambient insensitivity of the completed detector. Thus encapsulation of rear and edges of the sample improves performance of *p*-SSBD if it is applied just after etching. In *n*-SSBD it was employed after the postetch exposure.

α -Spectroscopy results indicate energy resolutions of 30 keV fwhm (N₂ detector) and 50 keV fwhm (P₃ detector) for 5.47 MeV α -particles at the source-to-detector spacing of 3 cm and at 30 V reverse bias. Thus performance of both *p*- and *n*-SSBD fabricated by optimized schedules was reasonably good.

4 Discussion

4.1 *n*-Type Silicon Surface Barrier Detectors

The ranking of quenchants obtained, i.e. HNO₃, H₂O, HF, is in complete disagreement with superiority advanced by Goradia⁵. It indicates that with increasing thickness of the stain film, leakage currents increase and hence deterioration in detector quality. This stain film appears to have a fluoride group which, being electropositive induces donor levels and reduces barrier height on *n*-type silicon. Superiority of HNO₃ over other quenchants is because of its capacity to replace this fluoride group by initial oxygen coverages resulting in induction of acceptor states. The necessity of postetch exposure to deionized water is consistent with the results of Goradia⁵. This leads to water chemisorption on entire silicon surface which is known to induce donor levels and reduce the surface potential on *n*-type specimen. During metallic evaporation most of the chemisorbed water is dislodged from M_{sc} region because of vacuum pull and impinging metallic atoms¹¹ resulting in an increase in V_d. It cannot occur in R_{sc} as this region is encapsulated and so the reduced V_s is retained. Thus the condition |V_d| larger than |V_s| is obtained to limit the surface leakage current. Excessive exposure, however, may result in penetration of water molecules in the oxide layer of silicon thus reducing V_d permanently. Such penetrations have been reported^{12,13} on germanium surfaces. The utility of encapsulation and superiority of E₂ procedure over others is also easily understood on the above model. Both in E₂ and E₃ the rear and the edges are exposed to deionized water but in E₁ these are encapsulated in picine prior to the exposure. So reduction of V_s does not occur in E₁. Superiority of E₂ over E₃ is because in the former the chemisorbed water from free surface cannot be dislodged during evaporation due to encapsulation, but in the latter the desorption of water from this region does take place because of vacuum pull. So the reduction of V_s attained due to ambient schedule is retained in E₂ while in E₃ it undergoes an increase thus enhancing the leakage current. Finally the ambient insensitivity of completed detector, too, is improved in E₂ over E₃ because the reduced V_s in the former cannot be altered by any ambient exposure. V_s of R_{sc} region in E₃ is, however, prone to changes due to displacement of water by the oxygen atoms as most of R_{sc} is not encapsulated.

4.2 *n*-Type Silicon Surface Barrier Detectors

Previous discussion on *n*-SSBD predicts the ranking of quenchants in *p*-SSBD as HF, H₂O, HNO₃, because the density of donor levels induced should be a function of the thickness of stain film. But the observed ranking, i.e. HNO₃, HF, H₂O, can be justified if the

role of thicker oxygen coverages on silicon is studied. Experimental data on germanium surface potential and the observed deterioration of *n*-SSBD by thick oxygen coverages² indicate that the initial coverages enhance the overall acceptor character thereby reducing surface potential, and the additional coverages introduce donor-like states and hence increase the surface potential. This reversal of character may be attributed to the following: (a) The additional oxygen coverages produce complex oxides with binding energies different from covalent bonding. It causes redistribution of surface charge and may result into donor levels. (b) Silicon surfaces have both acceptor and donor-like impurities, though the former is richer in *p*-type. The observed predominant diffusion of acceptor-like impurity atoms from surface to oxide-gas interface may leave the surface with relatively larger donor-like impurity. (c) Impurities incorporated during growth of oxides also introduce intermediate donor-like states¹⁴. Hence the superiority of quenchants in *p*-SSBD is determined by its capacity to produce oxygen coverages. But the detector formation by HF quenching, though of poorer quality than HNO₃-quenched sample, supports that stain film has a fluoride group which, being quite thick in this case, induces sufficient donor levels for formation of a barrier.

The need of postetch exposures to dry air also becomes obvious as it results in thick oxygen coverages. The result on encapsulation, too, can be justified on the above. Encapsulation prior to etching (E₁) does not involve initial oxygen coverages for reduction of V_s in R_{sc}. In E₃ the entire specimen is exposed for oxygen coverages; so both V_d and V_s

increase during postetch exposure. The difference |V_d - V_s| does not increase and hence the leakage current cannot be limited. In E₂ low V_s due to initial oxygen coverages is retained because R_{sc} is encapsulated but V_d in M_{sc} increases due to additional oxygen coverages. |V_d - V_s|, being the largest in E₂, yields the least leakage current. Insensitivity of completed detector is also improved in E₂ over E₃ because low V_s is retained permanently in E₂ whereas in E₃ it changes due to displacement of adsorbed atoms of R_{sc} by more active ambient atoms.

References

- 1 Mathew P J, Chapman N G & Coote G E, *Nucl Instrum & Methods (Netherlands)*, **49** (1967) 245.
- 2 Maksimov Y S, Rodinov Y F & Yavlinskii Y N, *Sov Phys Semicond (USA)*, **1** (1968) 867.
- 3 Protsenko A V, Sinitsyn V N, Pensenko N V & Korol V M, *Sov Phys Semicond (USA)*, **3** (1969) 1118.
- 4 Chaudhary R, *Bhabha Atomic Research Centre Report, BARC-527*, 1971.
- 5 Goradia C P, *Surface states and the gold-n-silicon barrier*, Ph D thesis, University of Oklahoma, USA, 1968.
- 6 Archer R J, *J Phys & Chem Solids (GB)*, **14** (1960) 104.
- 7 Clansenn B H, *J Electrochem Soc (USA)*, **111** (1964) 646.
- 8 Walter F J & Boshart R R, *IEEE Trans Nucl Sci (USA)*, **NS-13** (1966) 189.
- 9 Siffert P & Coche A, *IEEE Trans Nucl Sci (USA)*, **NS-12** (1965) 284.
- 10 Dearnaley G & Northrop D C, *Semiconductor counters for nuclear radiations* (E & F N Spon, London), 2nd Edn, 1966.
- 11 Gibbons P E, *Nucl Instrum & Methods (Netherlands)*, **29** (1964) 289.
- 12 Lasser M, Wysocki C & Bernstein B, *Phys Rev (USA)*, **105** (1957) 491.
- 13 Wallmark J T & Johnson R R, *RCA Rev (USA)*, **18** (1957) 512.
- 14 Atalla M M, Tannenbaum E & Scheibner E J, *Bell Syst Tech J (USA)*, **38** (1959) 749.

Effect of Additives and Dopants on the Growth of KDP Crystals

KOLLURI V RAMANAIAH* & K B R VARMA

Department of Physics, PSG College of Technology, Coimbatore 641 004

Received 17 May 1982; revised received 17 March 1983

The effect of addition of borax, nickel phosphate (NiPO_4), manganese phosphate [$\text{Mn}_3(\text{PO}_4)_2$], sodium dihydrogen orthophosphate (NaH_2PO_4) and potassium arsenate on the growth characteristics and growth habits of KDP crystals at room temperature (25 °C) has been studied. Single crystals of KDP with various concentrations of these additives have been grown by the Holden's rotary crystallizer (slow evaporation) technique. The crystals obtained are of excellent optical quality and of fairly large size. The relative importance of the addition of growth-aiding agents like borax to KDP has been brought out. The presence of the additives and dopants in the grown crystals has been detected by the chemical and the X-ray analyses.

1 Introduction

The various physical properties of the KDP-type crystals and their isomorphs which fit into the XH_2PO_4 group of electrooptic materials were explored thoroughly by a number of workers¹⁻³. However, the effect of dopants and additives on the growth characteristics, electrooptic and photoelastic properties of KDP crystals has not been studied in detail. Keeping in view that materials like borax, NiPO_4 , $\text{Mn}_3(\text{PO}_4)_2$, NaH_2PO_4 and potassium arsenate would have some effect on the growth characteristics, electrooptic and photoelastic properties of KDP crystals, the present study was taken up, and the results obtained are presented in this paper.

2 Growth of KDP with Borax

Brice⁴ suggested that borax could be used as a growth aid for KDP- and ADP-type crystals but did not give any details of the effect of borax on the growth rate and growth habit of KDP crystals. In order to study the effect of borax on the growth rate and growth habit of KDP and its isomorphs, a systematic study was initially made on the solubilities of both ADP and KDP in triple distilled water with various concentrations of borax at different temperatures⁵.

The characteristics of KDP were studied by taking three saturated solutions of KDP, each in 100 ml of triple distilled water containing 5, 10, 15 g borax and prepared at 36 °C. After cooling them to room temperature (25 °C) they were transferred to a set of 250 ml beakers. The temperature of the room (being a closed one) was fairly constant. KDP seed crystals of known dimensions were hung in all the three solutions and growth was allowed to take place by slow evaporation technique. The increase in length of the crystals along [001] (along Z-axis) was monitored periodically using a cathetometer arrangement. The results obtained are shown in Fig. 1. The following

conclusions were drawn from the growth rate along [001] of the crystal and by visual observation.

The growth rates for pure KDP and KDP containing 5 and 15 g borax in solution were almost same while the sample with 10 g borax had a higher growth rate. A small tapering was noticed in samples with 5 g borax whereas samples with 15 g borax did not show any tapering at all. In the case of samples with 10 g borax, the prism faces were observed to grow uniformly. The growth rates along other crystallographic axes (i.e. perpendicular to [001]) were high in the case of samples with 15 and 10 g borax compared to those of pure KDP samples. No significant difference was observed in the interfacial angles with 5 g borax and pure samples.

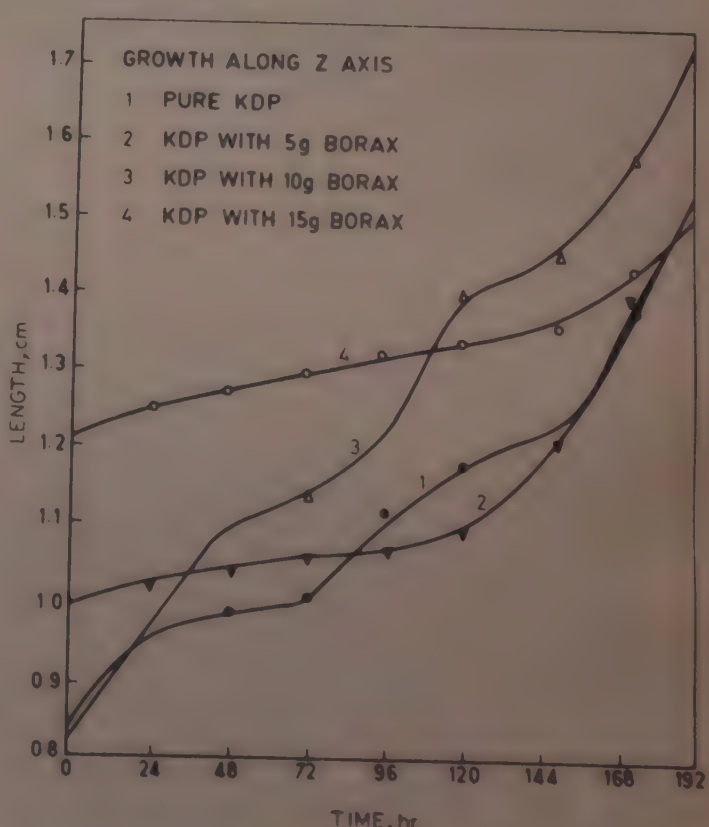


Fig. 1 Growth rates of pure KDP and KDP with borax crystals

KDP single crystals with 5, 10 and 15 g borax with excellent optical quality of dimensions $45 \times 12 \times 12$ mm were obtained using Holden's rotary crystallizer (slow evaporation) technique in a period of about 40 days.

3 Growth of KDP with Nickel Phosphate, Manganese Phosphate, Sodium Dihydrogen Orthophosphate and Potassium Arsenate

Byteva⁶ studied the effect of pH on the growth habit of ADP crystals in the presence of Fe^{3+} and Cr^{3+} and concluded that the solubility of FeCl_3 in saturated ADP solution at a given temperature is very much dependent on pH. Davey and Mullin⁷ studied the growth of (101) faces of ADP crystals in the presence of ionic species and indicated that Fe^{3+} ions get incorporated in the lattice. They suggested that a complex of the type $\text{Fe}(\text{H}_2\text{O})_4(\text{OH})_2^+$ is formed and occupies interstitial sites between two rows of H_2PO_4^+ ions parallel to the [010] direction of the (502), (701) and (702) faces. Torgesen and Jackson⁸ studied the action of Cr^{3+} on ADP and indicated the possibility of incorporation of the impurity along the growth fronts of the layers rather than by absorption on certain crystal planes. Fontanbera⁹, based on their Mössbauer studies, confirmed that Fe^{3+} ions do get into the lattice probably through the (0.25, 0.22, 0.12) and (0.75, 0.22, 0.12) sites.

Davey and Mullin⁷ reported the growth of ADP crystals in the presence of manganese ions; they discussed the effect of manganese ions on the growth rates of (010) faces. They explained the kinetic effect in terms of absorption of the Mn^{3+} complex and the interaction of this with the spiral growth process.

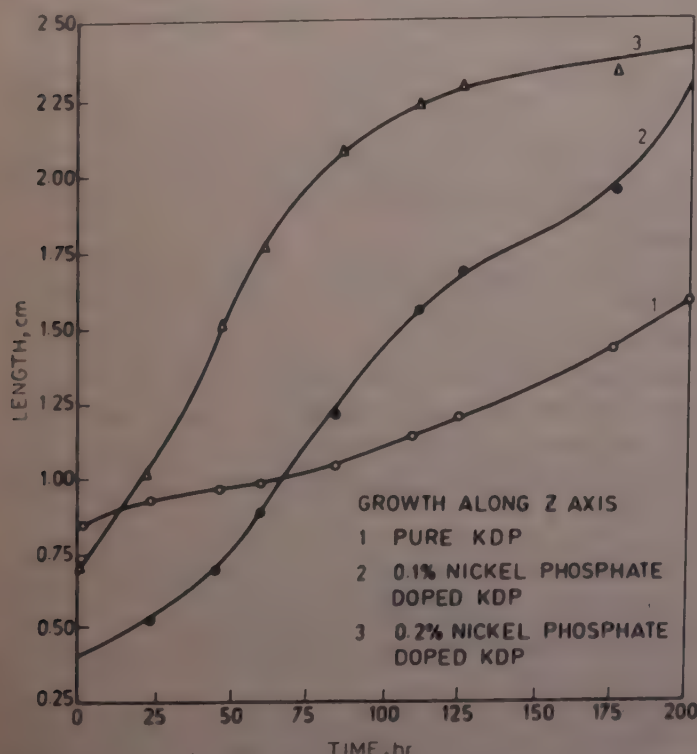


Fig. 2 - Growth rates of KDP and nickel phosphate doped KDP crystals

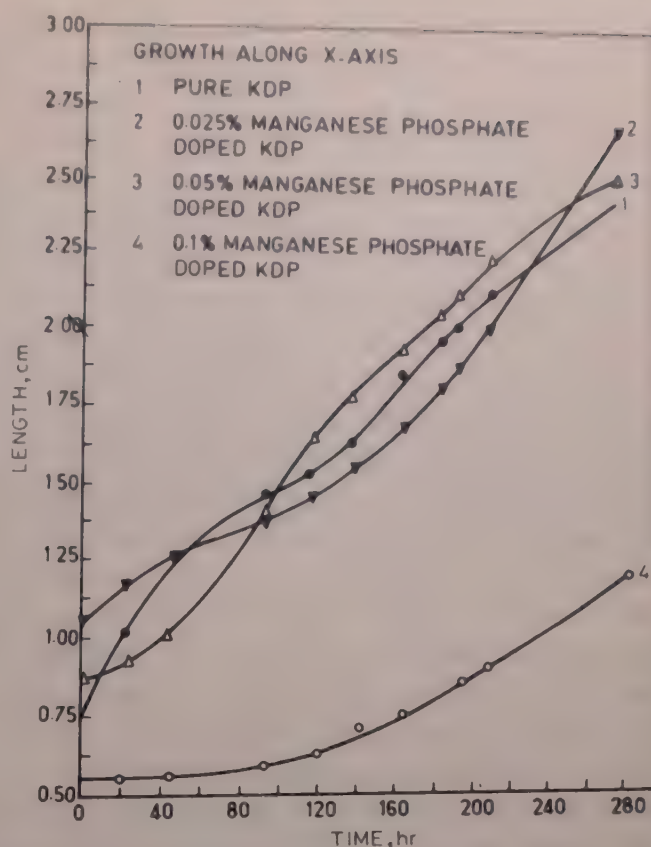


Fig. 3 - Growth rates of KDP and manganese phosphate doped KDP crystals

To study the effect of nickel phosphate (NiPO_4) on the growth characteristics of KDP, saturated solutions of KDP with 0.1 and 0.2% (by weight) NiPO_4 were prepared at 35°C. These solutions were allowed to cool down to 25°C. Seed crystals of KDP of known dimensions were introduced into the solutions. Then the crystals were allowed to grow by slow evaporation technique under controlled conditions. The growth rates of the crystals along [001] were monitored every 25 hr using the cathetometer arrangement. The results are presented in Fig. 2.

The growth rate along [001] was found to increase with the increase in concentration of NiPO_4 in KDP solution. The shapes of the pyramidal faces in the case of NiPO_4 doped samples were distorted and the interfacial angles decreased. It was observed that the tapering was severe in the case of 0.2% NiPO_4 doped KDP crystals. The tapering angle was found to increase with the ageing of the solution. In the case of 0.1% NiPO_4 doped KDP crystals, a small tapering was observed, but there was no substantial increase in the tapering angle with time. Attempts were made to study the effect of higher concentrations of NiPO_4 on growth characteristics of KDP crystals. However, it was found difficult to dissolve more than 0.2% NiPO_4 in KDP solution (100 ml) by mere addition and agitation.

Solutions of KDP containing 0.25, 0.05 and 0.1% (by weight) manganese phosphate [$\text{Mn}_3(\text{PO}_4)_2$] were prepared. A comparative study was made on the growth rates of the crystals, and the results are shown in Fig. 3. It is evident from Fig. 3 that except in the case

of 0.05% $Mn_3(PO_4)_2$, the growth rate of KDP decreased with the addition of the dopant. This result is quite contrary to that of $NiPO_4$ doped KDP crystals. The KDP crystals doped with higher than 0.1% $Mn_3(PO_4)_2$ had higher growth rate initially. But with the ageing of the solution, the growth completely ceased.

The effect of 1% (by weight) sodium dihydrogen orthophosphate (NaH_2PO_4) on the growth characteristics of KDP crystals was studied under the same conditions as above, and the following conclusions were drawn. There was no change in the growth rate of 1% NaH_2PO_4 added KDP crystals compared to pure KDP crystals along the X-axis. There was no significant change in the interfacial angles and growth of the pyramidal faces compared to those of pure KDP crystals. The growth rates of KDP crystals with small percentages of NaH_2PO_4 along the X- and the Y-directions were higher than those of pure KDP samples. Higher percentages of NaH_2PO_4 in KDP solutions resulted in polycrystalline aggregates.

Similarly, from the studies on 0.5% (by weight) potassium arsenate added KDP crystals, the following conclusions were drawn. The overall growth rates of KDP crystals with potassium arsenate were rather low compared to those of pure KDP crystals. No tapering was noticed in the growing samples. There was a small change in the growth habit of the pyramidal faces.

To study the linear electrooptic and photoelastic effects in these mixed crystals, one has to have sufficiently large-sized and good optical-quality crystals. The following procedure was adopted to grow such crystals.

Unsaturated solution of KDP was prepared in triple distilled water at 40°C. To this solution, 0.1% (by weight) $NiPO_4$ supplied by Sarabhai Chemicals was added and the solution was stirred until the whole amount of nickel phosphate was dissolved. The mixed solution was transferred to a glass tank in Holden's rotary crystallizer equipment. The temperature of the solution was kept at $35 \pm 0.05^\circ C$. The seed holder carrying KDP seed crystal was placed in the tank; special care was taken in preparing seed crystals. A moderately large and well developed flawless KDP seed crystal was selected. A basal plate was cut and washed with a few drops of distilled water. This plate was heated to the same temperature as that of the solution (i.e. 35°C) and hung by a thread from one of the branches of the seed holder. The seed holder was rotated at about 30 rpm. The small tapering observed in the growing crystal was minimized by periodically adding KOH pellets to the solution.

Excellent optical quality crystals of 0.1% (by weight) $NiPO_4$ doped KDP were grown (dimensions. 80 × 8 × 8 mm) over a period of about 70 days. By adopting the same technique, single crystals of KDP with

$NiPO_4$, 0.2% (by weight); NaH_2PO_4 , 1% (by weight); potassium arsenate, 0.5% (by weight); and $Mn_3(PO_4)_2$, 0.02% (by weight) were grown with dimensions (100 × 4 × 4 mm), (60 × 6 × 6 mm), (50 × 5 × 5 mm) and (50 × 4 × 4 mm) respectively.

4 Detection of the Presence of Dopants in the Grown Crystals

A qualitative determination of the presence of dopants was made by subjecting portions of the grown crystals to chemical analysis. By this method, the presence of borax, nickel, manganese and arsenate was confirmed in the corresponding doped crystals. The crystals were further subjected to X-ray analysis¹⁰ to study variation in the lattice parameters due to the presence of these ions. X-ray powder diffraction patterns of all the samples were obtained and variations in the lattice spacings as compared to pure KDP were observed. From the above observations, it was concluded that the additives had entered the host lattice of the grown crystals.

5 Conclusions

The KDP crystals grown with borax were generally large in size without any tapering, hard (as observed during grinding and polishing operations), less hygroscopic and exhibited very good optical qualities with minimal strains. The growth rate of KDP along [001] was very high in the presence of $NiPO_4$. This would imply that in order to obtain very large-sized KDP crystals, one could go in for $NiPO_4$ doping, even though there are some practical problems in obtaining strain-free and untapered crystals of KDP in the presence of $NiPO_4$.

Acknowledgement

The authors wish to record their appreciation of the valuable discussions they had with Prof. T S Narasimhamurthy, Department of Physics, Osmania University, Hyderabad. One of them (KBRV) is thankful to the University Grants Commission, New Delhi, for the Fellowship for carrying on this work.

References

- 1 Zwicker B & Scherrer P, *Helv Phys Acta (Switzerland)*, 17 (1979) 657.
- 2 Billing B H, *J Opt Soc Am (USA)*, 39 (1949) 802.
- 3 Carpenter R, *J Opt Soc Am (USA)*, 40 (1950) 225.
- 4 Brice J C, *The growth of crystals from liquids* (North Holland Publishing Co, London), 1973, 12.
- 5 Varma K B R & Ramanaiah Kolluri V, *Bull Mater Sci (India)*, 3 (1981) 307.
- 6 Byteva I M, *Growth of crystals*, edited by N N Shetiar, Translated from Russian by E S Bradley (Consultants Bureau, New York) SB (1968) 26.
- 7 Davey R I & Mullin J W, *J Cryst Growth (Netherlands)*, 23 (1974) 89.
- 8 Torgesen J C & Jackson R L, *Science (USA)*, 148 (1965) 952.
- 9 Fontenberta J, *J Cryst Growth (Netherlands)*, 44 (1978) 593.
- 10 Cullity B D, *Elements of X-ray diffraction* (Addison-Wesley, New York), 1978.

Lateral Self-Diffusion in Indium Thin Films

J J B PRASAD & K V REDDY*

Department of Physics, Indian Institute of Technology, Madras 600 036

Received 23 August 1982

Lateral self-diffusion has been studied in indium thin films. A thin-film sample with a well defined radioactive region in the middle was prepared by neutron activation technique. An experimental set-up was fabricated to scan the concentration of the radioactive indium in the sample. A non-linear fitting procedure was employed to determine the self-diffusion coefficient from the experimental data. The diffusion data obtained in the temperature range 93-145 °C could be fitted to the equation $D = 0.22 \exp(-0.60/kT)$. The thin-film data were compared with the available data on bulk indium. A grain boundary diffusion mechanism has been concluded for the lateral self-diffusion in indium thin films in the temperature range studied.

1 Introduction

With the increasing cost of materials, especially some of the metals due to their limited availability, it is vital to develop more and more thin film devices in microelectronics, solar cells and other types of transducers. Thin metallic films are also used for making inter-connections, protective layers, etc. In all the applications, the films are subjected to electric fields which sometimes may produce current densities greater than 10^4 A/cm^2 resulting in 'electromigration' of atoms. In some cases there may exist thermal gradients to cause thermomigration. In either case of mass transport, the migration depends on the fundamental diffusion processes involved.

In recent years, reliable data on the study of self-diffusion and inter-diffusion in thin films in normal direction have been reported using alpha particle back scattering¹, sputter ion mass spectrometers², Auger electron spectroscopy³ and radioactive tracer techniques⁴. Depth profiling by rf sputtering⁵ using radioactive tracers gives excellent results wherever it is applicable for determining the diffusion coefficient in the normal direction in thin films. It was pointed out by Gupta *et al.*⁶ that data available on lateral diffusion measurements in thin films are meagre. Beniere *et al.*⁷ determined the lateral diffusion coefficient of copper in aluminium thin films by a sectioning technique using radioactive tracers. Scanning of the radioactive tracer concentration is a non-destructive technique for studying lateral diffusion in thin films^{8,9}. Tai *et al.*¹⁰ employed this method to determine the lateral self-diffusion in tin thin films.

Dickey¹¹ studied the self-diffusion in indium single crystals using radioactive tracers and sectioning technique. Self-diffusion in polycrystalline indium was studied by Eckert and Drickamer¹². We are reporting in this paper the results of lateral self-diffusion in indium thin films studied by neutron activation combined with a tracer scanning technique.

2 Method

The schematic diagram of the sample used for obtaining the lateral self-diffusion coefficient is shown in Fig. 1(a). The shaded regions contain radioactive indium (^{114m}In) and the continuous stripe pattern is ordinary indium film. For obtaining the diffusion coefficients we have used an analysis technique somewhat similar to that used by Sun and Ohring¹³. Fig. 1(b) shows the ideal radioactive indium concentration profile of the sample before diffusion annealing when viewed through a slit of infinitely small width. From the fundamental diffusion laws, for the type of the configuration shown in Fig. 1(b), the radioactive concentration $C(x, t)$ at a distance x from

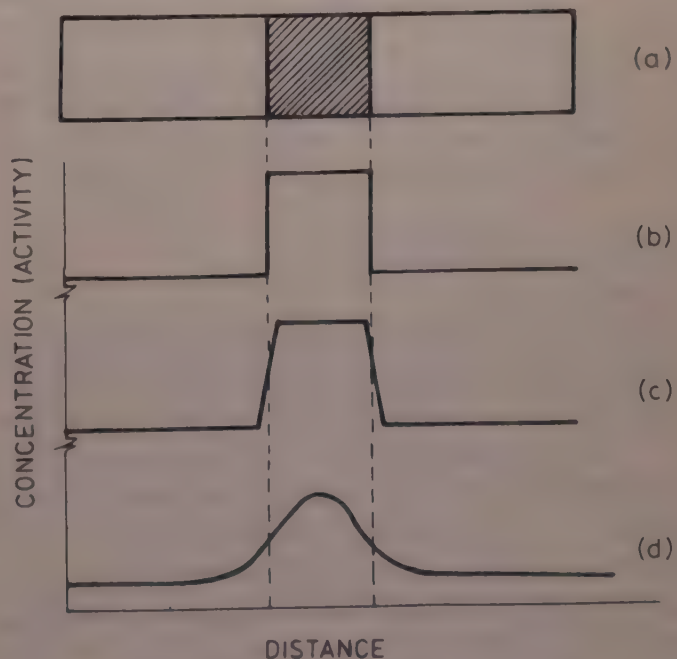


Fig. 1—Schematic diagram of the thin film sample used for diffusion studies [(a), shaded region contains radioactive indium; continuous stripe pattern is ordinary indium film; (b), ideal radioactive indium concentration profile of the sample before diffusion annealing if scanned by a slit of infinitely small width; (c), shape of the profile in (b) if scanned by a slit of finite width; and (d), shape of the radioactive indium concentration profile after diffusion annealing if scanned by a slit of finite width]

the centre of the radioactive region of width $2h$ after annealing for t sec is given by

$$C(x, t) = \frac{C_0}{2} \left[\operatorname{erf}\left(\frac{h+x}{2\sqrt{Dt}}\right) + \operatorname{erf}\left(\frac{h-x}{2\sqrt{Dt}}\right) \right] \quad \dots (1)$$

where C_0 is the activity at $x = 0$ and D the lateral diffusion coefficient.

To obtain the radioactive concentration profiles of the sample, we have placed an adjustable slit in between the detector and the sample mounted on a movable platform. Fig. 1(c) shows the shape of the concentration profile before diffusion annealing when scanned by a slit of finite width. Fig. 1(d) shows the shape of the profile after diffusion. Because of the large slit width ($50 \mu\text{m}$) employed in recording the tracer profiles, the experimentally observed concentration is $\bar{C}(x, t)$ corresponding to a region of finite width of the sample instead of $C(x, t)$ given by Eq. (1). $\bar{C}(x, t)$ can be derived from the true profile $C(x, t)$ as

$$\bar{C}(x, t) = \int_{|x - \frac{W}{2}|}^{x + \frac{W}{2}} C(x, t) dx \quad \dots (2)$$

where W is the width of the slit used in recording the profiles.

When $C(x, t)$ is substituted from Eq. (1), Eq. (2) becomes

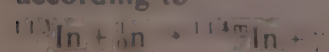
$$\bar{C}(x, t) = \frac{C_0}{2} \int_{(x - \frac{W}{2})}^{(x + \frac{W}{2})} \left[\operatorname{erf}\left(\frac{h+x}{2\sqrt{Dt}}\right) + \operatorname{erf}\left(\frac{h-x}{2\sqrt{Dt}}\right) \right] dx \quad \dots (3)$$

One can obtain D values by fitting the experimental data to Eq. (3) by a non-linear least squares fitting procedure. Statistical errors in recording the nuclear radiations have also been taken into account in writing the programme for fitting the experimental data in the present study. Since the slit widths used are large, the edge effects due to diffraction can be neglected.

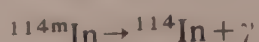
3 Experimental Details

3.1 Sample Preparation

Samples for diffusion studies were prepared in two stages. In the first stage 99.999% pure indium was evaporated in a vacuum coating unit at about 10^{-6} Torr on oxidized silicon single crystal substrates of $250 \mu\text{m}$ thickness. Indium was evaporated in the shape of $1 \times 3 \text{ mm}$ dot ($0.1 \mu\text{m}$ thick) through a contact mask prepared by photoetching techniques. A set of samples thus prepared were subjected to thermal neutron irradiation in a neutron flux of 10^{13} neutrons/ $\text{cm}^2\text{-sec}$ for one week in CIRUS reactor of the Bhabha Atomic Research Centre, Bombay. Relative abundance of ^{113}In isotope is 4.3% and its neutron absorption cross-section is 56 b. On neutron irradiation, ^{113}In converts to radioactive ^{114}mIn , according to



Radioactive ^{114}mIn decays to ^{114}In with a half-life of 50 days



^{114}In is a β emitter with a half-life of 72 sec



These β particles are detected for determining radioactive indium concentration.

After neutron irradiation, in the second stage, continuous $1 \mu\text{m}$ thick indium film of dimensions $7 \times 3 \text{ mm}$ was evaporated on the irradiated dot-shaped samples through another contact mask at about 10^{-6} torr vacuum. Both the contact masks were prepared in such a way that on evaporation through the second mask, the edge of the continuous ordinary film coincided with the edges of the radioactive indium dot as shown in Fig. 1(a).

3.2 Diffusion Annealing

Fig. 2 shows the annealing set-up for diffusion studies. Samples placed on a quartz sample holder were introduced into a quartz tube as shown in Fig. 2. The quartz tube was evacuated and flushed with argon several times and finally filled with argon up to $1/3$ atmospheric pressure. A furnace was designed specially for diffusion studies. A hollow metallic cylinder was placed inside the furnace into which the quartz tube containing the sample was introduced. This metallic block was used for avoiding temperature gradient along the length of the sample. Temperature of the furnace can be controlled to an accuracy of $\pm 0.2^\circ\text{C}$ by a PID (proportional, integral and derivative) temperature controller. Throughout the period of diffusion annealing the temperature of the furnace was monitored continuously on a strip chart recorder.

3.3 Tracer Concentration Profiling

Fig. 3 shows the tracer scanning arrangement used for obtaining the tracer concentration profiles. A precision scanning arrangement was fabricated to move the sample laterally. The least count of the system shown in Fig. 3 is $1 \mu\text{m}$. For recording the counts coming from a specified position of the sample, an adjustable slit was placed in between the sample and the detector. An organic scintillator was used as a detector for detecting β -radiations coming from the radioactive indium. A single channel analyzer was used for sorting out the pulses and for counting them. The detector has very low efficiency for detecting gamma rays. When β -rays coming from radioactive indium are detected, a thin adjustable slit of 0.2 cm thickness is sufficient for stopping the β -rays and minimizing the background contribution.

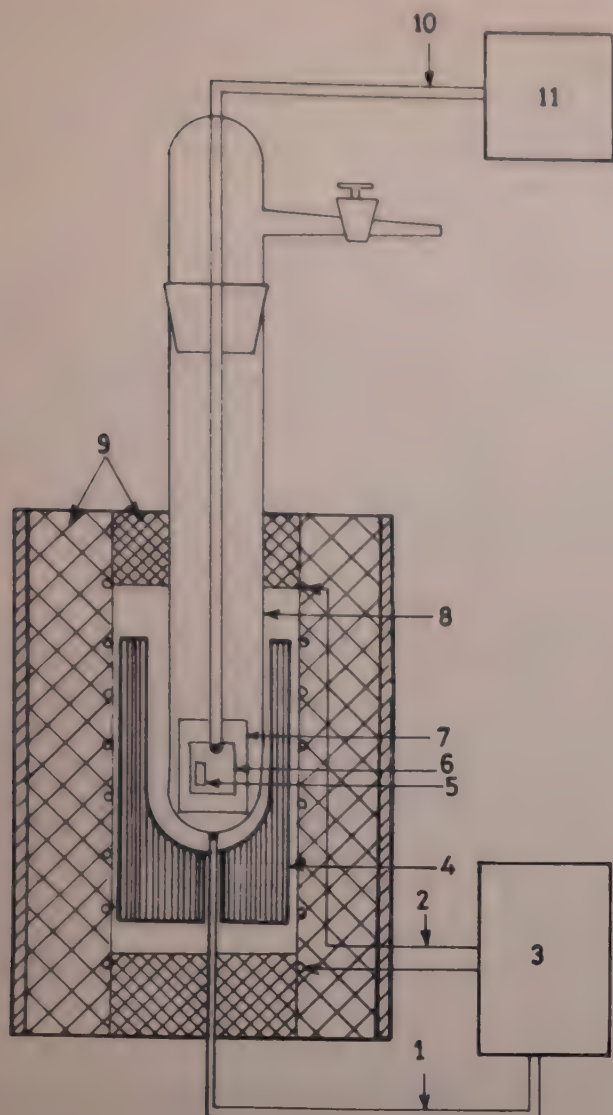


Fig. 2—Experimental set-up for diffusion annealing [1 and 10, thermocouples; 2, furnace coil; 3, temperature controller; 4, stainless steel block; 5, sample; 6, substrate; 7, sample holder; 8, quartz tube; 9, thermal insulator; and 11, digital temperature indicator]

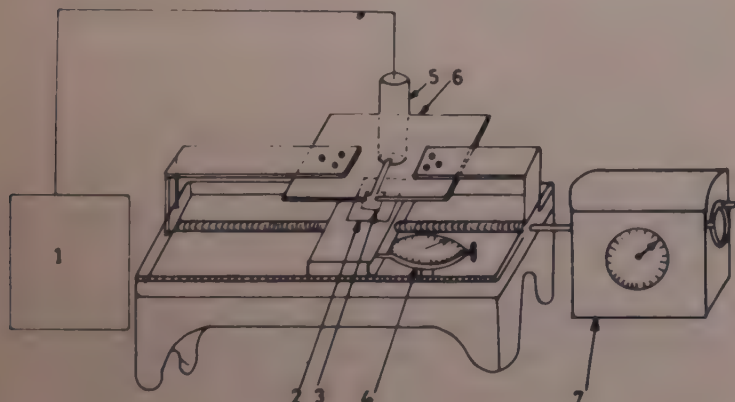


Fig. 3—Schematic diagram of tracer scanning arrangement (1, single channel analyzer; 2, sample holder; 3, sample; 4, dial gauge; 5, detector; 6, slit and 7, reduction gear box)

After diffusion annealing, samples were placed on a movable platform which can be moved laterally by the scanning arrangement. A slit of 50 μm width was used and the activity at every 50 μm distance along the length of the sample was determined. The best fit for the experimental data to Eq. (3), using IBM 370/155 computer, gave the tracer concentration profiles.

4 Results and Discussion

Fig. 4 shows the radioactive indium concentration profile of a sample annealed for 52 hr at 102°C. In Fig. 4, the continuous curve is the theoretical curve obtained by fitting the experimental data to Eq. (3); experimental points are shown by small circles. The fitted values of dot width and diffusion coefficient are 1 mm and $1.45 \times 10^{-9}\text{cm}^2/\text{sec}$ respectively. Diffusion experiments were performed at various temperatures in the range 93–145°C. The results are given in Table 1. The diffusion data obtained are found to obey the Arrhenius law with a single slope. The fitted values of the pre-exponential factor and activation energies are $(0.22 \pm 0.02)\text{ cm}^2/\text{sec}$ and $0.60 \pm 0.01\text{ eV}$ respectively.

Fig. 5 shows the comparison of our data with the self-diffusion data obtained by Dickey¹¹ and Eckert and Drickamer¹² in bulk indium. Dickey studied indium self-diffusion in single crystals using

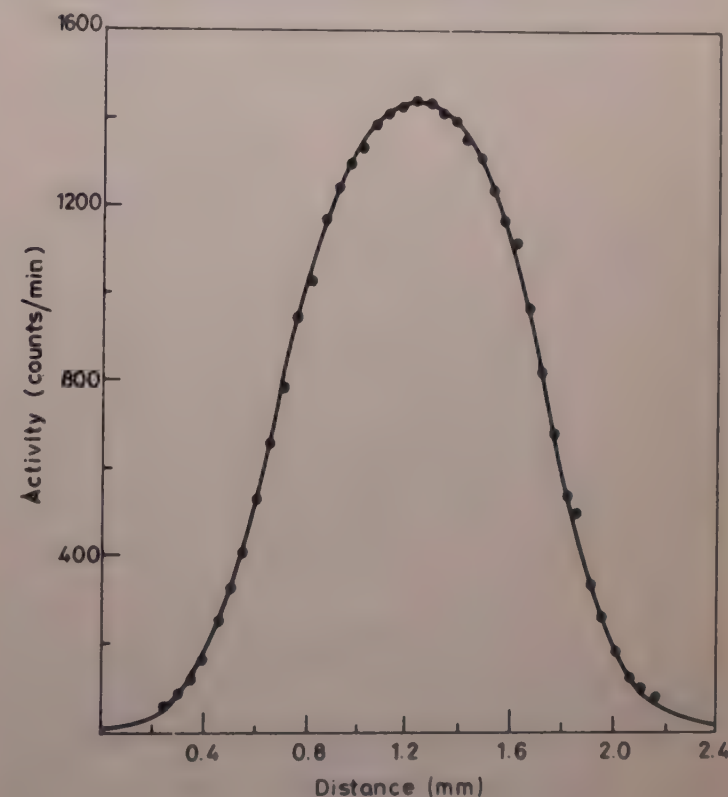


Fig. 4—Radioactive indium concentration profile of a sample annealed at 102°C for 52 hr; continuous line is the fitted curve and circles represent experimental points

Table 1—Experimental Data on Lateral Self-diffusion in Indium Thin Films

Temp. °C	Time of anneal hr	Diffusion coefficient $10^{-9}\text{cm}^2/\text{sec}$
93	74	0.899
102	52	1.45
111	52	3.72
118	50	2.96
126	46	5.07
133	41	7.06
145	55	8.88

radioactive tracer and sectioning techniques and obtained an activation energy of 0.81 eV. This has been correlated to the vacancy diffusion mechanism. Eckert and Drickamer studied self-diffusion in polycrystalline indium. An activation energy of 0.77 eV was given by them for the studies in the temperature range 44-145°C. We have obtained an activation energy of 0.60 eV in the temperature range 93-145°C, which is smaller compared to the data available in bulk. We could not extend the measurements to lower temperatures due to the limitation of the method employed.

Grain boundary diffusion in thin films has been discussed by Gupta *et al.*⁶ and they showed that the ratio of the activation energies for thin films (E_b) and bulk (E_l) is $E_b/E_l = 0.5 \sim 0.7$ for grain boundary diffusion mechanism. The activation energy of 0.60 eV obtained for indium thin films in the present study is in accordance with the above range. Moreover, the value

of the pre-exponential factor obtained by us is also low compared to the bulk values^{11,12} (2.7 cm²/sec for single crystal and 1.02 cm²/sec for polycrystalline indium) which is also an indication of grain boundary diffusion mechanism.

5 Conclusions

We can attribute the activation energy of 0.60 eV obtained for lateral self-diffusion in indium films as due to grain boundary diffusion. This method could be employed wherever it is possible to produce a radioactive isotope of convenient half-life by neutron irradiation. This method can well be employed for lateral self-diffusion as well as inter-diffusion in thin films.

Acknowledgement

The authors wish to express their thanks to Dr Dominic Damien for his help in the computations. They also thank Prof. Y V G S Murti for the useful discussions they had during the course of this work. Their thanks are also due to Dr K V S Rama Rao and his students for providing the thin film coating facilities. They are grateful to Prof. C Ramasastry and Prof. J Sobhanadri for their constant encouragement.

References

- 1 Borders J A, *Thin Solid Films (Switzerland)*, **19** (1973) 359.
- 2 McHugh J A, *Methods of surface analysis* (Elsevier, Amsterdam) 1975, 273.
- 3 Chang C C & Quintana G, *Appl Phys Lett (USA)*, **29** (1976) 453.
- 4 Gupta D, *Phys Rev (USA)*, **7** (1973) 586.
- 5 Gupta D & Asai K W, *Thin Solid Films (Switzerland)*, **22** (1974) 121.
- 6 Gupta D, Campbell D R & Ho P S, *Thin films—Inter-diffusion and reactions* (John Wiley, New York) 1978, 161.
- 7 Beniere F, Reddy K V, Kostopoulos D & Le Traon J Y, *J Appl Phys (USA)*, **49** (1978) 2743.
- 8 Gupta D, *Abstr Bull Metall Soc, AIME (USA)*, **4** (1970) 117.
- 9 Tai K L & Ohring M, *Rev Sci Instrum (USA)*, **45** (1974) 9.
- 10 Tai K L, Sun P H & Ohring M, *Thin Solid Films (Switzerland)*, **25** (1975) 343.
- 11 Dickey J L, *Acta Metall (USA)*, **7** (1959) 350.
- 12 Eckert R E & Drickamer H G, *J Chem Phys (USA)*, **20** (1952) 13.
- 13 Sun P H & Ohring M, *J Appl Phys (USA)*, **47** (1976) 478.

Fig. 5 Arrhenius plot of the diffusion data in indium ($\log D$ versus $1000/T$): present data on thin films are compared with the data available in bulk indium

Behaviour of Large-grain Polycrystalline *n*-InP Grown by SSD Technique

J N ROY, S BASU* & D N BOSE

Semiconductor Division, Materials Science Centre, Indian Institute of Technology, Kharagpur 721 302

and

A J SINGH

Chemistry Division, Bhabha Atomic Research Centre, Trombay, Bombay 400 085

Received 27 July 1982; revised received 13 December 1982

Large-grain (2-3 mm) polycrystalline *n*-InP was prepared by synthesis solute diffusion (SSD) technique. The material thus prepared was fully characterized by X-ray, conductivity and Hall-effect measurements. Room temperature measurements showed carrier concentration $n_e = 3 \times 10^{23}/\text{m}^3$, resistivity $\rho = 3.46 \times 10^{-4}$ ohm-m and Hall mobility $= 6.91 \times 10^{-2} \text{ m}^2/\text{V}\cdot\text{sec}$. The grain-boundary scattering effect was determined taking compensation into account. Using electrochemical technique the band gap was measured as 1.28 eV. These results were compared with the standard sample obtained from Metals Research, U.K. From the temperature variation of carrier concentration and conductivity the activation energies were determined. The conductivity activation energy (E_σ) and the carrier activation energy (E_n) were 9.09×10^{-3} and 1.39×10^{-2} eV respectively. The temperature (T) dependence of mobility (μ) was found to follow the relation $\mu \propto T^{-x}$ with $x = 2.44$. The mobility at 160 K was found to be $0.276 \text{ m}^2/\text{V}\cdot\text{sec}$.

1 Introduction

InP is a useful material for many electronic devices because of its suitable band structure and low surface recombination velocity. For the current optical-fibre communication systems, diode lasers and LEDs based on InP/InGaAsP are considered most suitable as optical light sources. Also high efficiency, stable photo-electrochemical solar cells have recently been prepared¹ using single-crystal InP in which electrons are the minority carriers.

The growth of InP is complicated by the high vapour pressure of phosphorus, 28 atm at 1070°C, the melting point of InP. Low temperature growth of InP was reported by the authors² in which the phosphorus vapour pressure problem and the probable incorporation of impurity from the quartz crucible were minimized. But the quality of the crystal with respect to grain size, mobility, etc. was poor. Gradient freeze³ and synthesis solute diffusion (SSD)⁴ methods have recently been developed in order to grow high quality crystals without employing the expensive high pressure Czochralski liquid encapsulated technique. The SSD technique is fairly simple and can be employed to grow better quality crystal. This technique was first developed by Kaneko *et al.*^{4,5} for the growth of GaP which was subsequently modified for the growth of InP [Ref. 6,7]. Preparation and characterization of large-grain (2-3 mm) polycrystalline *n*-InP by SSD technique is reported in this paper.

2 Experimental Details

In SSD method indium (In) melt was held in a temperature gradient. Phosphorus (P) reacted with In

melt on the surface to form InP which was transported by diffusion to the cooler end and was solidified due to smaller solubility. The experimental set-up is schematically shown in Fig. 1. A quartz crucible (I.D. = 4 mm, O.D. = 6 mm, length = 3.5 cm) containing In (5N) was placed in a larger diameter quartz tube (I.D. = 8 mm, O.D. = 10 mm, length = 17.6 cm) and red phosphorus (5N) was charged at the bottom of this tube. The system was evacuated to 1×10^{-5} Torr and was sealed by fusing. The tube was subsequently put into a two-zone furnace whose temperature profile is shown in Fig. 1(b). The temperature of the phosphorus (T_p) was 450°C, corresponding to its vapour pressure of about 2 atm. The growth rate is dependent on the temperature difference between top of the solution (InP surface), i.e. T_2 and the temperature of the growing interface, i.e. T_1 and is limited by the diffusion process of the solute. The quality of the crystal also depends upon the temperature gradient. Since the diffusion co-

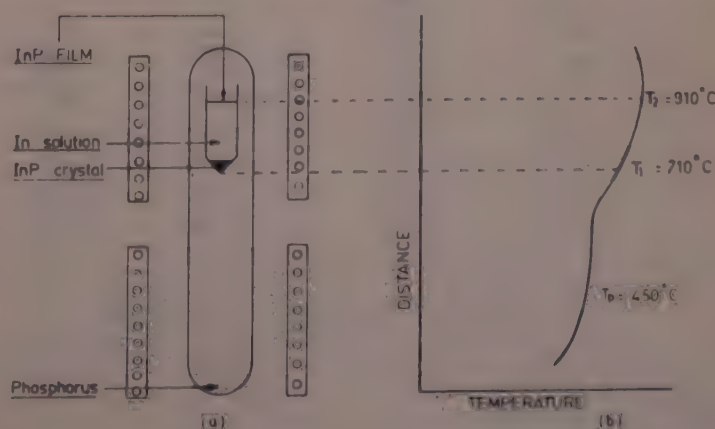


Fig. 1—(a) Experimental set-up for the SSD growth of InP and
(b) the temperature profile of the two-zone furnace

efficiency of P in In is low, a large temperature gradient is normally required to increase the growth rate. On the other hand, large temperature gradient produces poor quality crystals. So optimization is necessary to obtain the best results. In the present study, the following temperatures were used:

$$T_1 = 710^\circ\text{C}, T_2 = 910^\circ\text{C}, T_p = 450^\circ\text{C}$$

and temperature gradient $\approx 20^\circ\text{C}/\text{cm}$.

The above conditions were maintained for 114 hr. After the growth run was completed, the furnace was cooled slowly ($3^\circ\text{C}/\text{hr}$) up to $T_2 = 850^\circ\text{C}$ and $T_1 = 650^\circ\text{C}$. Then the furnace was cooled to room temperature at the rate of nearly $30^\circ\text{C}/\text{hr}$. One end of the outer quartz tube was cut open to remove the crystal.

3 Results and Discussion

The formation of InP was verified by the analysis of the product using X-ray diffraction studies. No other phases were observed within the sensitivity (1%) of the instrument. Table 1 shows the comparison between calculated and standard d values for InP.

The stoichiometry was determined by electron microprobe analysis taking single-crystal InP obtained from Metals Research, U.K. as reference. The results are given in Table 2.

The results show that the stoichiometry is very close to that of the standard sample and there is no phosphorus deficiency in the grown sample since the observed differences are within the limit of the accuracy of the instrument.

Table 1—Comparison between Calculated and Standard d Values for InP

Peak No.	2θ	[Radiation used: Cu-K _α , $\lambda = 1.54 \text{ \AA}$]		hkl
		$d(\text{calculated})$	$d(\text{standard})$	
1	26.3	3.3885	3.39	111
2	30.5	2.9308	2.94	200
3	43.63	2.0745	2.08	220
4	51.63	1.7696	1.771	311
5	54.1	1.6951	1.693	222
6	63.4	1.467	1.467	400
7	69.85	1.3465	1.347	311
8	71.95	1.3123	1.312	420
9	80.1	1.198	1.198	422
10	86.05	1.1298	1.129	511, 333
11	9.6	1.0373	1.038	440

Table 2—Stoichiometry of SSD-grown InP

Standard InP (obtained from Metals Research, U.K.)	In content	P content
SSD-grown InP	78.74	21.26

SSD-grown InP	In content	P content
	77.976	21.477

The grain size was determined optically and was found to be of the order of 2-3 mm. The band gap was measured using an electrochemical technique by Faktor *et al*⁸. The specimen was used as anode and platinum as the cathode in 1M potassium hydroxide solution ($\text{pH} = 11.5$) electrolyte. The anode was illuminated and the wavelength of the incident light was varied between 0.4 and $0.89 \mu\text{m}$ using a Jarrell-Ash monochromator and the resultant photovoltage was measured. A photovoltage versus wavelength plot was obtained (Fig. 2) and from the cut-off wavelength the band gap, as determined using the relation $E_g = 1.24/\lambda$, was found to be 1.28 eV at room temperature.

From the thermoelectric power measurements it was found that the material was *n*-type which was also verified by Hall-effect measurements. Conductivity and Hall mobility were determined from Hall-effect measurements using van der Pauw technique. Ohmic contact was made by evaporating In-Sn alloy and subsequent annealing at 400°C for 1 min in argon atmosphere. The results are summarized in Table 3, which also shows the comparison between prepared and standard InP samples at room temperature. It is evident from Table 3 that there is a good agreement between the properties of the prepared sample and those of the standard sample grown by LEC. The higher mobility of the single crystal is due to the absence of grain-boundary scattering. For the prepared sample, the grain-boundary scattering effects were calculated taking compensation into account as described by Jensen⁹. Table 4 summarizes the results.

From the temperature variation (160-300 K) of conductivity, carrier concentration and mobility, activation energies and temperature dependence of mobility were found out. Temperature (T) dependence of mobility (μ) followed the relation $\mu \propto T^{-x}$ where the value of x was found out from $\log T$ versus $\log \mu$ plot. The results are summarized in Table 5.

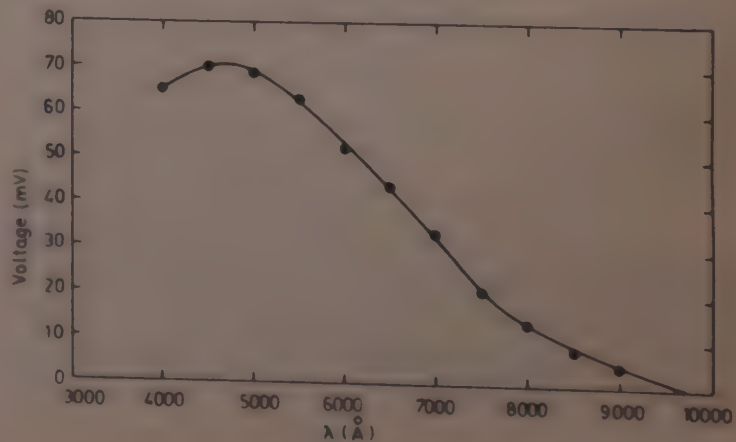


Fig. 2—Variation of photovoltage with wavelength for determination of band gap

Table 3—Comparison between the Properties of Prepared and Standard InP Samples at Room Temperature

	Prepared sample (SSD)	Standard sample (LEC) from Metals Research, UK
X-ray diffraction	<i>d</i> values close to the standard values and no other phases	
Grain size	2-3 mm	Single crystal
Band gap* (eV)	1.28	1.29
Resistivity (ohm-m)	3.46×10^{-4}	2×10^{-4}
Mobility ($\text{m}^2/\text{V}\cdot\text{sec}$)	6.91×10^{-2}	1.3×10^{-1}
Carrier conc. (n_e , m^{-3})	3×10^{23}	2×10^{23}

*Also measured by electrochemical technique.

Table 4—Compensation and Grain Boundary Parameters of SSD-grown InP

Concentration of charged donors, N_d^+ (m^{-3})	3.5×10^{-23}
Concentration of charged acceptors, N_a^- (m^{-3})	0.5×10^{23}
$C = (N_a^- N_d^+)$	0.143
Compensation ratio $r = N_i/n_e$ (where $N_i = N_d^+ + N_a^-$)	1.333
Grain boundary limited mean free path (\AA)	155.5
Single crystal mobility ($\text{m}^2/\text{V}\cdot\text{sec}$)	0.3199
Grain boundary mobility ($\text{m}^2/\text{V}\cdot\text{sec}$)	0.08814

Table 5—Activation Energies and Mobility of SSD-grown InP

Mobility (at 160 K), $\text{m}^2/\text{V}\cdot\text{sec}$	0.276
Activation energy (E_a from $1/T - \ln n$ curve, eV)	1.39×10^{-2}
Activation energy (E_a) from $1/T - \ln \sigma$ curve, eV	9.09×10^{-3}
x (where $\mu \propto T^{-x}$)	2.44

4 Conclusion

The SSD-grown InP reported here is of satisfactory quality compared with standard single crystal from Metals Research, U.K., although grain-boundary scattering is present, as determined experimentally. Temperature variation of mobility ($\mu \propto T^{-x}$) shows $x = 2.44$ which is also comparable to the value of $x = 2.0-2.4$ for pure crystals as reported by Kubato *et al.*⁶. The

comparatively low mobility value ($6.91 \times 10^{-2} \text{ m}^2/\text{V}\cdot\text{sec}$) is mainly due to grain-boundary scattering while the effect of compensation is small ($r = 1.333$).

Acknowledgement

The work was supported by a grant from the Department of Atomic Energy (DAE), Government of India. One of the authors (JNR) also acknowledges the financial support through a Junior Research Fellowship from the DAE.

References

- Heller A, Miller B & Thiel F A, *Appl Phys Lett (USA)*, **38** (1981) 282.
- Roy J N, Basu S & Bose D N, *Solar energy materials* (North-Holland, Amsterdam), **5** (1981) 379.
- Miller S E, *Compound semiconductors* (Reinhold, New York) **1** (1962) 274.
- Kaneko K, Ayabe M, Dosen M *et al*, *Proc IEEE (USA)*, **61** (1973) 884.
- Kaneko K, Ayabe M & Isawa N, *Jpn J Appl Phys (Japan)*, **18** (5) (1979) 861.
- Kubato E & Sugii K, *J Appl Phys (USA)*, **52** (1981) 2983.
- Engh R O, Peterson S R, Thorne J P & Peterson P E, *Appl Phys Lett (USA)*, **38** (1981) 243.
- Faktor M M, Ambridge T, Elliott C R & Regnault J C, *Current topics in materials science*, edited by E Kaldus (North-Holland (Amsterdam), **6** (1981) 1.
- Jensen B, *J Appl Phys (USA)*, **50** (1979) 5800.

Conductivity of Magnesium Valerate Solutions in Binary Liquid Mixtures

S N GOUR & UMESH KUMAR

Department of Physics, D A V College Muzaffarnagar 251 001
and

R P VARMA*

Department of Chemistry, D A V College Muzaffarnagar 251 001

Received 6 November 1981; revised received 8 February 1983

Specific conductivity of magnesium valerate (soap) solutions in binary liquid mixtures has been studied. It is found that the soap aggregates into micelle and the CMC is independent of benzene, chlorobenzene and *p*-xylene concentrations in methanol and the temperature. The conductivity data fit well in the equation: $\log \lambda = A + B \log C$ where *A* and *B* are constants and *C* is the concentration of soap in mol dm^{-3} . Constant *A* increases with increase in temperature and methanol concentration in the mixture but the values of $-B$ are found independent. The soap is a weak electrolyte which dissociates below the CMC. Molecular conductivity at infinite dilution, λ_∞ , dissociation constant (*K*), activation parameters of dissociation, ΔH° , ΔG° and ΔS° have been evaluated and the effect of composition of binary liquid mixtures has been discussed.

1 Introduction

Conductivity measurements are the basis for some of the earliest theoretical developments in the field of micelle formation and structure. Two basic characteristics which distinguish surfactants from ordinary solute are their surface activity and their ability to form micelle by an association-dissociation equilibrium. The relationships between these properties and their uses in greases¹⁻⁴, paints and varnishes⁵, catalytic actions^{6,7}, etc. have been studied extensively.

Magnesium valerate is found to aggregate into micelle in water and the critical micelle concentration (CMC), dissociation constant, *K*, molecular conductivity at infinite dilution, λ_∞ , and heat of dissociation, ΔH° have been evaluated⁸. The conductivity of these soaps in alcohols has been investigated^{9,10} which confirms that CMC is unaffected by change in temperature.

In the present paper, we report the conductivity of magnesium valerate in binary liquid mixtures of methanol with benzene, chlorobenzene and *p*-xylene at different temperatures in order to study its micellar behaviour.

2 Experimental Details

Methanol, benzene, chlorobenzene, *p*-xylene and magnesium carbonate (Merck or B.D.H.) were used. *n*-valeric acid, obtained from Sigma Chem. Co., was purified by distillation under reduced pressure and the purity was confirmed by b.p. measurements.

The calculated amount of magnesium carbonate was weighed and suspended in water. The suspension was heated up to 80°C and the required amount of valeric acid was added in portions under constant stirring. After evolution of carbon dioxide had ceased, the

magnesium valerate was purified by recrystallization from alcohol and then dried in vacuum.

The procedure of conductivity measurement was the same as reported earlier¹¹. Mixtures of known composition were prepared by volume, taking precautions as far as possible to keep the solutions out of contact with the atmosphere. Lower percentages of solvent mixtures were used which allowed the distinct measurement of conductivity of solutions.

3 Results and Discussion

Specific conductivity (*k*) soap solutions increases with increase in concentration of soap. The plots (Fig. 1) of *k* vs *C* indicate that a point is reached at which *k* increases at a slower rate. The concentration at which the inflection occurs, i.e. 0.01 *M*, shows the CMC of soap. This is independent of benzene, chlorobenzene and *p*-xylene concentrations in methanol, temperature and the composition of the mixture. The CMC of magnesium valerate, 0.01 *M* in methanol is also found¹² to be independent of temperature.

Molecular conductivity (λ) obtained from the measured specific conductivity of solutions decreases

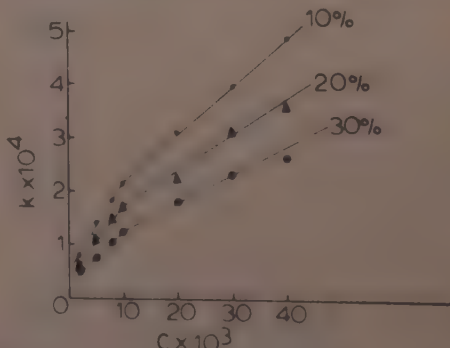


Fig. 1 - Plot of specific conductivity *k* ($\text{ohm}^{-1} \text{cm}^{-1}$) vs concentration *C* (in mol dm^{-3}) of magnesium valerate in methanol (B) in presence of chlorobenzene (A) at 35°C

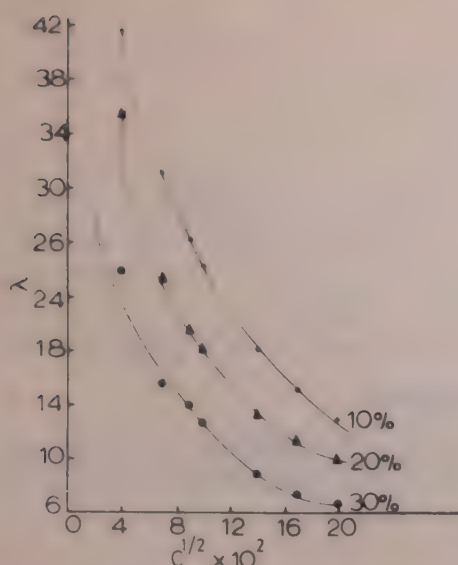


Fig. 2—Plot of λ vs $C^{1/2}$ of magnesium valerate in methanol (B) in presence of benzene (A) at 35°C

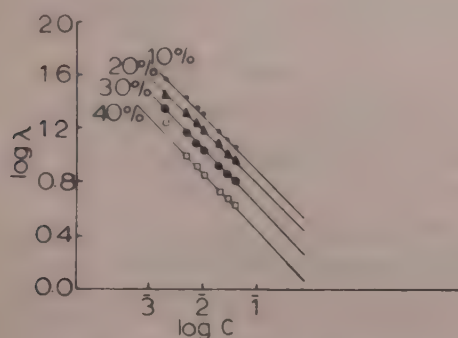


Fig. 3—Plot of $\log \lambda$ vs $\log C$ of magnesium valerate in methanol (B) in presence of *p*-xylene (A) at 35°C

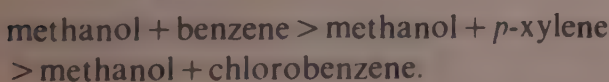
with increase in concentration of soap and composition of the solvent. The plots (Fig. 2) of λ vs $C^{1/2}$ are concave upwards. This is due to the weak electrolyte behaviour of soap.

Conductivity behaviour of soap solutions at different temperatures and compositions of liquid mixtures is represented by

$$\log \lambda = A + B \log C \quad \dots(1)$$

where A and B are constants.

A and B are found from the slopes and intercepts of linear plots (Fig. 3) of $\log \lambda$ vs $\log C$. It is seen that the constant A of soap increases with increase in temperature and concentration of methanol in the mixture and varies in different solvent mixtures in the following order:



Constant B is independent of temperature and composition of mixture. This supports the idea that CMC remains unaffected by the change in these variables.

Magnesium valerate is found to behave as a weak electrolyte in dilute solutions¹³ and therefore the

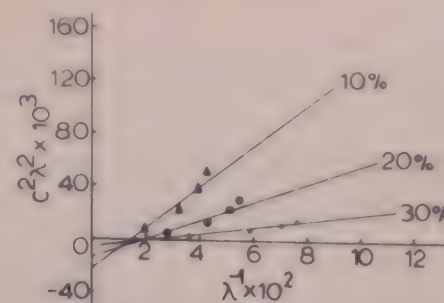
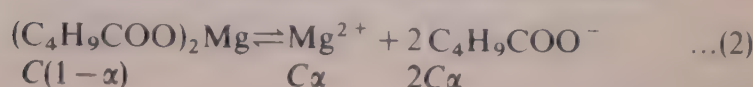


Fig. 4—Plot of $C^2\lambda^2$ vs λ^{-1} of magnesium valerate in methanol (B) in presence of chlorobenzene (A) at 50°C

dissociation of soap can be derived as follows:



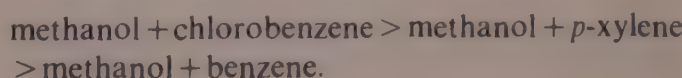
$$K = \frac{C\alpha(2C\alpha)^2}{C(1-\alpha)}; K = \frac{4C^2\alpha^3}{1-\alpha} \quad \dots(3)$$

Since α is very small, ionic concentrations would be low; therefore interionic effects can be neglected. On substituting $\alpha = \lambda/\lambda_\infty$ in Eq.(3) we obtain the expression:

$$C^2\lambda^2 = \frac{K\lambda_\infty^3}{4\lambda} - \frac{K\lambda_\infty^2}{4} \quad \dots(4)$$

The applicability of Eq.(4) has been tested graphically (Fig. 4) by plotting $C^2\lambda^2$ vs λ^{-1} . The plots are linear below CMC and the equation fails above this concentration. The values of λ_∞ and K have been evaluated from the slopes and intercepts of these plots.

Molecular conductivity at infinite dilution increases as the temperature increases in different solvent mixtures and decreases with increase in methanol concentration at different temperatures. A comparison of λ_∞ values of soap in different solvent mixtures of varying compositions shows that they are in the following order:



Methanol molecules are associated because of hydrogen bonding and the order of λ_∞ variations in different solvent mixtures is the same as the order of polarity of solvents. It may be pointed out that chlorobenzene is highly polar than *p*-xylene and benzene.

Dissociation constant (K) of the soap increases with increase in addition of benzene but decreases with increasing concentration of chlorobenzene and *p*-xylene. The electrostatic attractive forces in comparatively less non-polar than benzene liquids, i.e. chlorobenzene and *p*-xylene, are large in a medium of low dielectric constant which give rise to a very diminished dissociation. The value of K also decreases as the temperature increases. The plots of $\log K$ vs T^{-1}

Table 1—Values of ΔH° , ΔG° , ΔS° (at 35°C), $\left(\frac{\partial \Delta G^\circ}{\partial T}\right)$ and $\left(\frac{\partial \Delta S^\circ}{\partial T}\right)$ of Magnesium Valerate in Methanol in Presence of Different Liquids

Vol. % of liquid present	35°C				
	$-\Delta H^\circ$ kJ mol ⁻¹	$-\Delta G^\circ$ kJ mol ⁻¹	$-\Delta S^\circ$ kJ K ⁻¹ mol ⁻¹	$-\left(\frac{\partial \Delta G^\circ}{\partial T}\right)$ kJ K ⁻¹	$-\left(\frac{\partial \Delta S^\circ}{\partial T}\right) \times 10^3$ mol ⁻¹
Benzene					
10	47.86	21.19	0.08	0.18	0.87
20	43.07	20.45	0.07	0.20	0.92
30	38.29	19.35	0.06	0.20	0.96
Chlorobenzene					
10	67.01	24.61	0.13	0.28	1.46
20	76.58	24.69	0.16	0.27	1.56
30	95.72	24.93	0.22	0.35	1.88
p-Xylene					
10	33.50	24.39	0.02	0.17	0.62
20	43.07	24.69	0.05	0.20	0.83
30	57.43	24.83	0.10	0.27	1.25
40	95.72	25.71	0.22	0.35	2.09

are linear, and the heats of dissociation ΔH° calculated from slopes of these plots are given in Table 1. It is observed that the values of $-\Delta H^\circ$ vary similarly with concentrations of additives as that of K .

Free energy ΔG° has been calculated from the relationship:

$$\Delta G = RT \ln K \quad \dots(5)$$

where K is a dissociation constant.

Values of entropy of dissociation (ΔS°) have also been obtained from ΔH° and ΔG° . Both free energy and entropy of dissociation increase with increase in concentration of chlorobenzene and *p*-xylene in the mixture, whereas in benzene it shows the reverse behaviour. The temperature coefficients of free energy and entropy of dissociation have been calculated and are recorded in Table 1.

Acknowledgement

The authors are thankful to the D.A.V. College authorities for providing laboratory facilities.

References

- 1 Adams E W, Brunstrum L C & Flint G W, *US Pat* 2,341,134 (1944).
- 2 Baouman A, *Ind Chim (France)*, **33** (1946) 55.
- 3 Puddington I E, *Inst Spokesman Natl Lubric Grease Inst (USA)*, **9** (1945) 1.
- 4 Butcosk R A, *US Pat* 2,842,493 (1958).
- 5 Minich A & Levinson H, *US Pat* 2,236,296 (1941).
- 6 Bespyatov M P & Polystyanov V I, *Maslo-Zhir Promst (USSR)*, **28** (1962) 14.
- 7 Golendeev V I, Bogareva K G, Bobkova E I & Dobrynina O N, *Maslo-Zhir Promst (USSR)*, **24** (1958) 17.
- 8 Varma R P & Kumar K, *Cellul Chem & Technol (Romania)*, **9** (1975) 23.
- 9 Varma R P & Kumar K, *Colloid & Polym Sci (USA)*, **256** (1978) 266.
- 10 Varma R P, *J Indian Chem Soc*, **LVI** (1979) 842.
- 11 Varma R P, Singh K & Singh H, *Bull Chem Soc Jpn (Japan)*, **51** (1978) 1530.
- 12 Varma R P & Kumar K, *J Indian Chem Soc*, **LIV** (1977) 491.
- 13 Kraus C A & Bray W C, *J Am Chem Soc (USA)*, **35** (1913) 1315.

Excitation of Hydrogen Atom to the $n=2$ State by Helium-Ion Impact

SHYAMAL DATTA, KANIKA ROY† & S C MUKHERJEE*

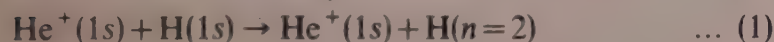
Department of Theoretical Physics, Indian Association for the Cultivation of Science, Jadavpur, Calcutta 700 032

Received 31 May 1982; revised received 5 March 1983

The two-state distortion approximation in the impact parameter formulation is employed to calculate the cross-sections for $\text{He}^+(1s) + \text{H}(1s) \rightarrow \text{He}^+(1s) + \text{H}(n=2)$ collision process for the incident energy ranging from 16 to 2500 keV. The present results are in reasonably good agreement with those of the existing four-state calculation and the experimental findings.

1 Introduction

In a previous investigation¹ we have studied the excitation of the projectile He^+ ions in collision with hydrogen atoms using an approach based on the two-state distortion approximation² in the impact parameter formulation. On comparison with the many-state close-coupling calculation, we have found that the distortion calculation¹ is in reasonably good agreement specially in the intermediate- and high-energy region. The low computing cost and the numerical simplicity makes the distortion calculation highly attractive as compared to the coupled-state calculation for describing collisions of systems having internal structure for both the target and the projectile in the above mentioned energy region. In the present paper, we propose to apply the same method¹ to evaluate the total cross-sections for the process



and compare the calculated results with other existing calculations obtained by using the Born², the two- and four-state eikonal^{2,3}, the first-order Glauber approximation⁴, the symmetrized first-order Glauber approximation⁵, and the Vainshtein-Presnyakov-Sobelman approximation⁶ and also with the recent experimental measurements⁷⁻¹⁰. However, all the computed results²⁻⁶ are found to exhibit varying agreement with the experimental findings in the intermediate-energy region (50-200 keV).

2 Theory

The two-state distortion amplitude for $\text{He}^+ - \text{H}$ collisions can be expressed¹ as

$$A_m^D(\infty) = \exp \left[\frac{i}{v} \int_{-\infty}^{\infty} F_{mm}(s) ds \right] \times \frac{i}{v} \int_{-\infty}^{\infty} A_1 F_{m1} \exp \left[-\frac{i}{v} \int_{-\infty}^s F_{mn} ds' \right] ds \dots (2)$$

with

$$\begin{aligned} F_{mn} &= -\langle \Phi_m | V_i | \Phi_n \rangle = V_{mn} \exp[i\varepsilon_{mn} s/v] \\ \varepsilon_{mn} &= \varepsilon_m - \varepsilon_n \\ S &= vt \\ V_i &= -\frac{2}{r_{A_2}} - \frac{1}{r_{B_1}} + \frac{1}{r_{12}} \end{aligned} \dots (3)$$

$\Phi_n(\mathbf{r}_{A_1}, \mathbf{r}_{B_2}) = \Phi_1^{\text{He}^+}(\mathbf{r}_{A_1}) \Phi_n^H(\mathbf{r}_{B_2})$

the symbols being the same as used in our previous paper¹.

For $2s$ and $2p_{\pm 1}$ state excitations, all the V_{mn} involved are even in s , and on simplification one obtains the distortion probability as

$$P_m^D = [A_m^D(\infty)]^2 \quad \dots (4)$$

where

$$A_m^D(\infty) = \frac{2}{v} \int_0^{\infty} V_{m1} \cos \left[\frac{1}{v} \left\{ \int_0^s (F_{11} - F_{mm}) ds' + \varepsilon_{m1} s \right\} \right] ds \quad \dots (5)$$

For $2p_0$ state excitations, all the V_{mn} involved are odd in s , and the distortion probability reduces to

$$A_m^D(\infty) = \frac{2}{v} \int_0^{\infty} V_{m1} \sin \left[\frac{1}{v} \left\{ \int_0^s (F_{11} - F_{mm}) ds' + \varepsilon_{m1} s \right\} \right] ds \quad \dots (6)$$

The total cross-section for excitation from the ground state to the m th state is given by

$$\sigma_m = 2\pi \int_0^{\infty} P_m^D pdp \quad \dots (7)$$

where p is the impact parameter.

The method for calculating the distortion cross-sections has been described earlier¹ and will not be presented here.

3 Results and Discussion

We present our calculated values for the total cross-sections for the process (1) in Table 1 and compare

* Present address: Department of Physics University of Durham, Durham DH1 3LE (UK)

Table 1—Distortion Approximation Cross-sections, σ_{2s} and σ_{2p} (in units of a_0^2) in the Reaction $\text{He}^+(1s) + \text{H}(1s) \rightarrow \text{He}^+(1s) + \text{H}(n=2)$

Energy of incident He^+ ion (keV)	Present distortion calculation		Full two-state calculation of Flannery		Four-state calculation of Flannery		First Born approximation of Flannery	
	σ_{2s}	σ_{2p}	σ_{2s}	σ_{2p}	σ_{2s}	σ_{2p}	σ_{2s}	σ_{2p}
16	1.04(-2)	3.39(-1)	1.01(-2)	9.20(-2)	1.22(-1)	1.04(-1)	2.31(0)	3.63(0)
25	7.04(-2)	9.16(-1)	5.86(-2)	4.02(-1)	4.30(-1)	3.78(-1)	2.37(0)	5.19(0)
36	1.93(-1)	1.68(0)	1.65(-1)	1.19(0)	1.02(0)	9.03(-1)	2.17(0)	6.12(0)
64	4.28(-1)	3.35(0)	3.90(-1)	3.30(0)	2.08(0)	2.35(0)	1.6(0)	6.67(0)
100	5.16(-1)	4.63(0)	4.86(-1)	4.57(0)	2.12(0)	3.55(0)	1.21(0)	6.33(0)
200	4.51(-1)	4.80(0)	4.42(-1)	4.74(0)	1.35(0)	4.18(0)	7.02(-1)	5.09(0)
400	2.98(-1)	3.67(0)	2.94(-1)	3.65(0)	6.24(-1)	3.46(0)	3.69(-1)	3.60(0)
900	1.55(-1)	2.31(0)	1.54(-1)	2.24(0)	2.38(-1)	2.20(0)	1.70(-1)	2.17(0)
2500	6.03(-2)	1.07(0)	6.03(-2)	1.02(0)	7.32(-2)	1.02(0)	6.25(-2)	1.00(0)

Note: The numbers in the parenthesis denote the powers of ten by which the numbers are to be multiplied.

them with the two-state and the four-state impact parameter calculations of Flannery². It is found from Table 1 that at high energies of the projectile the present calculation for 2p excited state coincides with the first Born, the two-state, and the four-state calculations. On the other hand, the cross-sections for the 2s excited state at high energies obtained by applying the four-state calculations² differ from the first-Born, the two-state, and the present distortion calculations. It may, however, be noted that the two-state calculation of Flannery² does not differ much from the present distortion calculation above 200 keV. Since the present distortion calculation neglects the effect of back coupling, the close agreement between the full two-state and the present calculation indicates that the effect of back coupling is not very much appreciable for the s-state excitations.

In Fig. 1, our results for the excitation of hydrogen atom by He^+ ion impact in the 2s state are compared with the theoretical results² obtained in the first Born, the two-state and the four-state calculations in the impact parameter treatment. The full two-state results of Flannery agree well with the present distortion calculation throughout the energy range of the projectile. The cross-sections calculated by the four-state method² agree reasonably well in shape with the present calculation; however, the magnitude of the four-state calculation is somewhat larger in the intermediate-energy region. With the increase of energy, the cross-sections obtained by the first Born approximation approach closely to the present calculated results. However, the four-state results predict somewhat larger values of cross-sections than the first Born and the present calculation. This overestimation, according to Flannery², is due to the strong 2p-2s dipole coupling which has been incorporated in the four-state calculation.

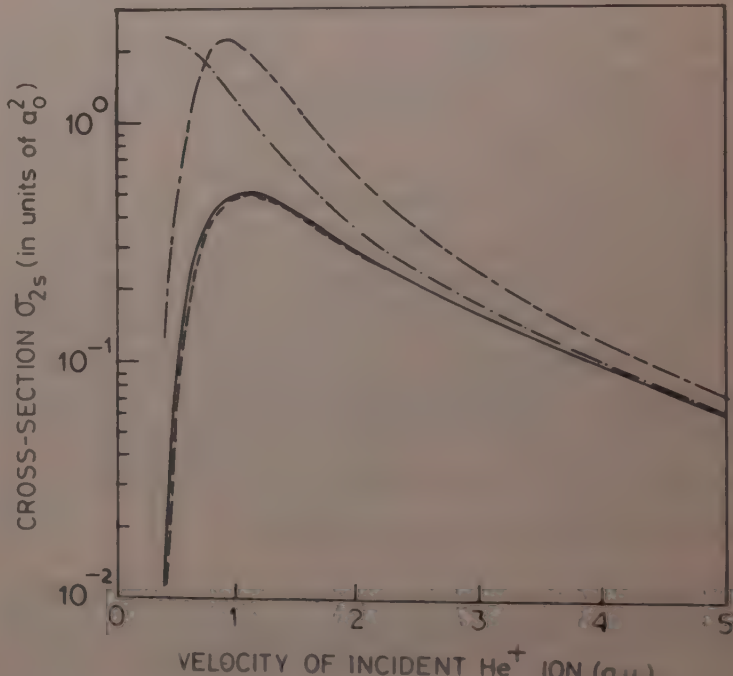


Fig. 1—Cross-sections for $1s \rightarrow 2s$ excitation of hydrogen atom by He^+ ion impact in the reaction $\text{He}^+(1s) + \text{H}(1s) \rightarrow \text{He}^+(1s) + \text{H}(2s)$ [Theory: —, present distortion calculation; - - -, first Born calculation (Flannery²); - - - -, four-state impact parameter calculation (Flannery²); - - . - - . - - ., Four-state impact parameter calculation (Flannery²)]

In Fig. 2, we present our results for the excitation of hydrogen atom in the 2p state by the impact of He^+ ion and compare the results with the first Born, the two-state, and the four-state calculations of Flannery². The two-state results almost coincide with the present distortion results except at very low energy side and this again indicates that the effect of back coupling has negligible effect in the cross-sections. The cross-sections obtained by the present two-state distortion calculation agree well both in shape and magnitude with those from the four-state calculation. At high impact energies of the projectile the cross-sections obtained by using the first Born, the two-state and the

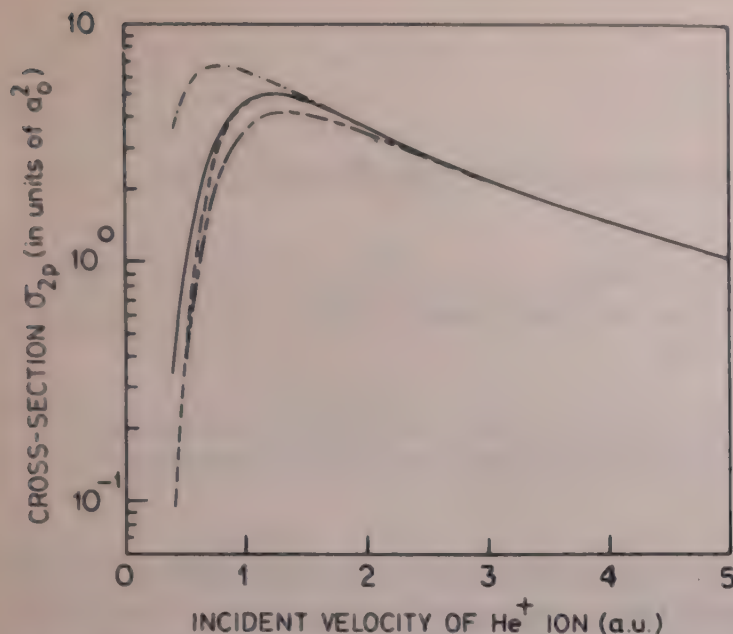


Fig. 2—Same as Fig. 1, but for $1s \rightarrow 2p$ excitation of hydrogen atom by He^+ ion impact in the reaction $\text{He}^+(1s) + \text{H}(1s) \rightarrow \text{He}^+(1s) + \text{H}(2p)$

four-state calculations are identical with those obtained in the present calculation.

In Fig. 3, we compare the total cross-section results for the process (1) with the recent experimental observations of Aldag *et al.*⁸, Young *et al.*⁹, and McKee *et al.*¹⁰, and the available theoretical predictions²⁻⁶. The experimental results of McKee *et al.*¹⁰ for the $2s$ excitation process have been added with the reported cross-section measurement of Young *et al.*⁹ for the excitation of the $2p$ state of hydrogen atom to allow comparison for the process (1) with other total cross-section results. Our present results as well as those of the four-state calculation² agree well with the measurements of Aldag *et al.*⁸ in the energy range 25-50 keV. However, the two-state, the four-state, and the present distortion results underestimate the observed findings below 25 keV and overestimate them above 50 keV. The cross-sections obtained by the first Born approximation are always higher than the existing theoretical and experimental results throughout the energy range considered. The first-order Glauber approximation results⁴ show poor agreement with the observed findings whereas the cross-sections obtained by the use of the symmetrized first-order Glauber

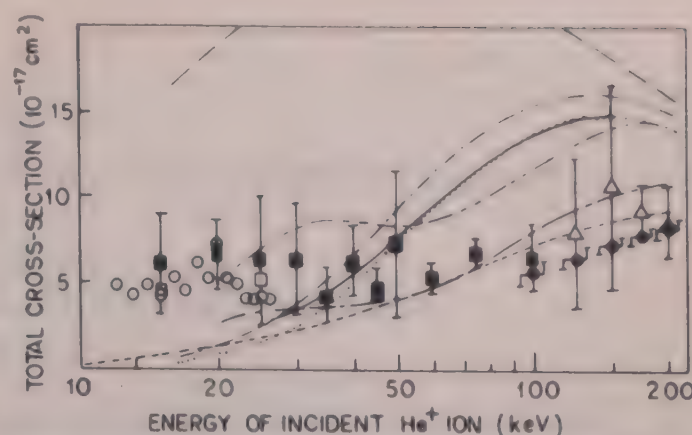


Fig. 3—Total cross-sections for the reaction $\text{He}^+(1s) + \text{H}(1s) \rightarrow \text{He}^+(1s) + \text{H}(n=2)$ [Theory: —, present distortion calculation; - - -, first Born calculation [Flannery²]; ... , full two-state impact parameter calculation (Flannery²); ——, four-state impact parameter calculation (Flannery); - - - - , first-order Glauber calculation (Franco⁴); - - - - - , symmetrized first-order Glauber calculation (Franco⁵); ---, Vainshtein-Presnyakov-Sobelman approximation calculation (Theodosiou⁶). Experiment: ■ and Δ, Aldag *et al.*⁷; ○, McKee *et al.*¹⁰; □, Young *et al.*⁹; ●, Aldag *et al.*⁸]

approximation⁵ are found to be in good agreement with the data in the energy range 25-175 keV. The Vainshtein-Presnyakov-Sobelman results⁶ are also in good agreement with the experimental values over the energy range 50-200 keV. Above 50 keV, all the existing theories predict cross-sections with varying agreement among themselves. The present distortion calculation is, however, in reasonable agreement with the four-state calculation².

References

- Datta S, Roy K & Mukherjee S C, *Phys Rev A (USA)*, **23** (1981) 1775.
- Flannery M R, *J Phys B (GB)*, **2** (1969) 1044.
- Flannery M R & McCann K J, *J Phys B (GB)*, **7** (1974) 1349.
- Franco V, *Phys Rev A (USA)*, **20** (1979) 2297.
- Franco V, *Phys Lett A (Netherlands)*, **42** (1979) 759.
- Theodosiou C E, *Phys Rev A (USA)*, **22** (1980) 2556.
- Aldag J E, Peacher J L, Martin P J, *et al.*, *Phys Rev A (USA)*, **23** (1981) 1062.
- Aldag J E, George J M & Park J T, *Bull Am Phys Soc (USA)*, **21** (1976) 1264.
- Young R A, Stebbings R F & McGowan J W, *Phys Rev (USA)*, **171** (1968) 85.
- McKee J D A, Sheridan J R, Geddes J & Gilbody H B, *J Phys B (GB)*, **10** (1977) 1679.

Nonperturbative Solutions for Screened Coulomb Potentials

A P KAJWADKAR & L K SHARMA*

Department of Applied Physics, Government Engineering College, Jabalpur 482011

Received 24 May 1982

Using nonperturbative solutions, the binding energies for different atoms have been evaluated for screened Coulomb potentials. The variation of the wavefunction with r has also been studied. The results obtained are in excellent agreement with earlier calculations.

1 Introduction

It is well known that there are some processes which although occurring outside the nucleus are dominated by distances which are small on the atomic scale (Compton wavelength distances). In atomic photo-effect, for example, Pratt and Tseng¹ have argued that for a wide range of photon energies, electron Compton-wavelength distances are of primary importance. In such a case, the knowledge of screened wavefunction is desirable for including the effects of screening, at least for small r . Further, internal conversion², threshold pair production³ and single quantum annihilation⁴ phenomena are also characterized by small distances on the atomic scale. The normalization screening theory has recently been applied successfully to explain the anomalously large photo-defect cross-section in molecular hydrogen⁵. There are many atomic and nuclear processes which are characterized by the behaviour of an electron wavefunction at the origin. One such phenomenon is the orbital electron capture because, in this process only the region of overlap between electron and nuclear wavefunction is involved.

The screened Coulomb potential also finds importance in atomic phenomena involving electronic transitions. It has been treated numerically and analytically by various workers using different methods, such as WKBJ method⁶, the quantum defect method⁷ and different types of perturbation methods. Realizing the utility of the screened Coulomb potential, several variational calculations⁸⁻¹² have been done and tables of energy as a function of screening parameters have been compiled. McEnnan *et al.*¹³ used analytic perturbation theory for nonrelativistic case, while Greene and Aldrich¹⁰ applied nonperturbative approach to the problem. Later, Mehta and Patil¹⁴, using approximate and nonperturbative approach, predicted binding energies for different atoms.

When a classical charged two-particle system is influenced by a plasma sea, the Coulomb potential is

replaced by a static screened Coulomb potential, the so called Debye potential¹⁵ to explain the interaction. Ray and Ray¹⁶ obtained s -matrix, discrete energies and wavefunctions for the s -states for exponential cosine screened Coulomb (ECSC) potential in Ecker-Weizel (EW) approximation. Recently, Dutt *et al.*^{17,18} obtained bound s -state energies of an electron in ECSC potential by analytical method using EW approximation. They further proposed an extension of the EW approximation to treat the non-zero angular momentum bound-states of a class of screened Coulomb potentials and obtained the discrete energies for Yukawa potential.

Motivated by the growing importance of the screened Coulomb potential, we have considered in this paper a more general potential of the form

$$V(r) = -\frac{Ze^2}{r(1+\delta_0 r^n)} \quad \dots (1)$$

where δ_0 is a screening parameter.

The energy eigenvalues and the wavefunctions for different values of n for potential (1) have been obtained by an approximate and nonperturbative approach.

On comparing our results with the corresponding experimental values and the results of Mehta and Patil¹⁴, it is found that very good fits for bound state energies are obtained for $n=1$ in potential (1). It is also seen that for this value of n , the bound state energies for lower values of Z have poor agreement with the experimental values but the agreement improves for the medium and higher values of Z . Also the shapes of wavefunctions for $n=1$ tally well with those of McEnnan *et al.*¹³

2 Calculation of Eigenenergies

The radial Schrödinger equation with potential (1) can be written as

$$\left[-\frac{1}{2r^2} \frac{d}{dr} r^2 \frac{d}{dr} - \frac{Z}{r(1+\delta_0 r^n)} + \frac{l(l+1)}{2r^2} \right] R(r) = ER(r) \quad \dots (2)$$

In Eq. (2), we have used atomic units (unit of length $a_0 = \hbar^2/m e^2$ and units of energy $= -me^4/\hbar^2$ and $\delta [= (a_0)^n \delta_0]$ is a dimensionless quantity.

Setting $\psi(r) = rR(r)$, Eq. (2) is transformed to

$$\left[-\frac{1}{2} \frac{d^2}{dr^2} + V_1^{\text{eff}}(r) \right] \psi(r) = E\psi(r) \quad \dots (3)$$

In Eq. (3),

$$V_1^{\text{eff}}(r) = \frac{-Z}{r(1+\delta r^n)} + \frac{l(l+1)}{2r^2} \quad \dots (4)$$

$V_1^{\text{eff}}(r)$ may also be written in the form

$$V_1^{\text{eff}}(r) = \frac{-Z\delta r^{n-1}}{(1+\delta r^n) \ln(1+\delta r^n)} + \frac{\delta^2 l(l+1)r^{2n-2}}{2\ln(1+\delta r^n)[(1+\delta r^n)^{1/2} - (1+\delta r^n)^{-1/2}]} \quad \dots (5)$$

as $V_2^{\text{eff}}(r)$ tends to $V_1^{\text{eff}}(r)$ for $\delta r^n < 1$, i.e.

$(\delta r^n)^2 \ll 1$, and hence it is neglected.

Thus Eq. (3) with the help of Eq. (5) takes the form

$$\left[-\frac{1}{2} \frac{d^2}{dr^2} - \frac{Z\delta r^{n-1}}{(1+\delta r^n) \ln(1+\delta r^n)} + \frac{\delta^2 l(l+1)r^{2n-2}}{2\ln(1+\delta r^n)[(1+\delta r^n)^{1/2} - (1+\delta r^n)^{-1/2}]} \right] \psi(r) = E\psi(r) \quad \dots (6)$$

Further, setting

$$E = -\frac{1}{2}a^2\delta^2 \quad \dots (7)$$

$$\psi(r) = \varphi(r)e^{a\delta r^n}$$

Eq. (6) becomes

$$\begin{aligned} & -\frac{1}{2} \frac{d^2\varphi}{dr^2} + an\delta r^{n-1} \frac{d\varphi}{dr} - \frac{Z\delta\varphi(r)r^{n-1}}{(1+\delta r^n)\ln(1+\delta r^n)} \\ & + \frac{\delta^2 l(l+1)\varphi(r)r^{2n-2}}{2\ln(1+\delta r^n)[(1+\delta r^n)^{1/2} - (1+\delta r^n)^{-1/2}]} \\ & - \frac{n^2 a^2 \delta^2}{2} r^{2n-1} \varphi(r) + \frac{n}{2}(n-1)a\delta r^{n-2} \varphi(r) = E\varphi(r) \quad \dots (8) \end{aligned}$$

Now a change of variable $y = \ln(1+\delta r^n)$ along with approximations

$$\varphi'(r) = n\delta e^{-y} \left(\frac{y}{\delta} \right)^{\frac{n-1}{n}} \varphi'(y)$$

and

$$\begin{aligned} \varphi''(r) &= \left[n\delta \left(\frac{y}{\delta} \right)^{\frac{n-1}{n}} \right]^2 \frac{e^{-y}}{ny} (1-y) \\ &\times [ny\varphi''(y) + (n-1-ny)\varphi'(y)] \end{aligned}$$

for $n = 1, l = 0$ (for s-states) transforms Eq. (8) to

$$y(1-y)\varphi''(y) - y(1+2a)\varphi'(y) + y^2\varphi'(y) + \frac{2Z}{\delta}\varphi(y) = 0 \quad \dots (9)$$

In Eq. (9) terms involving δ^2 (for the region $\delta^2 \ll 1$) have been neglected. Further to observe the usefulness of the results with $n \neq 1$ in potential (1) we restrict the study for those processes which are determined in the region $r \simeq 1$. Hence one gets the following for $n = 2$ from Eq. (8)

$$\begin{aligned} & y(1-y)\varphi''(y) - y(3-2y)\varphi'(y) \\ & + \frac{1}{2}\varphi'(y) - 2ay\varphi'(y) + \frac{Z}{2\delta}\varphi(y) \\ & - \frac{a}{2}(1+y+y^2)\varphi(y) = 0 \end{aligned} \quad \dots (10)$$

and the following for $n = -1$

$$\begin{aligned} & y(1-y)\varphi''(y) + y^2\varphi'(y) - y(3+2a)\varphi'(y) \\ & + 2\varphi'(y) + \left(\frac{2Z}{\delta} - 2a \right) \varphi(y) \\ & - 2ay(1+y)\varphi(y) = 0 \end{aligned} \quad \dots (11)$$

2.1 Solutions for the Case, $n = 1$

Assuming $\varphi(y)$ to be of the form

$$\varphi(y) = \sum_{i=0}^{\infty} C_i y^{i+\sigma} \quad \dots (12)$$

and substituting it in Eq. (9), one finds on equating coefficients of like powers of y that $\sigma = 1$ for s-states and the C_i 's satisfying the following recursion relation

$$C_{i+1} = \frac{[(i+1)(i+2a+1) - 2Z/\delta]C_i}{(i+1)(i+2)} \quad \dots (13)$$

If the series (13) is to terminate after a certain finite number of terms (i.e. $C_{M+1} = 0$), then

$$(M+1)(M+2a_M+1) - 2Z/\delta = 0 \quad \dots (14)$$

This expression is identical with the similar expression obtained by Greene and Aldrich¹⁰ for $Z = 1$. Eq. (14) determines the quantity a_M and hence the energy. The wavefunction $\psi_{Ml}(r)$ may now be written as

$$\psi_{Ml}(r) = e^{-a_M \mu r} \sum_{M=0}^M C_M [\ln(1+\mu r)]^{M+\sigma} \quad \dots (15)$$

where δ is replaced by a variational parameter μ as trial function. Thus

$$\psi_{Ml}(r) = k\mu r e^{-a_M \mu r}$$

The condition of normalization finally yields $k^2 = 4a_M^2 \delta$ where μ has been set such that

$$\mu + \delta/a_M = 0$$

Now the expression¹⁰

$$E = \int_0^\infty \psi_{Ml}(r) \left[-\frac{1}{2} \frac{d^2}{dr^2} - \frac{Z}{r(1+\delta r)} + \frac{l(l+1)}{2r^2} \right] \psi_{Ml}(r) dr \quad \dots (16)$$

yields the following for the binding energy

$$E = - \left[\frac{Z\delta}{2} - \frac{\delta^2}{4} \right] \quad \dots (17)$$

2.2 Solutions for the Case, $n=2$

Again for $n=2$ in potential (1), C_i 's satisfy the relation

$$C_{i+1} = \frac{[i(i+2a+1/2) - (Z/2\delta) + (a/2)]2C_i}{i(2i+1)} \quad \dots (18)$$

with $\sigma=0$.

This yields for s-states and for

$$M=0, a_0 = Z/\delta$$

and

$$M=1, \text{ for } a_1 = \left(\frac{Z}{5\delta} - \frac{3}{5} \right) \quad \dots (19)$$

2.3 Solutions for the Case, $n=-1$

Similarly for s-states and for $n=-1$ and $\sigma=0$, the recursion relation is

$$C_{i+1} = \frac{[i(i+2a+2) - 2(Z/\delta) + 2a]C_i}{(i+1)(i+2)} \quad \dots (20)$$

Eq. (20) yields

$$a_0 = Z/\delta$$

and

$$a_1 = \left(\frac{Z}{2\delta} - \frac{3}{4} \right) \quad \dots (21)$$

The above values of a_M finally give the following expression for the wavefunctions

$$\psi_{Mi}(r) = e^{-a_M \delta r^n} \sum_{M=0}^{\infty} C_M [\ln(1 + \delta r^n)]^{M+\sigma} \quad \dots (22)$$

The wavefunctions given by (22) are approximate and their resemblance with exact wavefunctions depends on the extent to which $V_2^{\text{eff}}(r)$ approximates $V_1^{\text{eff}}(r)$.

3 Results and Conclusion

The binding energy values (in keV) obtained from Eq. (17) for $n=1$ for different atoms with Z ranging between 34 and 84, and the values of the screening parameters chosen and the corresponding experimental values are given in Table 1.

It can be seen from Table 1 that the agreement in calculated and observed values is poor for lower values of Z but it improves for higher values of Z .

In Table 2 the binding energy values calculated for $n=-1$ are given. They show a reasonably good agreement with the energy values obtained by Iyer¹⁹.

It may also be mentioned that the screened Coulomb potential (1) changes to a form considered by Mehta *et al.*¹⁴ for $n=-1$. The energy values obtained in this work are comparable with those obtained by them.

It may be noted that the method of investigation used in this paper involves minimum number of parameters and is quite straightforward when compared to the methods used by other workers⁹⁻¹¹. The potential considered by us has a general form and the comparison of shapes obtained for the wavefunction $\psi_{Mi}(r)$ for $n=1$ (Figs 1 and 2) reveals that within the interior of the atom, i.e. $\delta r < 1$, shapes of all the screened Coulomb potentials are similar and are Coulombic in nature. This enhances the chances of possible use of the wavefunctions $\psi_{Mi}(r)$ as the trial wavefunctions. Further, there is a shift of maxima for $n=2$ towards origin for the increasing values of Z . For the same n , the magnitude of the wavefunction falls off rapidly with increase in r for higher values of Z (Fig. 3). Finally we conclude with the remark that fairly

Table 1—Bound State Energies E (in keV) with $n=1$ as a Function of Z and δ

Z	δ	E	Present study with $n=1$ in potential (1)	Experimental (Ref. 14)
34	0.09	-1.52	-1.27	
39	0.095	-1.84	-1.70	
44	0.100	-2.19	-2.21	
49	0.120	-2.93	-2.79	
54	0.130	-3.50	-3.46	
59	0.135	-4.12	-3.98	
64	0.16	-5.11	-5.02	
69	0.18	-6.20	-5.94	
74	0.20	-7.39	-6.95	
84	0.22	-9.22	-9.31	

Table 2—Bound State Energies E (in keV) with $n=-1$ as a Function of Z and δ

Z	δ	E	Present study for $n=-1$ in potential (1)	By dispersion relation (Ref. 14)	By perturbative approach (Ref. 19)
34	0.09	-1.52	-1.30	-1.36	
39	0.095	-1.84	-1.74	-1.55	
44	0.100	-2.19	-2.25	-2.12	
49	0.120	-2.92	-2.82	-2.80	
54	0.130	-3.49	-3.45	-3.53	
59	0.135	-4.11	-4.15	-4.44	
64	0.160	-5.10	-4.92	-5.22	
69	0.180	-5.81	-5.76		
74	0.200	-7.37	-6.66		
84	0.220	-9.20	-8.66		

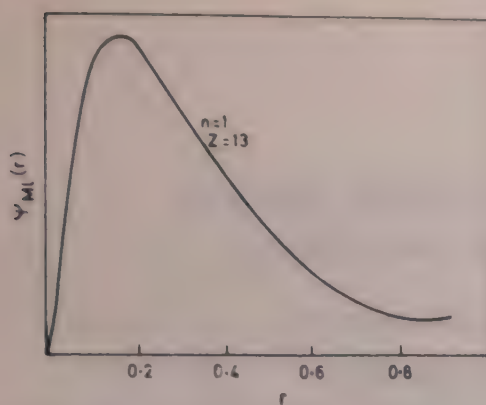


Fig. 1—Unnormalized radial function $\psi_{Ml}(r)$ for 1s state of aluminium ($Z = 13$) for $n = 1$ (Distances are in electron Compton wavelengths.)

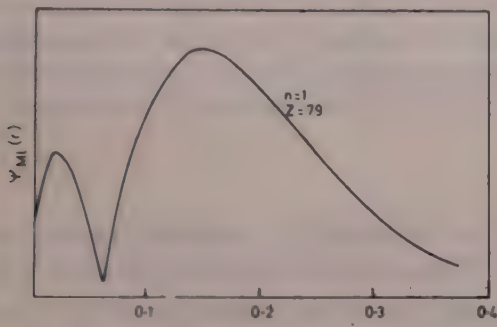


Fig. 2—Unnormalized radial function $\psi_{Ml}(r)$ for 2s state of gold ($Z = 79$) for $n = 1$ (Distances are in electron Compton wavelengths)

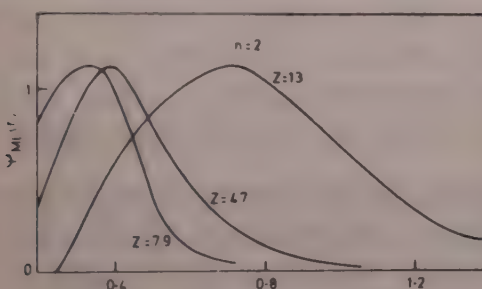


Fig. 3—Unnormalized radial function $\psi_{Ml}(r)$ for 2s state of aluminium, silver and gold for $n = 2$ (Distances are in electron Compton wavelengths.)

satisfactory results of binding energies for potential (1) are obtained only for $n = 1$ and that the utility of results for the cases with $n \neq 1$ is restricted for the processes determined in the region $r \approx 1$. However, such a restriction does not exist for the case $n = 1$.

References

- 1 Pratt R H & Tseng H K, *Phys Rev A (USA)*, **5** (1972) 1063.
- 2 Band I M & Sliv L A & Trzhaskovskaya M B, Institute of Technical Physics, USA Report No. 262 (1970); unpublished order No 1314, 21/IV.
- 3 Tseng H K & Pratt R H, *Phys Rev A (USA)*, **4** (1971) 1835, **6** (1973) 2049.
- 4 Tseng H K & Pratt R H, *Phys Rev A (USA)*, **7** (1973) 1423.
- 5 Cooper J W, *Phys Rev A (USA)*, **9** (1974), 2236.
- 6 Schiff L I, *Quantum mechanics* (McGraw Hill, New York), 1968.
- 7 Seaton M J, *Mon Not R Astron Soc (GB)*, **11** (1958) 8504.
- 8 Lam C S & Varshni Y P, *Phys Rev A (USA)*, **4** (1971) 1875.
- 9 Roussel K M & O'connel R F, *Phys Rev A (USA)*, **9** (1974) 552.
- 10 Greene R L & Aldrich C, *Phys Rev A (USA)*, **14** (1976) 2363.
- 11 Rogers F J, Grabske H C & Harwood D J, *Phys Rev A (USA)*, **1** (1970) 1557.
- 12 Harris G M, *Phys Rev (USA)*, **125** (1962) 1131.
- 13 McEnnan J, Kissel L & Pratt R H, *Phys Rev A (USA)*, **13** (1976) 532.
- 14 Mehta C H & Patil S H, *Phys Rev A (USA)*, **17** (1978) 43.
- 15 Lam C S & Varshni Y P, *Phys Lett A (Netherlands)*, **55** (1976) 363.
- 16 Ray P P & Ray A, *Phys Lett A (Netherlands)*, **78** (1980) 443.
- 17 Dutt R, *Phys Lett A (Netherlands)*, **73** (1979) 310.
- 18 Dutt R, Ray A & Ray P P, *Phys Lett A (Netherlands)*, **83** (1981) 65.
- 19 Iyer R C, *Potential and scattering problems in quantum mechanics*, PhD thesis, University of Jabalpur, Jabalpur, 1980, Chap 4.

Random Electrodynamics of Nonlinear System: Part I—Quartic Anharmonic Oscillator

S SACHIDANANDAM[‡] & I V V RAGHAVACHARYULU[†]

Bhabha Atomic Research Centre, Trombay, Bombay 400 085

Received 26 April 1982; accepted 19 April 1983

A successful extension of the classical techniques of Random Electrodynamics to nonlinear microsystems is still not obtained in the literature. A beginning is made in this direction in this paper. We study the quartic anharmonic oscillator as an illustrative example. By extending one of the approximation methods employed in the study of deterministic nonlinear systems to stochastic nonlinear systems, properties quite close to those given by the quantum mechanical description are obtained. The results partly dispel the doubts raised by Claverie and others in the validity of Random Electrodynamics in the description of nonlinear microsystems.

1 Introduction

Interest in Random Electrodynamics (RED) stems from the possibility that it may emerge as a classical covering theory for quantum mechanics. It postulates the existence of a force due to radiation damping accounting for the radiation losses and a fluctuating zero-point electromagnetic field. Incorporating these two forces in the equations of motion of any classical electrodynamical system, a Langevin type of equation of motion¹ of the system in RED is first obtained. One can then study the solutions of these equations directly or develop a Fokker-Planck type of equation for the distribution function as the problem is stochastic in nature. These two approaches produce equivalent results for simple linear systems, essentially in agreement with those obtained on the basis of quantum theory. As regards the linear oscillator, the quantum results are not qualitatively different from the classical ones: The resonance frequency is independent of the driving fields and remains the same as the classical characteristic frequency; only the mean square displacements and velocities get quantized. The quantum oscillator is thus a classical oscillator on which the radiation forces of damping, and the zero-point fields act independently. However, the Fokker-Planck approach when applied to nonlinear systems has yielded results which are in disagreement with the results obtained when the system is treated quantum mechanically. The disagreements range from a sign difference in the second order correction to the energy of a slightly anharmonic oscillator to the catastrophic self-ionizing solution of the hydrogen atom which is, on the basis of quantum mechanics, obviously unphysical². Unlike in the case of linear systems, the

situation is drastically different with nonlinear oscillators. The greater the deviation of the system from linearity, the more profound is the effect of the driving fields on the system dynamics, necessitating in principle, a nonperturbative approach. It is quite well known that such methods are not available in mathematical literature. But if RED is to be the cover theory for quantum mechanics, then obviously it should yield essentially the quantum results.

We hold that the discrepancy in the results is due to an inadequate treatment of Nonlinear Random Electrodynamical System from the point of view of mathematics rather than lack of soundness in the basic physics itself.

In view of the nonavailability of exact treatments in the literature, the purpose of this note is to develop, at least in the perturbative framework, suitable mathematical techniques that enable us to study nonlinear RED systems using the Langevin type of equations and illustrate the method as applied to a quartic anharmonic oscillator. The other much more physical problems like that of the hydrogen atom will be considered separately.

2 Preliminaries of Random Electrodynamics

The physical idea in RED is as follows:

An electromagnetic system, subject to the additional forces of RED, evolves from an arbitrary initial state, to an equilibrium state in which the electromagnetic energy radiated away by the system is balanced on an average by the energy picked up from the reservoir of random fields. That is, under equilibrium, the radiation reaction force and the zero-point fields produce a stationary value for the mean energy of the system. We now proceed to consider the conceptual basis of these forces.

[†]Division of Radiological Protection.

[‡]Nuclear Physics Division.

2.1 Radiation reaction force

The damping force due to radiation reaction can be considered in a variety of ways: (1) in terms of self-action³; (2) through the canonical formalism in classical mechanics with the inclusion of interaction with radiation; (3) via the nonrelativistic quantum electrodynamics in the Heisenberg picture⁴; and (4) by considerations of the energy loss through radiation⁵. However, the energy loss argument is the most suitable one for our present purpose, since it throws light on the limitations of the resulting form of the force and avoids the idea of self-action, by leaving the source of the reaction force unspecified.

Now consider a point charge in accelerated motion. The non-relativistic Larmor formula for the rate of energy loss by the accelerated charge is given by:

$$-\frac{dE}{dt} = \frac{2e^2}{3c^3} \mathbf{r}^2 \quad \dots (1)$$

We can picture the above loss as arising due to an equivalent radiation reaction force \mathbf{F}_R . This force is to take energy from the particle at the same rate as given by Eq.(1) on an average, when we set

$$\begin{aligned} -\int_0^T \mathbf{F}_R \cdot \mathbf{r} dt &= \frac{2e^2}{3c^3} \int_0^T \mathbf{r} \cdot \mathbf{r} dt \\ &= \frac{2e^2}{3c^3} \left\{ \left[\mathbf{r} \cdot \mathbf{r} \right]_0^T - \int_0^T \mathbf{r} \cdot \mathbf{r} dt \right\} \end{aligned} \quad \dots (2)$$

We note that if the motion is periodic or nearly so, the first term on the right can be neglected, and we get

$$\mathbf{F}_R = \frac{2e^2}{3c^3} \mathbf{r} \quad \dots (3)$$

In view of the neglect of the first term, it would not be correct to use this formula in situations involving arbitrary aperiodic motions of the particle. Moreover, even in periodic motions, the term containing \mathbf{r} should be negligible compared to the other force terms so that the term with the third order derivative can be reduced to a lower order one using suitable proportionality 'constants'. By this procedure we suppress the unphysical runaway and preacceleration solutions. It should be emphasized that one must always bear the above limitations⁶ of the Lorentz damping force in mind. Otherwise one would get the type of counter-intuitive solutions discussed in detail by Jayaratnan⁷.

2.2 Zero-point Electromagnetic Fields (ZPF)

As is well known, quantum electrodynamics (QED) leads to the concept of a vacuum state in which each of the modes (\mathbf{k}, λ) of the free electromagnetic field has a zero-point energy value $1/2\hbar\omega_{k\lambda}$. By virtue of the resulting divergent energy density, the zero-point energy is eliminated in the 'first' renormalization. However, it has been found useful, in certain contexts,

to visualize an equivalent real classical fluctuating electromagnetic radiation, satisfying the homogeneous Maxwell equations. For example, the spontaneous emission by an excited atom is physically pictured as emission stimulated by the ZPF. In the calculation of radiative corrections such as Weisskopf's⁸ on the self-mass of electron and Welton's⁹ on the Lamb shift, the ZPF can be assumed to induce a jiggling and a translational Brownian kind of motion respectively, on the electron. Since the heuristic calculation of Welton, various arguments have been advanced for taking the ZPF as real. One should of course always keep in view the limitations when using these fields, the most important one being the imposition of a suitable upper cutoff to eliminate the divergences.

A simple model for these fields with their infinite number of degrees of freedom is that of a Gaussian random process with the spectral density

$$S(W) = \frac{2\hbar}{3c^3} |\omega|^3 \quad \dots (4)$$

A convenient representation, for ease of application in the Langevin type of differential equations, is, in terms of random phases, as follows:

$$\begin{aligned} \mathbf{E}(\mathbf{r}, t) &= 1/2 \int d^3k \sum_{\lambda=1}^2 \mathbf{e}(\mathbf{k}, \lambda) \sqrt{\frac{\hbar\omega}{2\pi^2}} |a_{k\lambda}| \\ &\quad \exp[-i(\omega t - \mathbf{k} \cdot \mathbf{r})] + c.c \end{aligned} \quad \dots (5)$$

where $a_{k\lambda} = \exp(i\theta_{k\lambda})$ with $\theta_{k\lambda}$ being a random variable uniformly distributed in the interval 0 to 2π , independently for each wavevector \mathbf{k} , and polarization index λ . The usual orthogonality and closure properties hold good for the polarization vectors $\mathbf{e}(\mathbf{k}, \lambda)$. They are:

$$\mathbf{e}(\mathbf{k}, \lambda) \cdot \mathbf{e}(\mathbf{k}, \lambda') = \delta_{\lambda\lambda'}$$

$$\mathbf{e}(\mathbf{k}, \lambda) \cdot \mathbf{k} = 0$$

and

$$\sum_i e_i(\mathbf{k}, \lambda) e_j(\mathbf{k}, \lambda) = \delta_{ij} - k_i k_j / k^2 \quad \dots (6)$$

Further, in view of the independence of the phases for each mode (\mathbf{k}, λ) , we have the following ensemble average $\langle \rangle$ over phases:

$$\langle a_{k\lambda} a_{k'\lambda'}^\dagger \rangle = 0 = \langle a_{k\lambda}^\dagger a_{k'\lambda'} \rangle,$$

and

$$\langle a_{k\lambda} a_{k'\lambda'}^\dagger \rangle = \delta(\mathbf{k} - \mathbf{k}') \delta_{\lambda\lambda'} \quad \dots (7)$$

2.3 Langevin Type of Equations in RED

Consider an electromagnetic system which is subjected to the two forces of damping and radiation fluctuation fields besides any other usual deterministic fields that are already acting on it. Then we obtain a generalized equation in RED of the given system. The

equations so obtained are very similar to the Langevin equations.

In the original Langevin approach to Brownian motion, the damping force arises as the systematic part of the fluctuating influence of the reservoir on the Brownian particle. On the other hand, in the quantum mechanical derivation of the fluctuation-dissipation theorem by Callen and Welton¹⁰, a system losing energy by dissipation, becomes subject to a fluctuating force; in particular, a charged harmonic oscillator with a radiation damping term given by Eq.(3), is acted on by a fluctuating electromagnetic field precisely with the spectrum of the zero-point field plus that given by the Planck formula for blackbody radiation.

In RED, we assume classical dynamics, deduce the damping terms from considerations like those of Section 2.1 and assume the existence of the zero-point fields independently. The resulting Langevin type of equation has several complexities not present in the original Langevin equation, not the least of which is the nonwhite nature of the spectrum defined in Eq.(4) of the fluctuating forces.

3 The Quartic Anharmonic Oscillator in RED

Though a general basis can be developed in treating stochastic nonlinear systems making use of the Langevin type of differential equation within the framework of perturbative mathematical theory, we illustrate the general principle by making use of the quartic anharmonic oscillator as an example.

3.1 Equation of motion

A particle moving in one dimension in a potential given by

$$V(x) = m(\omega_0^2 x^2/2 + \beta x^4/4) \quad \dots (8)$$

satisfies the familiar equation

$$\ddot{x} + \omega_0^2 x + \beta x^3 = 0 \quad \dots (9)$$

Further, we assume that the particle has a charge e which couples it to the radiation reaction and the zero-point fields. Hence, incorporating the two independently acting fields also in the equation of motion defined by Eq.(9), we obtain the stochastic differential equation of the charged particle given by

$$\ddot{x} + \omega_0^2 x + \beta x^3 - \tau \ddot{x} = e/m E_x^0 \quad \dots (10)$$

where $\tau = 2/3 e^2/mc^3$, and E_x^0 is as given by Eq.(5).

The Eq. (10) cannot be solved exactly. However, in having recourse to approximation methods, one should keep in view the peculiar effects of non-linearity. The equation is very similar to that of the Duffing oscillator¹¹ except that the harmonic driving forces in the latter are replaced by radiation fields having the spectrum defined by Eq. (4).

From the literature on the Duffing oscillator, we know that in an iterative or perturbative calculation,

the 'natural' frequency of the oscillation has to be renormalized at every order of the calculation. The reason for this is that the frequency becomes a function of the amplitude and the force term. A simple way to take the major part of this feature non-perturbatively into account is through an optimal linearizational! In this method, the original equation is replaced by a linear equation with the frequency as a parameter. The resulting solution is used to evaluate the time average of the square of the difference between the two equations. The parameter is then fixed by requiring this quantity to be a minimum. We extend the optimal method to the Langevin type of equations by replacing the averages over time by those over the ensembles of random fields in the steady state.

3.2 Solution of the Linear Equation Motion

In view of the foregoing, we first solve, instead of the Eq.(10), the linear equation:

$$\ddot{x} - \tau \ddot{x} + \Omega^2 x = e/m E_x^0 \quad \dots (11)$$

where Ω is to be chosen to minimize the mean square difference between Eq.(10) and Eq.(11). With E_x^0 as given by Eq.(5), the steady state solution of Eq.(11) will be

$$x = \frac{1}{2m} e^2 \sum_{\lambda=1}^2 \int d^3 k \left(\frac{\hbar \omega}{2\pi^2} \right)^{1/2} e_x(\mathbf{k}, \lambda) \times \left[\frac{a \exp(-i\omega t)}{\Omega^2 - \omega^2 - i\tau\omega^3} + c.c. \right] \quad \dots (12)$$

where we have used the dipole approximation in using the fields evaluated at $x=0$. Making use of the expectation values in Eq.(7) for averages over phases, we readily find that

$$\langle x^2 \rangle = \frac{1}{4} \frac{e^2}{m^2} \sum_{\lambda=1}^2 \int d^3 k e_x^2(\mathbf{k}, \lambda) \frac{\hbar \omega}{2\pi^2} \times \frac{2}{(\Omega^2 - \omega^2)^2 + \tau^2 \omega^6} \quad \dots (13)$$

Using Eq. (6) for the summation over the polarization index $e(\mathbf{k}, \lambda)$, performing the angular integration, and using $\omega^2 = c^2 k^2$, we get

$$\langle x^2 \rangle = (\hbar/m\pi)(2/3)(e^2/mc^3) \int_0^\infty \frac{\omega^3 d\omega}{(\Omega^2 - \omega^2)^2 + \tau^2 \omega^6} \quad \dots (14)$$

The integral is evaluated by making use of the fact that the integrand is sharply peaked at $\omega = \Omega$ and replacing all ω 's [except in terms involving $(\Omega - \omega)$] by Ω to yield

$$\langle x^2 \rangle = \hbar/(2m\Omega) \quad \dots (15)$$

Similarly, we get

$$\langle \dot{x} \rangle^2 = (\hbar/2m)\Omega \quad \dots (16)$$

provided we eliminate the logarithmic divergence by assuming a suitable cutoff limit which incidentally provides a radiative correction to the right hand side of Eq. (16).

The n th moment of x^2 can be similarly evaluated by contracting the $a^+(\mathbf{k}, \lambda)$, $a(\mathbf{k}', \lambda')$ factors into all possible pairs so that the $2n$ -fold integration in the \mathbf{k} -space becomes a product of n simple integrations. Since there are $(2n)!/(n!2^n)$ such pairs, we have

$$\langle x^{2n} \rangle = \{(2n)!/n!2^n\} \langle x^2 \rangle^n \quad \dots (17)$$

This completes the analysis of the harmonic oscillations of a charged particle in RED, at zero temperature. And the analysis can be extended to higher temperatures by modifying the spectral density given in Eq. (4) by multiplying it by $\coth(\hbar\omega/2kT)$ so that for example $\langle x^2 \rangle$ becomes

$$\langle x^2 \rangle_T = \langle x^2 \rangle_0 \coth(\hbar\Omega/2kT) \quad \dots (18)$$

The above analysis of the linear oscillator in RED was first obtained by Marshall¹ and most of the subsequent papers and review articles¹²⁻¹⁴ in the field of RED have revolved around it without any essential advance in the understanding of the scope of RED with respect to realistic microsystems.

3.3 Parameter Choice (Optimal) and Evaluation of Ground State Energy of Oscillator

In order to obtain the ground state solution of the linear system dealt within the previous section maximally close to the true solution of the quartic anharmonic oscillator, we shall choose Ω to minimize the quantity

$$\begin{aligned} \epsilon^2 &= \langle (\omega_0^2 x + \beta x^3 - \Omega^2 x)^2 \rangle \\ &= \omega_0^2 - \Omega^2)^2 \langle x^2 \rangle + 2\beta(\omega_0^2 - \Omega^2) \langle x^4 \rangle \\ &\quad + \beta^2 \langle x^6 \rangle \end{aligned} \quad \dots (19)$$

On making use of Eq. (17), this becomes

$$\begin{aligned} \epsilon^2 &= \omega_0^2 - \Omega^2)^2 \frac{\hbar}{2m\Omega} + 6(\omega_0^2 - \Omega^2)\beta \left(\frac{\hbar}{2m\Omega} \right)^2 \\ &\quad + 15\beta^2 \left(\frac{\hbar}{2m\Omega} \right)^3 \end{aligned} \quad \dots (20)$$

In terms of the variable $\xi = \Omega/\omega_0$, and the parameter $\gamma = (3/2)(\hbar\beta/m\omega_0^3)$, the function to be minimized assumes the form:

$$f(\xi) = \left(\frac{2m}{\hbar\omega_0^3} \right) \epsilon^2 \equiv \xi^3 - 2\xi - 2\gamma + \frac{1}{\xi} + \frac{2\gamma}{\xi^2} + \frac{5\gamma^2}{3\xi^3} \quad \dots (21)$$

Setting $\partial f/\partial \xi = 0$ gives,

$$3\xi^6 - 2\xi^4 - \xi^2 - 4\gamma\xi - 5\gamma^2 = 0 \quad \dots (22)$$

Now the roots of the equation must lie close to those for the case $\gamma = 0$, i.e. near $\xi^2 = 1$ and $\xi^2 = -1/3$. The only relevant solution must, therefore, be of the form $\xi = 1 + \delta$, where δ is a small quantity of order γ .

Substituting in Eq. (22) and including terms up to second order in $\gamma(\delta)$, we get

$$32\delta^2 + (8 - 4\gamma)\delta - (4\gamma + 5\gamma^2) = 0 \quad \dots (23)$$

so that

$$\Omega = \omega_0(1 + \gamma/2 - \gamma^2/8) \quad \dots (24)$$

Taking the second derivative of Eq. (21) it is easily verified that the value obtained is indeed a minimum.

We can now compute the mean energy of the quartic oscillator at the absolute zero temperature as

$$\begin{aligned} \langle E \rangle &= 1/2m \langle \dot{x}^2 \rangle + 1/2m\omega_0^2 \langle x^2 \rangle + 1/4m\beta \langle x^4 \rangle \\ &= 1/2m \langle x^2 \rangle (\Omega^2 + \omega_0^2 + 3/2 \langle x^2 \rangle) \end{aligned} \quad \dots (25)$$

Making use of Eq. (24) and the fact that $\langle E_0 \rangle = 1/2\hbar\omega_0$ which is the mean zero-point energy of the unperturbed oscillator, we have

$$\begin{aligned} \langle E \rangle &= \langle E_0 \rangle (1 + \gamma/4 - \gamma^2/8) \\ &= \langle E_0 \rangle \left\{ 1 + \frac{3}{8} \frac{\hbar\beta}{m\omega_0^3} - \frac{18}{64} \left(\frac{\hbar\beta}{m\omega_0^3} \right)^2 \right\} \end{aligned} \quad \dots (26)$$

The above value for the mean energy in RED is to be compared with the value obtained in quantum mechanical perturbation theory given by

$$\langle E \rangle_{qm} = \langle E_0 \rangle \left\{ 1 + \frac{3}{8} \frac{\hbar\beta}{m\omega_0^3} - \frac{21}{64} \left(\frac{\beta\hbar}{m\omega_0^3} \right)^2 \right\} \quad \dots (27)$$

and the Stochastic Electrodynamics (SED) value of

$$\langle E \rangle_{SED} = \langle E_0 \rangle \left\{ 1 + \frac{3}{8} \frac{\beta\hbar}{m\omega_0^3} + \frac{141}{256} \left(\frac{\beta\hbar}{m\omega_0^3} \right)^2 \right\} \quad \dots (28)$$

obtained by Pesquera and Claverie¹⁵.

An evaluation of the absorption spectrum of the oscillator can be performed only after elucidating the stationary states of the oscillator in equilibrium with the Planck fields in addition to the ZPF. This would require the solution of transcendental equations instead of Eq. (22). However, the renormalization effect of the Planck fields on the optimal frequency will be negligible because of the smallness of the value of γ (i.e. $\omega_0^2 \gg 3\beta \langle x^2 \rangle$). We can thus conclude that at $T=0$, the first absorption peak for an applied small signal will occur at

$$\omega = \omega_0(1 + \gamma/2) \quad \dots (29)$$

to the first order in γ . This agrees with the quantum mechanical value and has again to be contrasted with the value Pesquera and Claverie¹⁵ had obtained through the linear response theory, i.e.

$$\omega = \omega_0(1 + \gamma/4) \quad \dots (30)$$

4 Discussion

The disagreement between Eq. (27) and Eq. (28) in the second order term even in sign is taken by Pesquera and Claverie to be one indication of the failure of SED. Now in quantum mechanics, as is well known, the first order term in Eq.(27) is the expectation of the

perturbing Hamiltonian in the unperturbed eigenstate of the linear oscillator while the second-order one results from the first-order correction to the wavefunction. Thus, it would appear that Pesquera and Claverie's method does not identify the correct quantum state of the system. On the other hand, that Eq.(26) is quite close to the quantum value is an indication that our generalized optimal determination of the frequency takes us quite close to the proper ground state of the system.

Pesquera and Claverie estimate the frequency as a function of the energy of undriven quartic oscillator for use in their Fokker-Planck type of equation. This parallels Rauscher's method of iteration¹⁶ which starts with the solution of the autonomous system as the first step. The agreement of their results for the energy at least up to the first order shows that the system is basically linear. The greater the deviation from linearity, the larger will be the error in the approach, as the atomic example shows: In the case of the hydrogen atom there is no zeroth approximation in which the orbital frequency is independent of the orbit size. The radiation forces must hence be of decisive importance in determining the mean frequency of the orbital motion. Planck's constant enters the frequency in the form $\mu e^4/\hbar^3$ whereas in the slightly anharmonic oscillator it appears in a small additive correction term:

$$\Omega = \omega_0 + 3\beta h/4 m\omega_0^2$$

In the atomic problem, the mean frequency and the mean size of the orbit must be determined at once from the full equation of motion incorporating the fields.

Thus the above discussion has served to highlight the importance of nonperturbatively incorporating the effect of the radiation fields on the natural frequencies of a nonlinear system. It would indeed be unrealistic to talk of absorption and emission by a nonlinear system

when all its possible states of stationary motion have not been elucidated by studying the equilibrium with the Planck radiation and the zero-point fields. The lack of detailed radiation balance in nonlinear systems noted by several workers¹⁵ is not likely to persist after such a study. We are encouraged in this attitude by another development, though it is not related to the nonlinear question. Several fundamental quantum concepts such as spin 1/2 and identical particle correlations, lying somewhat outside the mainstream of the developments in RED reported in the literature so far, have been shown to be related to the basic ideas of RED, in a preliminary report by Sachidanandam¹⁷. Also, work on the hydrogen atom is in progress and will be reported separately.

References

- 1 Marshall T W, *Proc R Soc London (GB)*, **284** (1963) 475.
- 2 Claverie P, Pesquera L & Soto F, *Phys Lett A (Netherlands)*, **80** (1980) 113.
- 3 Jackson J D, *Classical electrodynamics* (Wiley, New York) 2nd Edn, 1975, 786.
- 4 Milonni P W & Smith W A, *Phys Rev A (USA)*, **11** (1975) 814.
- 5 Heitler W, *Quantum theory of radiation* (Oxford, London) 3rd Edn, 1954, 26.
- 6 Landau L D & Lifshitz E M, *Classical theory of fields* (Pergamon Press, London), 1962, 231-5.
- 7 Jayaratnam C E, *Rev Mod Phys (USA)*, **19** (1947) 147.
- 8 Weisskopf V F, *Phys Rev (USA)*, **56** (1939) 72.
- 9 Welton T A, *Phys Rev (USA)*, **74** (1946) 1157.
- 10 Callen H B & Welton T A, *Phys Rev (USA)*, **33** (1951) 34.
- 11 Blaquier A, *Nonlinear system analysis* (Academic Press, New York) 1966, 13, 40, 186.
- 12 Boyer T H, *Phys Rev D (USA)*, **11** (1975) 790, 809.
- 13 Claverie P & Diner S, *Int J Quant Chem (USA)*, **12** (Suppl. 1) (1977) 41.
- 14 De la Pena-Auerbach L & Cetto A M, *J Math Phys (USA)*, **20** (1979) 469.
- 15 Pesquera L & Claverie P, *J Math Phys (USA)*, **23** (1982) 1315.
- 16 Ref. 11, p. 38.
- 17 Sachidanandam S, *BARC Rep.*, **1150** (Bhabha Atomic Research Centre, Bombay), 1981.

Evaluation of Spectroscopic Parameters for the Pr^{3+} Ion in a Laser Liquid

S V J LAKSHMAN* & S BUDDHUDU

Spectroscopic Laboratories, Department of Physics, S V University, Tirupati 517502

Received 4 May 1982

Radiative lifetimes are predicted for the fluorescent 3P_1 , 3P_0 and 1D_2 levels of Pr^{3+} in the laser liquid SeOCl_2 . Quantities such as squared reduced matrix elements, electric and magnetic dipole linestrengths, total radiative transition probabilities and radiative relaxation rates which are required for lifetime calculations are also reported.

1 Introduction

Experimental and certain theoretical investigations of the absorption spectra of a few lanthanides in SeOCl_2 at room temperature are available in the literature¹⁻³. Since radiative lifetimes for the fluorescent levels 3P_1 , 3P_0 and 1D_2 of the Pr^{3+} ion in SeOCl_2 laser liquid are not available, the authors took up calculation of these and the procedure followed and the results obtained are reported in the present paper.

2 Spectral Intensities

Theoretical estimates of intensities for the electronic excited states of the Pr^{3+} ion in a laser liquid are made following the methods of (a) Judd-Ofelt, and (b) Electric (S_{ed}) and magnetic (S_{md}) dipole linestrengths.

2.1 Judd-Ofelt Theory

Judd⁴ and Ofelt⁵ independently showed the oscillator strength of an induced electric dipole transition to be related to the energy of the transition $\nu(\text{cm}^{-1})$ and squares of the matrix elements of the unit tensor operator $\| U^\lambda \|$ connecting the initial and final states (ψJ and $\psi' J'$) via three phenomenological parameters T_λ ($\lambda = 2, 4$ and 6).

According to the theory,

$$S_{ed} = \sum_{\lambda=2,4,6} T_\lambda \nu (f^N \psi J \| U^\lambda \| f^N \psi' J')^2 \quad (1)$$

Evaluation of reduced matrix elements ($f^N \psi J \| U^\lambda \| f^N \psi' J'$) in the (I) LS coupling and (II) the intermediate coupling cases is as follows:

(I) LS COUPLING

The evaluation of the reduced matrix element is made using the formula:

$$(f^N \psi J \| U^\lambda \| f^N \psi' J') = (-1)^{S+L'+J+\lambda} [(2J+1)(2J'+1)]^{1/2} \times \left\{ \begin{array}{l} JJ' \lambda \\ L' LS \end{array} \right\} (f^N SL \| U^\lambda \| f^N SL') \quad (2)$$

The right hand side matrix elements of ($f^N SL \| U^\lambda \| f^N SL'$) are taken from the tables reported by Nielson and Koster⁶ and the values of the $6j$ symbol $\left\{ \begin{array}{l} JJ' \lambda \\ L' LS \end{array} \right\}$ (for $\lambda = 2, 4$ and 6) are taken from the tables reported by Rotenberg *et al.*⁷

(II) INTERMEDIATE COUPLING

The calculation of the reduced matrix elements in an intermediate field is illustrated for a typical transition like $^1D_2 \rightarrow ^3F_2$ belonging to $4f^2(\text{Pr}^{3+})$ configuration. The energy matrix for $J = 2$ is a 3×3 matrix given as^{8,9}:

$$\begin{vmatrix} |^3F_2\rangle & |^3F_2\rangle & |^1D_2\rangle & |^3P_2\rangle \\ |^3F_2\rangle & (15F_2 + 18F_4 - 24)^{1/2}\xi & -273F_6 - 4\xi & 0 \\ |^1D_2\rangle & -24^{1/2}\xi & (44F_2 - 48F_4 + 728F_6) & (18)^{1/2}\xi \\ |^3P_2\rangle & 0 & (18)^{1/2}\xi & (70F_2 + 84F_4 - 1274F_6 + \xi) \end{vmatrix} = 0$$

We write

$$\begin{aligned} |^1D'_2\rangle &= C_1|^3F_2\rangle + C_2|^1D_2\rangle + C_3|^3P_2\rangle \\ |^3F'_2\rangle &= C_4|^3F_2\rangle + C_5|^1D_2\rangle + C_6|^3P_2\rangle \end{aligned} \quad \dots (3)$$

where C_1, C_2, C_3, C_4, C_5 and C_6 are the eigenvectors corresponding to the intermediate fields $|^1D'_2\rangle$ and $|^3F'_2\rangle$ respectively. Now we have

$$\begin{aligned} (^1D'_2 \| U^\lambda \| ^3F'_2) &= [C_1|^3F_2\rangle + C_2|^1D_2\rangle + C_3|^3P_2\rangle] \\ &\quad + [C_4|^3F_2\rangle + C_5|^1D_2\rangle + C_6|^3P_2\rangle] \\ &= [C_1C_4 \langle ^3F_2 \| U^\lambda \| ^3F_2 \rangle + C_2C_5 \langle ^1D_2 \| U^\lambda \| ^1D_2 \rangle \\ &\quad + C_3C_6 \langle ^3P_2 \| U^\lambda \| ^3P_2 \rangle] \end{aligned} \quad \dots (4)$$

There will be no cross terms involving 3F_2 and 1D_2 , since the matrix elements between different spin states are zero.

The values of the reduced matrix elements $\langle ^3F_2 \| U^\lambda \| ^3F_2 \rangle$, $\langle ^1D_2 \| U^\lambda \| ^1D_2 \rangle$ and

$\langle ^3P_2 \parallel U^\lambda \parallel ^3P_2 \rangle$ in LS coupling are easily determined from Eq. (2). From these and the eigenvectors (C_1, C_2, C_3, C_4, C_5 and C_6) obtained by solving energy matrices^{8,9} the reduced matrix elements (${}^1D'_2 \parallel U^\lambda \parallel {}^3F'_2$) for the intermediate coupling case are calculated using Eq. (4). The reduced matrix elements are thus transformed from the LS basis states to the physical coupling scheme prior to being squared and substituted in Eq. (1). The squared values of Eq. (4) were substituted in Eq. (1) and using f_{expt} for f_{ed} the values of T_λ were evaluated by the least squares fit method. With these T_λ ($\lambda = 2, 4$ and 6) values, oscillator strengths $f_{\text{calc}}^{J=0}$ were calculated for the different transitions.

2.2 Method of Electric (S_{ed}) and Magnetic (S_{md}) Dipole Linestrengths

Theoretical spectral intensity (f^{e-m}) can be evaluated by the relation

$$f^{e-m} = \frac{8\pi^2 mc v}{3\hbar e^2 (J+1)} \left[\frac{(n^2 + 2)^2 S_{\text{ed}}}{9n} + n S_{\text{md}} \right] \quad \dots (5)$$

where n =refractive index of the medium, S_{ed} =electric dipole linestrength, S_{md} =magnetic dipole linestrength, m =mass of an electron, c =velocity of light, v =wavenumber of the band in cm^{-1} , \hbar =Planck's constant, e =electron charge in C, and J =value of the initial state J .

The value of S_{ed} then is given by:

$$S_{\text{ed}} = e^2 \left[1.085 \times 10^{11} \frac{n(n^2 + 2)}{9} \right]^{-1} \times (2J+1) \sum_{i=2,4,6} T_\lambda (f^N \psi J \parallel U^\lambda \parallel J' \psi' J')^2 \quad \dots (6)$$

The reduced matrix elements in Eq. (6) are transformed from the LS basis states to the physical coupling scheme prior to being squared. The value of S_{md} is then given by:

$$S_{\text{md}} = \frac{e^2 h^2}{16\pi m^2 c^2} (\psi J \parallel L + 2S \parallel \psi' J')^2 \quad \dots (7)$$

Values of $\|L + 2S\|^2$ are as given below (assuming the selection rule to be $\Delta J = 0 \pm 1$):

$$J' = J$$

$$(SLJ \parallel L + 2S \parallel SLJ') = gJ(J+1)(2J+1)$$

$$\text{where } g = 1 + \frac{J(J+1) + S(S+1) - L(L+1)}{2J(J+1)} \quad \dots (8)$$

$$J' = J - 1$$

$$(SLJ \parallel L + 2S \parallel SL, J-1)$$

$$= (S+L+J+1)(S+L+1-J)(J+S-L)(J+L-S) \quad \dots (9)$$

$$\begin{aligned} J' &= J + 1 \\ (SLJ \parallel L + 2S \parallel SL, J+1) &= \frac{1}{4(J+1)} [(S+L+J+2)(S+J+1-L) \\ &\quad (L+J+1-S)(S+L-J)] \end{aligned} \quad \dots (10)$$

The matrix elements calculated from Eqs (8)-(10) were transformed into the intermediate coupling scheme before computation of the magnetic dipole contribution represented by Eq. (7).

3 Results and Discussion

The absorption spectrum of Pr^{3+} in SeOCl_2 was measured by Heller¹. Using his results, eigenvalues and eigenvectors were evaluated by solving the energy matrices of $4^2(\text{Pr}^{3+})$ given by Dieke⁸ and Spedding⁹. The eigenvectors thus obtained were used in the calculation of squared reduced matrix elements $\|U\|^2$ between the electronic excited states ${}^3P_1, {}^3P_0, {}^1D_2$ and the next lower lying levels of Pr^{3+} in SeOCl_2 . S_{ed} and S_{md} values were evaluated from Eqs (6) and (7) respectively. Oscillator strengths were also calculated from the Judd-Ofelt and electric and magnetic dipole linestrengths methods.

Dieke⁸ has reported that ${}^3P_1, {}^3P_0, {}^1G_4$ and 3F_3 states would exhibit fluorescence in Pr^{3+} in LaCl_3 single crystals. Carnall *et al.*¹⁰ have pointed out that ${}^3P_1, {}^3P_0$ and 1D_2 states of Pr^{3+} exhibit fluorescence in LaF_3 solution. Since the present work is on solution spectra, radiative lifetimes for ${}^3P_1, {}^3P_0$ and 1D_2 excited states have been theoretically evaluated.

Carnall *et al.*¹¹ suggest that the total radiative transition probabilities (A) can be calculated using the Judd-Ofelt intensity parameters (T_λ) evaluated in absorption measurements. The authors have followed the same procedure in the calculation of A for the excited states ${}^3P_1, {}^3P_0$ and 1D_2 of Pr^{3+} in laser liquids.

The total radiative transition probability $A(\psi J; \psi' J')$ was calculated using the relation:

$$A(\psi J; \psi' J') = \frac{64\pi^4 v^3}{3\hbar(2J+1)} \left[\frac{n(n^2 + 2)^2}{9} S_{\text{ed}} + n^3 S_{\text{md}} \right] \quad \dots (11)$$

The total radiative relaxation rate (A_T) was evaluated using the formula:

$$A_T(\psi J) = \sum_{\psi' J'} A(\psi J; \psi' J') \quad \dots (12)$$

Table 1—Total Radiative Transition Probabilities (A), Radiative Relaxation Rates (A_T) and Predicted Radiative Lifetimes (τ_R) for the Levels of Pr^{3+} in $\text{SeOCl}_2 + \text{SnCl}_4$ and $\text{SeOCl}_2 + \text{SbCl}_5$

Transition		$A(\text{s}^{-1})$	
SLJ	$S'L'J'$	$\text{SeOCl}_2 + \text{SnCl}_4$	$\text{SeOCl}_2 + \text{SbCl}_5$
3P_1	3P_0	0.01	0.02
	1D_2	11.81	9.42
	1G_4	1104.89	301.66
	3F_4	3947.33	1978.05
	3F_3	23016.25	14501.97
	3F_2	12543.97	8554.72
	3H_6	6193.53	5208.98
	3H_5	17590.60	16665.70
3P_0	3H_4	8238.41	3929.60
	Value of $A_T(\text{s}^{-1}) \times 10^{-4}$	7.2646	4.5150
	Value of $\tau_R(\mu\text{s})$	13.77	22.15
3P_0	1D_2	21.53	17.22
	1G_4	1875.31	512.63
	3F_4	4034.62	2116.98
	3F_3	0	0
	3F_2	34573.33	22261.96
	3H_6	9777.77	8139.83
	3H_5	0	0
	3H_4	23075.97	10951.72
1D_2	Value of $A_T(\text{s}^{-1}) \times 10^{-4}$	7.3288	4.3940
	Value of $\tau_R(\mu\text{s})$	13.64	22.76
1D_2	1G_4	58.22.79	601.96
	3F_4	25909.15	3433.81
	3F_3	280.71	142.04
	3F_2	558.37	299.51
	3H_6	301.72	215.16
	3H_5	1394.76	1056.38
	3H_4	1993.67	1524.84
	Value of $A_T(\text{s}^{-1}) \times 10^{-4}$	3.6261	0.7273
Parameters	Value of $\tau_R(\mu\text{s})$	27.58	137.00
	n	1.515	1.601
	$T_2 \times 10^9$	1.977	1.156
	$T_4 \times 10^9$	1.026	0.419
	$T_6 \times 10^9$	1.463	1.627

where the sum runs over all $\psi'J'$ lower in energy than ψJ . The radiative lifetimes of a state is given as:

$$\tau_R(\psi J) = [A_T(\psi J)]^{-1} \quad \dots (13)$$

Total transition probabilities $A(\psi J; \psi'J')$, total radiative relaxation rates (A_T) and predicted lifetimes (τ_R) for the levels of Pr^{3+} in SeOCl_2 are presented in Table 1. It is interesting to note that the radiative lifetimes of fluorescent levels are much higher (about two times in 3P_1 , 3P_0 and five times in 1D_2) in the SbCl_5 complex than in the SnCl_4 complex.

Acknowledgement

One of the authors (SB) is thankful to CSIR, New Delhi, for awarding him a senior research fellowship.

References

- Heller A, *J Mol Spectrosc (USA)*, **28** (1968) 101.
- Tandon S P, Surana S S L & Mathur R C, *J Phys C (GB)*, **8** (1975) 2323.
- Lakshman S V J & Buddhudu S, *J Quant Spectrosc Radiat Transfer (USA)*, **24** (1980) 251.
- Judd B R, *Phys Rev (USA)*, **127** (1962) 750.
- Ofelt G S, *J Chem Phys (USA)*, **37** (1962) 511.
- Nielson C W & Koster G F, *Spectroscopic coefficients for pⁿ, dⁿ and fⁿ configuration* (MIT Press, Cambridge, Massachusetts), 1964.
- Rotenberg M, Bivins R & Metropolis W, *The 3j and 6j symbols* (MIT Press, Cambridge, Massachusetts), 1959.
- Dieke G H, *Spectra and energy levels of rare earth ions in crystals* (Interscience, New York), 1968.
- Spedding F H, *Phys Rev (USA)*, **58** (1940) 255.
- Carnall W T, Crosswhite H & Crosswhite H M, *Energy level structure and transition probabilities of trivalent lanthanides in LaF₃* (Argonne National Laboratory, Argonne, Illinois), 1978.
- Carnall W T, Hessler J P(Jr) & Wagner F J, *J Phys Chem (USA)*, **82** (1978) 2152.

NOTES

Indian Journal of Pure & Applied Physics
Vol 21, July 1983, pp. 416-417

Experimental Determination of the Neutral Level & Charge Density in the Interfacial Layer of a Schottky Barrier MIS Diode

A N DAW*, A K DATTA & M C ASH

Institute of Radio Physics & Electronics, Calcutta 700009

Received 26 November 1982; revised received 10 March 1983

Schottky barrier MIS diodes have been fabricated for two different values of interfacial layer thickness, by a chemical method with Ag, Cu, Ni and Pd as the barrier metals. The barrier heights of these contacts have been determined and utilising these data and the theory developed by the authors earlier, the neutral level (φ_0) and the charge present in the interfacial layer (Q_{0x}) of such diodes have been calculated.

In a recent paper¹, the authors have indicated a method for determining (i) the amount of fixed charge (Q_{0x}) in the interfacial layer of a MIS tunnel diode and (ii) the neutral level (φ_0) at the surface of the semiconductor with the help of the equations:

$$\varphi_{m01} = E_g + \chi_s - \frac{Q_{0x}}{qD_{S1}} \quad \dots (1)$$

and

$$\varphi_{m02} = E_g + \chi_s - \varphi_0 - \frac{Q_{0x}}{qD_{S2}} \quad \dots (2)$$

$$\frac{Q_{0x}}{qD_{S1}}$$

where φ_{m01} and φ_{m02} are the points of intersections of the theoretical line $\varphi_{Bn} = \varphi_m - \chi_s$ with the plots of the experimental values of φ_{Bn} versus φ_m of number of MIS contacts. There will be two points of intersection between the experimental and theoretical lines since there are two experimental curves, each corresponding to a particular value of interfacial layer thickness (δ) and surface state density (D_s). In the above equations, E_g and χ_s represent respectively the bandgap and electron affinity of the semiconductor and D_{S1} and D_{S2} the densities of states at the surface of the semiconductor for two different layers of oxide thickness (δ). Since the values of D_{S1} and D_{S2} can be easily calculated from the slopes of the φ_{Bn} versus φ_m plot, it follows that Q_{0x} and φ_0 can be determined from Eqs (1) and (2), provided E_g and χ_s are known and φ_{m01} and φ_{m02} are experimentally measured.

Based on the above principle, an attempt has been made in this laboratory to determine the values of Q_{0x} and φ_0 experimentally for an epitaxial silicon surface on which several metals were deposited

chemically. For the purpose of this experiment four metals, viz. Ag, Cu, Ni and Pd were selected for deposition on *n*-type epitaxial silicon wafers having an epi-layer thickness and resistivity of 20 μm and 4-6 ohm-cm respectively. The wafer surface was etched and cleaned in the usual way². Oxide layers were then grown on the epi-layer by two different methods, one by boiling the wafer in conc. HNO_3 for 20 min following the technique already reported^{3,4} and the other by heating the sample in an atmosphere of dry oxygen at a temperature of 450°C for 45 min. The oxide thicknesses were measured by an ellipsometer and found to be about 25 and 60 Å respectively. The four metals mentioned above were then deposited selectively using the chemical reduction and electroless process described earlier^{2,5}.

The barrier heights of the contacts thus formed were measured by both *I-V* and *C-V* techniques. The mean values of these measurements were plotted against φ_m (Fig. 1), curve a being for $\delta \approx 25 \text{ \AA}$ and curve b for $\delta \approx 60 \text{ \AA}$. The work function values⁶ were Ag(4.31 eV), Ni(4.74 eV), Cu(4.52 eV) and Pd(4.95 eV). On the same plot, the theoretical curve obeying the relation $\varphi_{Bn} = \varphi_m - \chi_s$ (assuming χ_s to be 4.05 eV) was also drawn. From the intersection of the latter curve with the curves a and b, φ_{m01} and φ_{m02} were obtained as 4.78 eV and 4.77 eV respectively. From the experimental plot of φ_{Bn} versus φ_m (curve a and curve b), D_{S1} and D_{S2} were found to be 1.26×10^{13} states/cm⁻²eV and 1.13×10^{13}

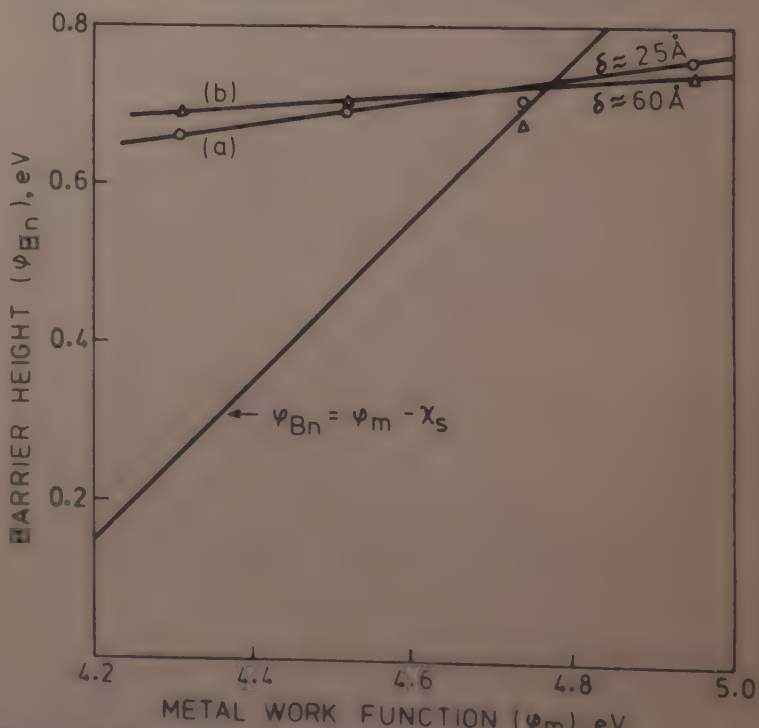


Fig. 1 Experimental plots of barrier height values (φ_{Bn}) as a function of work-function (φ_m) of the metals deposited on two surfaces having different values of interfacial layer thickness (δ) and surface state densities and theoretical curve of $\varphi_{Bn} = \varphi_m - \chi_s$

states/cm⁻²eV respectively. Substituting these values in Eqs.(1) and (2), Q_{0r} and φ_0 were obtained as 1.0×10^{12} charges cm⁻² and 0.31 eV respectively.

The above method thus appears to be a simple one for measuring the charge in the oxide layer of a MIS tunnel diode. An examination of the experimentally obtained curves (Fig.1) also reveals that below a particular value of the metal work-function ($\varphi_m = 4.68$ eV), the barrier height for larger values of interfacial layer thickness is more compared to that for smaller thickness. This trend is reversed for work-function values above this φ_m value.

References

- 1 Daw A N, Datta A K & Ash M C, *Solid St Electron (GB)*, **25** (1982) 431.
- 2 Datta A K, Ghosh K, Mitra R N & Daw A N, *Solid St Electron (GB)*, **23** (1980), 99.
- 3 Ponpon J P, Stuck R & Siffert P, *Proc 12th IEEE Photo Spec Conf (USA)*, (1976) 900.
- 4 Oakley R E & Godber G A, *Thin Solid Films (Switzerland)*, **9** (1972) 287.
- 5 Ghosh K, Datta A K, Chowdhury N K D & Daw A N, *Indian J Pure & Appl Phys*, **20** (1982) 308.
- 6 Riviere J C, *Proc Phys Soc London Ser B (GB)*, **70** (1957) 676.

Effect of Thickness on the Electrical Properties of AlSb Thin Films

S M PATEL & A M BIRADAR*

Department of Physics, Sardar Patel University, Vallabh Vidyanagar, Gujarat 388 120

Received 4 October 1982

Aluminium antimonide thin films of different thicknesses were prepared using co-evaporation method. The variations, with film thickness, of the Hall coefficient R_H , Hall mobility μ_H , and carrier concentration η , have been determined. It is observed that with increase in the film thickness the mobility of the carriers increases whereas the carrier concentration decreases. The maximum carrier mobility observed in the present study is $15 \text{ cm}^2 \text{ V}^{-1} \text{ s}^{-1}$ on the thickest film ($t=8000 \text{ \AA}$) with lowest carrier concentration of $7 \times 10^{17} \text{ cm}^{-3}$.

Effect of the thickness on the electrical properties of vacuum deposited AlSb films is dealt with in this note.

Aluminium antimonide films were prepared by co-evaporation method as described by Francombe *et al.*¹ All the deposition parameters such as substrate temperature, substrate, vacuum, etc. were held constant to study the effect of the film thickness on their electrical properties. The film geometry used for the Hall measurements was similar to that given by Goswami and Ojha². For the Hall measurements, a uniform magnetic field of 9000 G as measured by a gaussmeter was applied. The Hall voltage was measured with digital multimeter by changing the magnetic field and sample current directions. The film resistance was calculated from the voltage drop across them and the current flowing through them. For electrical contacts in all cases, thick silver films were deposited over the Hall and resistivity probes from which pressure contacts were made. The contacts were found to be ohmic.

Fig. 1 shows a plot of the variation of Hall constant R_H against the thickness of the films. It is observed that the Hall constant increases slowly with increase in the film thickness in the range 2000-5000 \AA , but more rapidly in the range 5000-8000 \AA . Fig. 2 shows the variation of $\log R$ with reciprocal of temperature for the film deposited at 550 C. The activation energy was calculated from the slope of the curve. The carrier concentration η was determined from the free carrier relation,

$$\eta = \frac{1}{R_H \cdot \rho}$$

* Present address: National Physical Laboratory, Hillside Road, New Delhi 110012

and the Hall mobility was calculated using the relation,

$$\mu = R_H \cdot \sigma$$

where σ is the measured conductivity. Fig. 3 shows the variation of η and μ with thickness. It is observed that the mobility of the carriers increases with increase in the film thickness whereas the carrier concentration decreases.

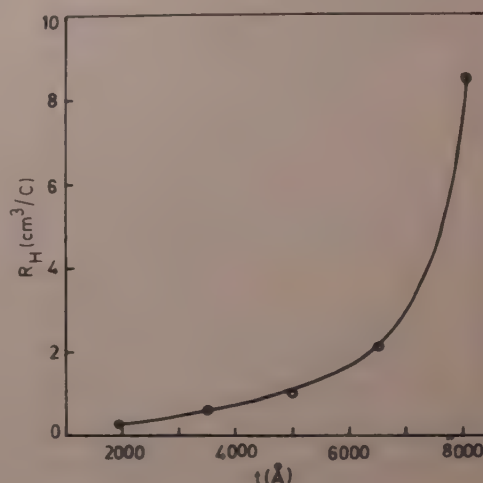


Fig. 1—Hall constant (R_H) versus thickness of the films (t)

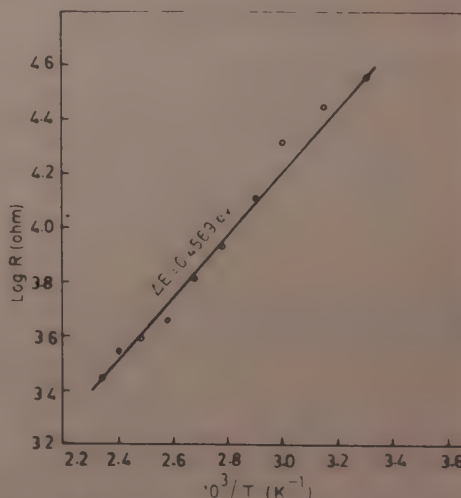


Fig. 2— $\log R$ versus $1/T$ for the film deposited at 550 C

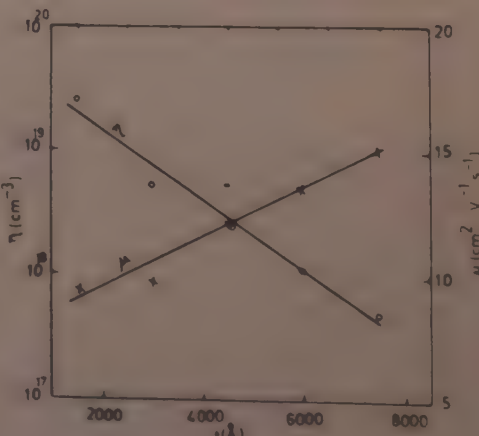


Fig. 3—Carrier concentration (η) and mobility (μ_H) versus thickness (t) of the films

The change in the electrical properties of vacuum-deposited thin film with varying thicknesses has been attributed mainly to the deterioration of the structural perfection. The electron microscopic observations show that the films prepared at the substrate temperature of 550°C were polycrystalline in nature. At lower thicknesses ($t < 1000 \text{ \AA}$) the crystallites would be smaller in size and are linked with the amorphous or polycrystalline material which offers high resistance. However, as film thickness increases, the size of the crystallites also increases and intercrystalline material offers less resistance and hence the conductivity of the film increases.

It has been observed in the case of InAs single crystals³ that the mobility dropped sharply when the carrier concentration varied from 1.7×10^{16} to $2 \times 10^{18} \text{ cm}^{-3}$. Fig. 3 also shows, an increase in the carrier concentration with a decrease in the thickness which ultimately results in a decrease in the carrier mobility in the films. It may be mentioned that the carrier mobility in films drops with increasing carrier concentration more vigorously than in single crystals. This can be due to the presence of scattering effect in the films, whose contribution increases with decreasing film thickness. Similar observations have been reported by Wieder⁴ in the case of InAs films, i.e., a decrease in the film thickness results in an increase in the dislocation density which increases the dislocation scattering. It is also possible that the mobility may decrease as a result of the effect of surface levels. This may be predominant

in thinner films. It has been reported⁵ that the mobility decreases when the thickness of silicon samples is reduced by etching from 60 to 20μ .

Thus the increase in the carrier mobility with increase in film thickness can be attributed to a decrease in the carrier concentration, by a decrease in the intercrystalline barriers and dislocation scattering. The carrier concentration drops from $9 \times 10^{19} \text{ cm}^{-3}$ at 2000 \AA thickness to $7 \times 10^{17} \text{ cm}^{-3}$ at 8000 \AA . The mobility of the carriers increases with an increase in thickness and a maximum carrier mobility of $15 \text{ cm}^2 \text{V}^{-1} \text{s}^{-1}$ is observed during the present study on the thickest film ($t = 8000 \text{ \AA}$) with the lowest carrier concentration of $7 \times 10^{17} \text{ cm}^{-3}$.

The authors are indebted to Profs A R Patel and G K Shivakumar for valuable discussions. Thanks are also due to Drs S Chandra and C P Sharma of the National Physical Laboratory, New Delhi for useful discussions. One of the authors (AMB) is grateful to the University Grants Commission, New Delhi for the award of a Junior Research Fellowship.

References

- 1 Francombe M H, Noreik A J, Zeitman S A & Johnson J E, *Thin Solid Films (Switzerland)*, **32** (1976) 259.
- 2 Goswami A & Ojha S M, *Thin Solid Films (Switzerland)*, **16** (1973) 189.
- 3 Harman C, Goering H L & Beer A C, *Phys Rev (USA)*, **104** (1956) 1562.
- 4 Wieder H, *Solid-State Electron (GB)*, **9** (1966) 373.
- 5 Kontseva Yu & Malyshev M I, *Sov Phys Solid State (USA)*, **8** (1966) 288.

Thickness Dependence of Electrical Resistivity of Vacuum-deposited Selenium Films[†]

ARUN K SHARMA* & B SINGH[‡]

Vacuum Tubes Division, Central Electronics
Engineering Research Institute,
Pilani 333 031

Received 11 October 1982

Thickness dependence of electrical resistivity of vacuum deposited selenium films (thickness, 500 to 4420 Å) has been reported in vacuum, after an annealing cycle (30 to 150°C and back) and in residual vacuum after 24 hr. Unusual increase of electrical resistivity from 500 to 3400 Å thickness has been explained in terms of localized surface states.

The electrical conduction of thick amorphous selenium films has been reported to be space-charge limited^{1,2} and in the lower temperature range (-100 to 20°C) it has been found to be polaronic³. Oxygen is known to increase the conductivity of pure selenium by many orders of magnitude in presence of even 50 ppm molecules of oxygen^{4,5}. In the present note, we explain the observed unusual increase in electrical resistivity of vacuum deposited selenium films with increasing thickness in vacuum, after an annealing cycle and then in residual vacuum after 24 hr.

Specimens have been prepared by thermal evaporation of Se-powder of 99.5% purity onto cleaned glass substrates from a molybdenum boat in 3×10^{-5} Torr vacuum at room temperature (30°C). The rates of deposition and film thickness have been 5 Å/sec and 500 to 4420 Å respectively. Area of the films, 0.2 mm × 25 mm has been obtained by shadowing the substrate by a copper wire during silver contact deposition. Leads from the silver contacts have been taken with the help of cleaned spring clips. Stable values of electrical resistance have been measured just after deposition, after an annealing cycle (30 to 150°C and back) and in residual vacuum after 24 hr. Stable values of electrical resistance just after deposition have been attained in about 50 min. Rate of heating and cooling during annealing has been about 0.5°C/min.

Fig. 1 shows a typical behaviour of electrical resistivity in the selenium films as a function of film

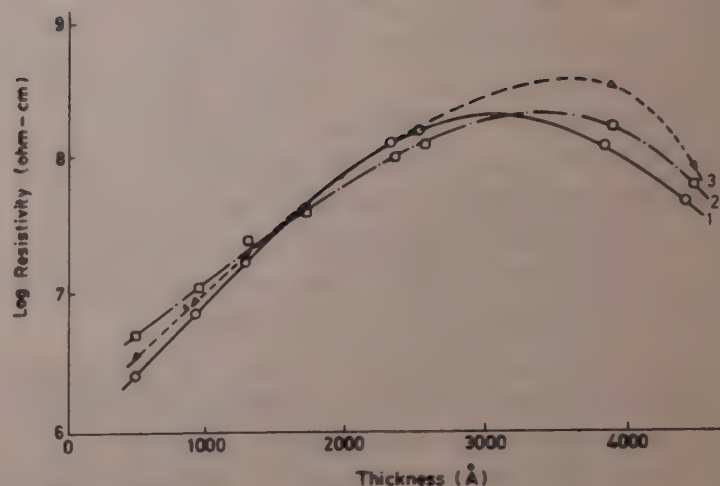


Fig. 1—Electrical resistivity versus thickness [Curve: 1, stable value after film deposition; 2, after an annealing cycle; and 3, after 24 hr in residual vacuum]

thickness. Electrical resistivity increases with thickness up to 3400 Å and thereafter decreases. The initial increase in resistivity with film thickness is in contradiction to the thin film size-effect theory^{6,7}. This unusual behaviour could be understood in terms of localized surface states, having energy distributed in the forbidden energy gap. These localized surface states exist due to chemisorption of oxygen molecules from environment, i.e. 2×10^{-6} Torr partial pressure of oxygen⁸ and non-crystalline structure of the specimens. These, in turn, cause statistical fluctuations in thinner region and form conducting channels, which are responsible for unusual behaviour below 3400 Å thickness⁹. For films thicker than 3400 Å, variation of resistivity is dominated by the size-effect on electron free path in the bulk and thus resistivity decreases thereafter.

No significant changes in the magnitudes of electrical resistivities of selenium films have been found for the following 3 conditions, viz. just after vacuum deposition (curve 1), after an annealing cycle (curve 2) and in residual vacuum after 24 hr (curve 3). This could be due to adequate chemisorption of oxygen molecules during film deposition. In the present study, the films have been deposited in an environment of 3×10^{-5} Torr pressure (i.e. in presence of $\approx 2.2 \times 10^{15}$ oxygen molecules striking per unit area of the substrate per second). LaCourse *et al.*⁴ have found that even 50 ppm of oxygen molecules reduce electrical resistivity of pure selenium (10^{17} ohm-cm) by six orders of magnitude. And our films have electrical resistivities in the range 10^7 to 10^9 ohm-cm, which confirms adequate chemisorption of oxygen molecules.

*Work done at Thin Films Laboratory, Physics Department, University of Jodhpur, Jodhpur 342 001

[†]Present address: Department of Physics, King Faisal University, Saudi Arabia

NOTES

References

- 1 Hartke J L, *Phys Rev (USA)*, **125** (1962) 1177.
- 2 Lanyon H P D & Spear W E, *Proc Phys Soc London (GB)*, **77** (1961) 1157.
- 3 Vautier C, Carles D & Viger C, *J Non-Cryst Solids (Netherlands)*, **7** (1972) 117.
- 4 LaCourse W C, Twadell V A & Mackenzie J D, *J Non-Cryst Solids (Netherlands)*, **3** (1970) 234.
- 5 Twadell V A, LaCourse W C & Mackenzie J D, *J Non-Cryst Solids (Netherlands)*, **8-10** (1972) 831.
- 6 Fuchs K, *Proc Camb Phil Soc (GB)*, **34** (1938) 100.
- 7 Sondheimer E H, *Adv Phys (GB)*, **1** (1952) 1.
- 8 Glang R, Holmwood R A & Kurtz J A, in *Handbook of thin film technology*, edited by L I Maissel & R Glang (McGraw-Hill, New York) 1970, 2-19.
- 9 Mott N F & Davis E A, *Electronic processes in non-crystalline materials* (Clarendon Press, Oxford) 1971, 22.

Preparation of Multialkali Antimonide Photocathode

R L VERMA* & R C BAPNA

Laser Section, Bhabha Atomic Research Centre, Bombay 400 085

Received 16 August 1982; revised received 28 December 1982

A method for preparing multialkali photocathode starting with an antimony layer possessing island structure is described. The photocathode thus formed is found to be more sensitive in the near infrared region than that prepared by the conventional method. A reproducible photocathode with average yield of $160 \mu\text{A}/\text{lm}$ and having long wavelength threshold at 870 nm is obtained.

Since the discovery of multialkali photocathode, $\text{CsNa}_2\text{K}\text{Sb}$, by Sommer¹ in 1955, various methods of preparing the photocathode have been reported²⁻⁴. Efforts have been made in past to enhance the sensitivity of the photocathode in the near infrared region with a view to exploiting the predominance of infrared photons over the visible ones in the night sky radiation². Variation in the sequence of introduction of alkali vapours and different conditions of activation have been tried. Most of the methods have a common feature in that preparation of photocathode starts with the deposition of an Sb layer of controlled thickness which is then treated with different alkali vapours. Among the conventional photocathodes, $\text{Ag}-\text{O}-\text{Cs}$ has the longest threshold extending up to $1.1 \mu\text{m}$ (Ref. 5). This photocathode layer is known to consist of islands rather than being a smooth layer⁶. Takahashi⁷ reported that the photocathodes prepared with initial antimony (Sb) layer in the form of a mosaic film rather than a smooth one had greater efficiency in the near infrared region of the spectrum. This note presents our experimental results on photocathode prepared from Sb layers having island structure.

The photocathodes were deposited on a plain glass window attached to one end of a diode. The photocathodes were processed on an all-glass mercury-diffusion-pump-system which maintained a pressure of $\approx 1 \times 10^{-7}$ Torr during processing of photocathodes. An ion gauge, based on the phenomenon of thermal ionization of alkali atoms hitting an incandescent filament, was used for monitoring the partial pressure of alkalis during activation of the cathode. The details of construction of the diode and the experimental set-up have been reported elsewhere⁸.

After assembly, the diode was heated at 300°C overnight for 18 h during which it was continuously pumped. When cooled subsequently to room

temperature the pressure in the system was registered 8×10^{-8} Torr. Alkali generators were then degassed and the diode was again heated at 275°C for a further period of 18 h and then cooled to room temperature. An Sb film having 30% light transmission was deposited on the glass substrate at room temperature. The diode was then heated to 250°C for about 15 min. The light transmission through the Sb layer increased, indicating thereby breaking-up of the smooth Sb layer into islands. Additional Sb was evaporated on the substrate till the light transmission of the film decreased by about 10%. The Sb film thus formed was treated with alkali vapours as follows: The diode temperature was raised to 180°C and potassium (K) was generated by resistance heating of the K-generator. White light from a calibrated tungsten lamp was utilized to monitor the photoyield of the photocathode. The variations of photocurrent and alkali ion current during the fabrication of photocathode are shown in Figs. 1 and 2 respectively. When the photosensitivity tended to fall off the peak attained by K-activation, the diode temperature was raised to 200°C and sodium (Na) vapours were generated by heating the Na-generator. Sensitivity of the cathode then attained a new peak. As the sensitivity began to fall from the second peak, the photocathode substrate was air cooled to allow as much Na and K as possible to stick to the photocathode. Na- and K-generators were switched off when the photocathode current fell to $1/3$ of the second peak. Sb was evaporated at that stage to increase the sensitivity. Subsequently, the photocathode was cooled by putting off the furnace. It was observed that sensitivity dropped to zero at room temperature. The tube was baked again and when the temperature was again raised to 100°C , potassium was generated. When the sensitivity attained a peak, Sb was evaporated on to the cathode till the sensitivity reduced to $1/3$ of the peak. The sensitivity again attained a new peak. Again it was reduced to $1/3$ of the peak by evaporating additional Sb. K-Sb cycles were repeated in order to maximize the sensitivity. After obtaining the peak, the temperature of the tube was raised to 200°C and addition of Na was started. The evaporation of Na was continued till the photocathode sensitivity dropped to almost zero. The diode was then cooled to 160°C and K-Sb cycles were repeated to get maximum photoyield. K-generator was then switched off. Cesium (Cs) vapours were then generated. When the sensitivity started falling from the peak, evaporation of Sb at a controlled rate was started. After reaching the

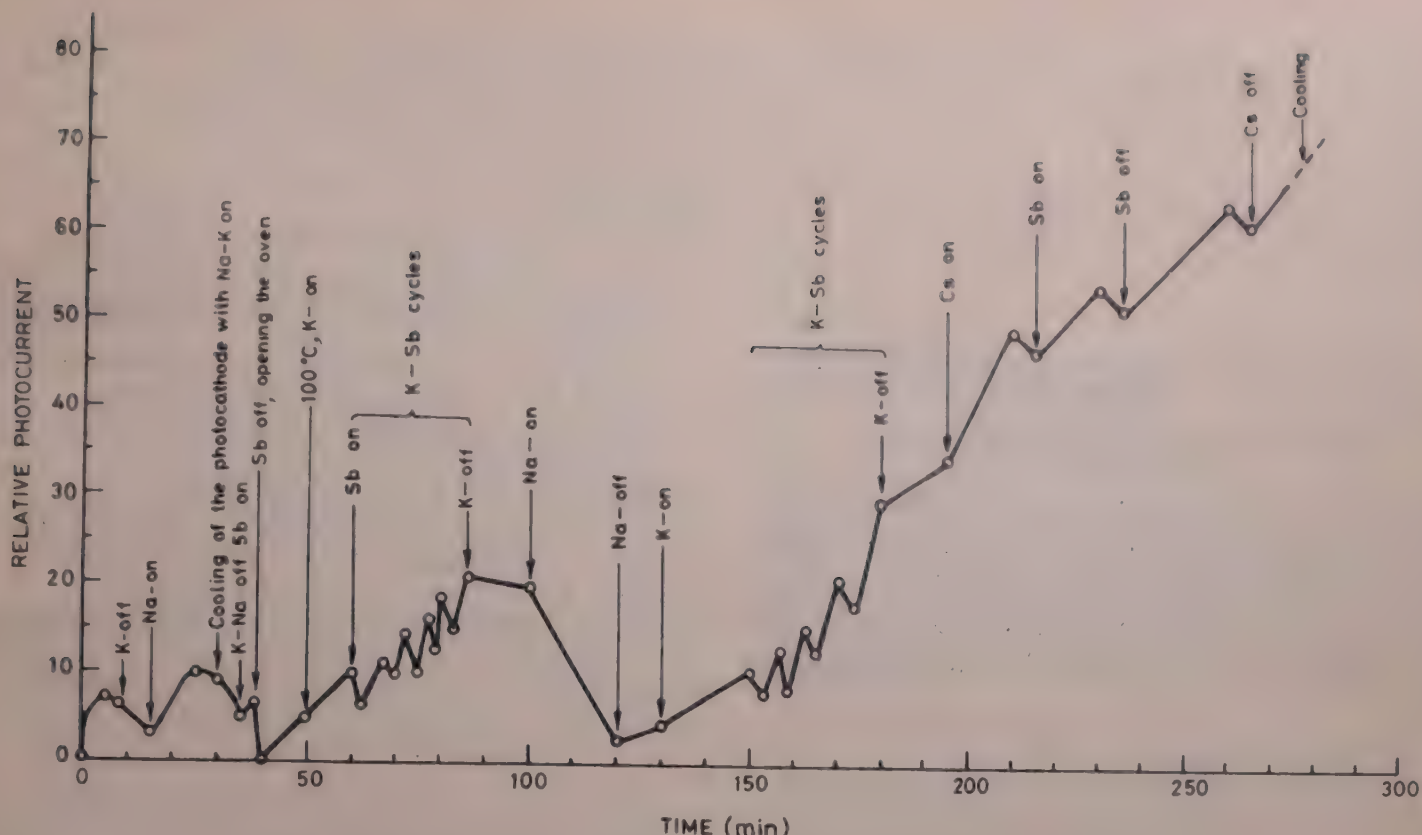


Fig. 1—Variation of photocurrent with time during the processing of photocathode

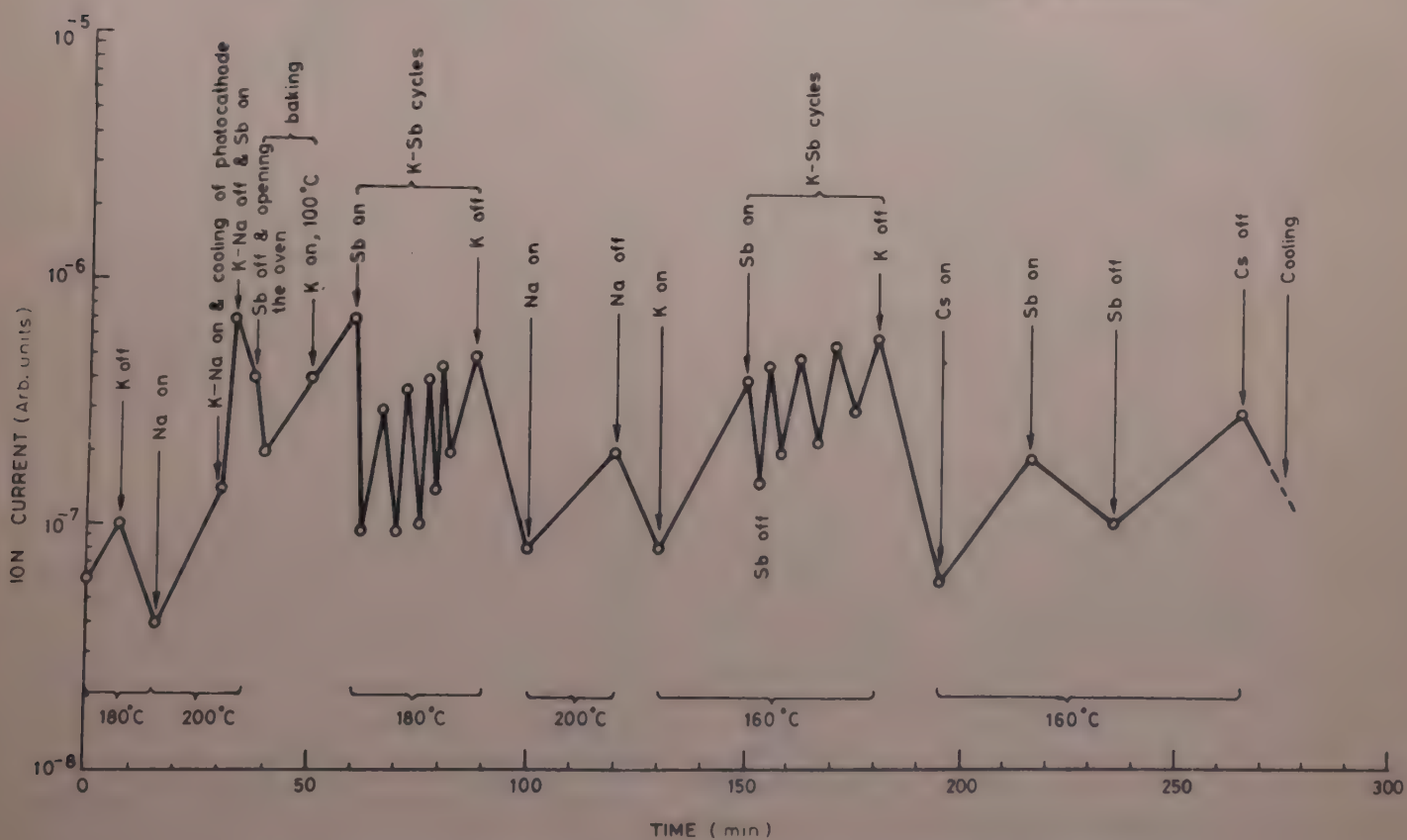


Fig. 2—Variation of ion current with time during the processing of photocathode

peak. Sb-evaporation was stopped. The photocathode was allowed to overcesiate for sometime and the Cs-generator was then switched off. The diode was allowed to cool to room temperature. On cooling, the photocathode sensitivity normally increased further.

Ten diodes were processed by this method. The photoyield was found to vary between 150 and 180 $\mu\text{A}/\text{Im}$. Even under seemingly identical activation

conditions regarding alkali vapour pressure and temperature of processing, photoyield of K-Sb layer was found to vary from sample to sample. Similar behaviour of K-Sb films has been reported by several workers^{9,10}. K_3Sb compound is known to possess two types of crystal structure, namely, cubic and hexagonal; the former has *p*-type conductivity and the latter *n*-type. In our experiments, the K-Sb layer was

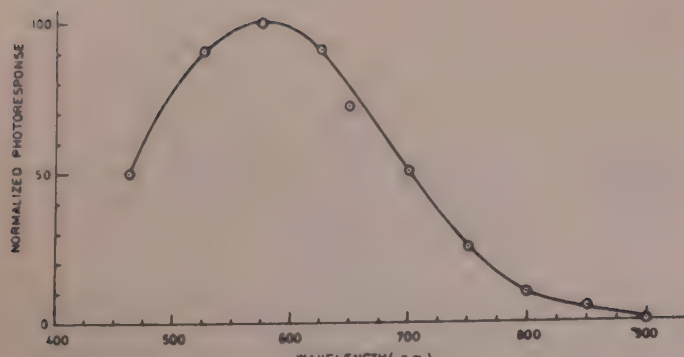


Fig. 3—Spectral response of the photocathode

found to have *n*-type conductivity. The photoyield of such a layer is known to vary due to the variation of the excess of alkali metal present in the layer¹¹. Fig. 3 shows the normalized spectral response of a typical photocathode. As shown in Fig. 3, quantum efficiency

of the photocathode peaks at 570 nm, and the long wavelength threshold lies at 870 nm as compared with those reported by Sommer having peak at 510 nm and threshold at 820 nm (Ref. 11).

References

- 1 Sommer A H, *Rev Sci Instrum (USA)*, **26** (1955) 725.
- 2 Varma B P & Ghosh C, *Indian J Pure & Appl Phys*, **13** (1975) 15.
- 3 Garfield B R C, *Adv Electron & Electron Phys (USA)*, **33A** (1972) 339.
- 4 Dowman A A, Jones T H & Beck A H, *J Phys D (GB)*, **8** (1975) 69.
- 5 Koller L R, *Gen Elect Rep (USA)*, **31** (1928) 426.
- 6 Pakhmov M T & Malamid A F, *Izv Akad Nauk SSSR (USSR)*, **35** (1971) 307.
- 7 Takahashi S, *N H K Tech J (Japan)*, **29** (1977) 1.
- 8 Verma R L & Bapna R C, *Vacuum (GB)*, **30** (1980) 483.
- 9 Ebina A & Takahashi T, *Phy Rev B (USA)*, **7** (1973) 7.
- 10 Shiraki H, *Jpn J Appl Phys (Japan)*, **4** (1965) 238.
- 11 Sommer A H, *Photoemissive materials* (John Wiley, New York), 1968, 119.

Modified Gell-Mann-Okubo Mass Formula in the (8,8) Model

T N TIWARI* & C V SASTRY†

Department of Physics, Regional Engineering College, Rourkela
769 008

and

(Mrs) SAROJ SHARMA

Department of Physics, Deva Nagari (Post-Graduate) College,
Meerut 250 002

Received 8 October 1982

A modified version of the famous Gell-Mann-Okubo mass formula for the pseudoscalar mesons has been derived from the (8,8) model of the broken chiral $SU(3) \otimes SU(3)$ symmetry. This modified formula agrees with the experimental data to within 0.4%, which is much better compared to 6.3% for the original formula.

The successes of the $SU(3)$ symmetry in hadron physics are well known¹ and need not be recounted here. It was realized later by Gell-Mann and others that the strong interactions are approximately invariant also under the larger group $SU(3) \otimes SU(3)$. For the symmetry breaking piece of the Hamiltonian, the most popular and successful model was the $(3,3^*) \oplus (3^*,3)$ representation^{2,3} of $SU(3) \otimes SU(3)$.

However, it soon became apparent in the early seventies that the conventional $(3,3^*) \oplus (3^*,3)$ model cannot successfully account for certain experimental data, e.g. the meson-meson scattering lengths, meson-meson σ -terms, the amplitude for the $\eta \rightarrow 3\pi$ decay, etc. To remedy this situation, we propose the (8,8) representation of $SU(3) \otimes SU(3)$ as a promising alternative to the $(3,3^*) \oplus (3^*,3)$ model. The present authors have investigated the (8,8) model and carried out several calculations using it⁴⁻⁷ with encouraging results. In this note, we exploit the (8,8) model to derive a modified version of the famous Gell-Mann-Okubo mass formula⁸ for the pseudoscalar mesons. The formula derived here shows much better agreement with the experimental data than the original formula.

Our approach is similar to that of Cicogna and coworkers⁹ who analyzed in detail the consequences of the chiral symmetry breaking and discussed the results which follow simply from the $(3,3^*) \oplus (3^*,3)$ model. For simplicity, we consider the case in which the field theory is described by a Lagrangian $L(x)$ given by

$$L(x) = L_0(x) + d_i \varphi_i(x) \quad \dots (1)$$

where $L_0(x)$ is invariant under the given group G , d_i are the real constants and $\varphi_i(x)$ are the basic local fields in

terms of which the Lagrangian is constructed and which transform locally as a representation of the group G as

$$\varphi_i(x) \rightarrow g_{ij}^\alpha \varphi_j(x) \quad \dots (2)$$

Here g_{ij}^α is the matrix representation of the generator G^α in the vector space spanned by the local fields $\varphi_j(x)$.

Now we introduce the notation

$$\lambda = \lambda_i \hat{\varphi}_i, \quad d = d_i \hat{\varphi}_i \quad \dots (3)$$

where $\hat{\varphi}_i$ is the unit vector in the direction i , and λ_i are the vacuum expectation values of the local fields $\varphi_i(x)$ and are given by

$$\lambda_i = \langle 0 | \varphi_i(x) | 0 \rangle \quad \dots (4)$$

With this notation, and using the functional method to treat the spontaneous breaking of symmetries in quantum field theory, it can be shown that the second-order Ward-identity can be written in the basis in which the mass matrix is diagonal in the form⁹

$$m_i^2 [G^\alpha, \lambda]_i = [G^\alpha, d]_i \quad \dots (5)$$

where m_i^2 is the squared mass of the particle i .

In the (8,8) model, the local fields $\varphi_i(x)$ are denoted by the symbols Z_α and \bar{Z}_α . They are defined in the suggestive form of the products of $SU(3) \otimes SU(3)$ currents⁴ as follows:

$$\begin{aligned} Z_0 &= (1/2\sqrt{2})(V - A)_\beta^\mu (V + A)_{\mu\beta} \\ Z_\alpha &= (\sqrt{3}/\sqrt{5})d_{\alpha\beta\gamma}(V - A)_\beta^\mu (V + A)_{\mu\gamma} \\ \bar{Z}_\alpha &= (1/\sqrt{3})f_{\alpha\beta\gamma}(V - A)_\beta^\mu (V + A)_{\mu\gamma} \end{aligned} \quad \dots (6)$$

with $\alpha, \beta, \gamma = 1, 2, \dots, 8$; $\mu = 0, 1, 2, 3$.

In Eq. (6), the fields Z_0 and Z_α belong, respectively, to the singlet and the even-parity octet in the $SU(3)$ decomposition of $8 \otimes 8$, while \bar{Z}_α belongs to the odd-parity octet. The fields Z_α correspond to the scalar 0^+ mesons, while the fields \bar{Z}_α correspond to the pseudoscalar 0^- mesons.

The strong interaction Hamiltonian H can be written as

$$H = H_0 + H' \quad \dots (7)$$

where H_0 is $SU(3) \otimes SU(3)$ invariant, while H' , which breaks this symmetry, can be written in terms of the fields given in Eq. (6), as

$$H' = d_0 Z_0 + d_8 Z_8 \quad \dots (8)$$

In Eq. (8), d_0 and d_8 are the symmetry-breaking parameters. We have chosen the above form of symmetry breaking to satisfy the requirements of the conservation of isospin and hypercharge for the strong interactions.

Now we utilize the Hamiltonian of Eq. (7) in the second-order Ward identity of Eq. (5) to derive the

*Department of Mathematics, Regional Engineering College, Rourkela 769 008

expressions for the squared masses of the pseudoscalar mesons⁴. By using the appropriate generators for the mesons π , K and η and evaluating the commutators of Eq.(5), we get

$$\begin{aligned} m_\pi^2 &= \frac{\sqrt{10}d_0 + 2\lambda_8}{\sqrt{10}\lambda_0 + 2\lambda_8} \\ m_K^2 &= \frac{\sqrt{10}d_0 - \lambda_8}{\sqrt{10}\lambda_0 - \lambda_8} \\ m_\eta^2 &= \frac{\sqrt{10}d_0 - 2\lambda_8}{\sqrt{10}\lambda_0 - 2\lambda_8} \end{aligned} \quad \dots (9)$$

Moreover, the expressions for the decay constants F_i of the pseudoscalar mesons can be obtained easily⁴ by combining the hypothesis of the partial conservation of axial-vector currents (PCAC) with the Ward identity of Eq.(5). This gives:

$$\begin{aligned} F_\pi &= C(\sqrt{10}\lambda_0 + 2\lambda_8) \\ F_K &= C(\sqrt{10}\lambda_0 - \lambda_8) \\ F_\eta &= C(\sqrt{10}\lambda_0 - 2\lambda_8) \end{aligned} \quad \dots (10)$$

where

$$C = (3\sqrt{3}/10)$$

Combining Eqs (9) and (10), we get the remarkable relation

$$4F_K M_K^2 = 3F_\eta m_\eta^2 + F_\pi m_\pi^2 \quad \dots (11)$$

which is the modified Gell-Mann-Okubo mass formula obtained from the (8,8) model. We note here that this relation is not new. It was obtained previously by several workers using various approaches. But it is for the first time that it has been derived from the (8,8) model and this shows once again that the (8,8) model may prove to be a promising alternative to the more popular (3,3*) \oplus (3*,3) model.

The original Gell-Mann-Okubo mass formula was derived in terms of linear masses from the $SU(3)$ symmetry and proposed in the form

$$4m_K = 3m_\eta + m_\pi \quad \dots (12)$$

But the agreement obtained using this relation with the latest experimental data on the masses is very poor. It turns out that if we substitute the average experimental masses in Eq.(12), it is satisfied to within 10.6%.

The agreement can be improved to some extent if we use the squared masses in the place of linear masses. Then we get the relation

$$4m_K^2 = 3m_\eta^2 + m_\pi^2 \quad \dots (13)$$

which is satisfied to within 6.3%. However, the reason why the use of the squared masses improves the agreement is not understood in depth. The only justification proposed for using m_i^2 instead of m_i ($i = \pi, K, \eta$) was that in the relativistic field theories

of mesons (e.g. in the Klein-Gordon equation), the meson mass always enters as m^2 .

Now we confront our modified relation (11) with the experimental data and show that there is a marked improvement in the agreement. Using the accepted numerical values

$$F_K/F_\pi = 1.25 \text{ and } F_\pi = 0.95 m_\pi \quad \dots (14)$$

in the first two relations of Eq. (10), we get

$$\begin{aligned} \lambda_0 &= 0.675 m_\pi \\ \lambda_8 &= -0.152 m_\pi \end{aligned} \quad \dots (15)$$

With these numerical values, the first and the third relations of Eq. (10) give

$$\frac{F_\eta}{F_\pi} = \frac{\sqrt{10}\lambda_0 - 2\lambda_8}{\sqrt{10}\lambda_0 + 2\lambda_8} = 1.33 \quad \dots (16)$$

Substituting the numerical values of the meson decay constants from Eqs (14) and (16) and the latest experimental data¹⁰ on their masses into Eq.(11), we find that our modified Gell-Mann-Okubo mass formula is satisfied to within 0.4%, which is really remarkable, since the chiral $SU(3) \otimes SU(3)$ itself is only an approximate symmetry and its violation is expected to be of the order of 10-20%.

Another satisfactory feature of our modified relation (11) is that in the limit of an exact $SU(3)$ symmetry (i.e., $F_\eta \approx F_K \approx F_\pi$), it reduces to the original Gell-Mann-Okubo mass formula (13) with squared masses. But relation (13) suffers from the serious drawback that the squared meson masses were introduced in this formula on an *ad hoc* basis, merely to improve its agreement. In contrast to this, the squared masses appear in our modified relation (11) as a logical consequence of the (8,8) model and the second-order Ward identity, which is more satisfying.

We are thankful to the authorities and staff of the Meerut University Library for their help and cooperation. One of us (TNT) is grateful to the Ministry of Education, Government of India, for the financial assistance.

References

- 1 Gell-Mann M & Ne'eman Y, *The eightfold way* (Benjamin, New York), 1964.
- 2 Gell-Mann M, Oakes R J & Renner B, *Phys Rev (USA)*, **175** (1968), 2195.
- 3 Glashow S & Weinberg S, *Phys Rev Lett (USA)*, **20** (1968) 224.
- 4 Sastry C V & Tiwari T N, *Phys Rev D (USA)*, **10** (1974) 366.
- 5 Sastry C V & Tiwari T N, *Phys Rev D (USA)*, **11** (1975) 1979.
- 6 Sastry C V & Tiwari T N, *Indian J Pure & Appl Phys*, **14** (1976) 128.
- 7 Sastry C V & Tiwari T N, *Indian J Pure & Appl Phys*, **16** (1978) 905.
- 8 Okubo S, *Prog Theor Phys (Japan)*, **27** (1962) 949.
- 9 Cicogna G, Strocchi F & Vergara-Caffarelli R, *Phys Rev D (USA)*, **6** (1972) 301.
- 10 Particle Data Group, *Phys Lett B (Netherlands)*, **111** (1982) 1.

Charmed Baryon Magnetic Moments in Broken SU (8) Model

K P TIWARI & C P SINGH*

Department of Physics, VSSD College, Kanpur 208 002

Received 13 October 1982

The magnetic moments of charmed baryons are studied in the broken SU(8) framework, including the additional symmetry-breaking effects due to quark masses. The results so obtained differ from those of the conventional quark model incorporating quark-mass breaking in magnetic moment operator only.

Magnetic moments have provided some very significant information in our search to understand the structure of the hadrons. The large moments of neutral baryons as well as anomalous magnetic moments of charged particles are clear evidence for important internal structure. The magnetic moments of baryons have been calculated in both the symmetry schemes¹⁻⁴ and in the quark models⁵⁻⁷ but now from the recent precise measurements⁸ it is clear that simple additive quark model considerations cannot explain these moments. Various attempts⁹⁻¹⁶ have been made to add symmetry-breaking contributions. De Rujula *et al.*¹³, in a mass broken quark model, assigning point-like Dirac magnetic moments to the quark which is taken to be proportional to the charge-mass ratio, and determining the quark mass ratio parameter from the baryon masses, successfully predicted $\mu(\lambda) = -0.61 \text{ nm}$. But with the same quark mass ratio parameter the predictions for $\mu(\Sigma^+)$, $\mu(\Xi^-)$ and $\mu(\Xi^0)$ are found to be much different. Identical results have also been obtained by Lipkin¹⁴ assuming that the quark mass difference is exactly equal to the baryon mass difference [$(m_s - m_u) = (M_\Lambda - M_p)$]. This implies that only the difference in quark masses does not provide the most general way to obtain symmetry-breaking contributions. Bag model¹⁷ which is supposed to be the manifestation of QCD and also includes the relativistic effects does not improve the situation much. Then it was thought to add additional symmetry breaking of the strong interactions in the wavefunctions. Fine structure corrections¹⁸, such as relativistic effects, configuration mixing, isospin violating effects and pion and kaon cloud contributions¹⁹ that one could expect in a constituent quark model, have been investigated, but 1% level of accuracy has not been achieved. Recently, Bohm *et al.*²⁰ have calculated the octet baryon magnetic moments using second order perturbation theory, taking into account the effect of spin-dependent

interaction arising from QCD, but failed to obtain an improved fit.

Some workers²¹⁻²⁵ have suggested different approaches of including the additional symmetry-breaking contributions. They have shown that the situation improves if one brings in baryon mass dependence in the computation of baryon magnetic moments essentially by bringing in dimensional consideration in the symmetry predictions. The situation appears to further improve^{24,25} when one considers the correction factor as given in terms of the square root of the masses of the baryons. This situation can be understood because the physical mass reflects symmetry-breaking effect and therefore, such a scale factor correctly represents a symmetry-breaking property. In a recent paper, Tomozawa²⁶ argued that such mass corrections may not be the right ones since symmetry-breaking effects presumably may be originating from the same source, (i.e. quark masses) and therefore, one should use the same parameters throughout. In calculating the octet baryon moments, he proposed²⁶ a symmetry-breaking mechanism which keeps ground state SU(6) wavefunctions and introduces a mass scale factor which is a symmetric function of quark masses and has the dimension of inverse mass.

The purpose of the present note is to study the magnetic moments of charmed baryons following the considerations of Tomozawa²⁶ and also to make a comparison with the estimates obtained in other formalisms^{12,25,26}. Since charmed baryons have been observed²⁷ and in the light of the possible mass spectrum some of the $\frac{1}{2}^+$ charmed baryons are expected to be stable against strong interactions, such studies may help in deciding the pattern of symmetry-breaking mechanism.

The magnetic moment operator¹³⁻¹⁶ μ is expressed as

$$\mu = \frac{eQ}{2m_u c} \sigma \quad \dots (1)$$

$$\text{where } Q = \left(\frac{2}{3} - \frac{\lambda}{3} - \frac{x}{3} + \frac{2y}{3} \right) \quad \dots (2)$$

$$\text{with } \lambda = \frac{m_u}{m_d}, x = \frac{m_u}{m_s} \text{ and } y = \frac{m_u}{m_c} \quad \dots (3)$$

and m_u , m_d , m_s and m_c are the masses of respective quarks. The magnetic moment of charmed baryons can be calculated by taking the expectation value of the operator [Eq. (1)] between spin unitary spin wavefunctions⁷ and are given in the second column of the Table 1. For the additional symmetry-breaking

Table 1—Charmed Baryon Magnetic Moments

Particle	SU(8) matrix element of Eq. (1)	Mass factor	
		A	B
Σ_c^+	$\frac{2}{9}(4-y)$	$\frac{2+\lambda^{-1}}{2+y^{-1}}$	$\frac{2+y}{2+\lambda}$
Σ_c^0	$\frac{2}{9}(2-\lambda-y)$	$\frac{2+\lambda^{-1}}{1+\lambda^{-1}+y^{-1}}$	$\frac{1+\lambda+y}{2+\lambda}$
Ξ_c^0	$-\frac{2}{9}(2\lambda+y)$	$\frac{2+\lambda^{-1}}{2\lambda^{-1}+y^{-1}}$	$\frac{2\lambda+y}{2+\lambda}$
Ξ_c^-	$\frac{2}{9}(2-x-y)$	$\frac{2+\lambda^{-1}}{1+x^{-1}+y^{-1}}$	$\frac{1+x+y}{2+\lambda}$
Ξ_c^0	$-\frac{2}{9}(\lambda+x+y)$	$\frac{2+\lambda^{-1}}{\lambda^{-1}+x^{-1}+y^{-1}}$	$\frac{\lambda+x+y}{2+\lambda}$
Ω_c^0	$-\frac{2}{9}(2x+y)$	$\frac{2+\lambda^{-1}}{2x^{-1}+y^{-1}}$	$\frac{2x+y}{2+\lambda}$
Ξ_{cc}^{++}	$\frac{2}{9}(4y-1)$	$\frac{2+\lambda^{-1}}{1+2y^{-1}}$	$\frac{1+2y}{2+\lambda}$
Ξ_{cc}^+	$\frac{1}{9}(8y+\lambda)$	$\frac{2+\lambda^{-1}}{\lambda^{-1}+2y^{-1}}$	$\frac{\lambda+2y}{2+\lambda}$
Ω_{cc}^+	$\frac{1}{9}(8y+x)$	$\frac{2+\lambda^{-1}}{x^{-1}+2y^{-1}}$	$\frac{x+2y}{2+\lambda}$
Λ_c^+	$\frac{2}{3}y$	$\frac{2+\lambda^{-1}}{1+\lambda^{-1}+y^{-1}}$	$\frac{1+\lambda+y}{2+\lambda}$
Ξ_c^+	$\frac{2}{3}y$	$\frac{2+\lambda^{-1}}{1+x^{-1}+y^{-1}}$	$\frac{1+x+y}{2+\lambda}$
Ξ_c^0	$\frac{2}{3}y$	$\frac{2+\lambda^{-1}}{\lambda^{-1}+x^{-1}+y^{-1}}$	$\frac{\lambda+x+y}{2+\lambda}$
$\langle \Lambda_c^+ \Sigma_c^+ \rangle$	$\frac{1}{3\sqrt{3}}(\lambda+2)$	$\frac{2+\lambda^{-1}}{1+\lambda^{-1}+y^{-1}}$	$\frac{1+\lambda+y}{2+\lambda}$
$\langle \Xi_c^+ \Xi_c^+ \rangle$	$\frac{1}{3\sqrt{3}}(x+2)$	$\frac{2+\lambda^{-1}}{1+x^{-1}+y^{-1}}$	$\frac{1+x+y}{2+\lambda}$
$\langle \Xi_c^0 \Xi_c^0 \rangle$	$\frac{1}{3\sqrt{3}}(1-x)$	$\frac{2+\lambda^{-1}}{\lambda^{-1}+x^{-1}+y^{-1}}$	$\frac{\lambda+x+y}{2+\lambda}$

term coming from strong interactions, we employ two mass scale factors

$$(A) \frac{1}{m_1+m_2+m_3} \quad \dots (4)$$

$$(B) \frac{1}{m_1} + \frac{1}{m_2} + \frac{1}{m_3} \quad \dots (5)$$

where m_1, m_2, m_3 are the masses of the quarks which constitute the baryons. The mass scale factors [Eqs (4) and (5)] entering in the expression for the magnetic moments of various baryons can easily be calculated and are given in third and fourth columns of Table 1.

The parameters λ and x can be determined by taking $\mu(p) = 2.79$ nm, $\mu(n) = -1.91$ nm and $\mu(\Lambda) = -0.614$ nm as inputs and these come out to be $\lambda = 1.03$ and $x = 0.726$ (Ref. 26). For the parameter y , as there is no charmed baryon whose magnetic moment is known, we following Rujula *et al.*¹³ determine its values using the known baryon masses in the expression

$$y = \frac{2(M_{\Sigma_c^*} - M_{\Sigma})}{2M_{\Sigma_c^*} + M_{\Sigma_c} - 3M_{\Lambda_c}} \simeq 0.23 \quad \dots (6)$$

Once the value of the parameters λ , x and y are known, the magnetic moments of the charmed baryons can be calculated and they are given in Table 2.

From our analysis, we noticed that our results differ from those of conventional quark models¹³⁻¹⁶ incorporating quark mass breaking in magnetic moment operator only. In Table 2 we also made a comparison of our results with some of the other formalisms which use a different mass scale^{24,25} or SU(4) symmetry-breaking terms¹² and found that the

Table 2—Comparison of Present Results on Charmed Baryon Magnetic Moments (in nuclear magnetons) with Other Formalisms

Particle	Quark model (Ref. 13) (Without mass scale)	Present analysis (Mass scale in terms of quark masses)	Formalism of	Formalism of	Formalism of
			Teese & Settles (Ref. 24) (Mass scale by $1/\sqrt{m_B}$)	Singh (Ref. 25) (Mass scale by $1/\sqrt{m_B}$)	Verma (Ref. 12) [(SU4) breaking]
Σ_c^{++}	2.36	1.07	1.44	1.45	1.50
Σ_c^+	0.46	0.22	0.29	0.30	0.68
Σ_c^0	-1.43	-0.67	-1.07	-0.86	-0.85
Ξ_c^+	0.73	0.28	0.42	0.37	0.40
Ξ_c^0	-1.16	-0.54	-0.81	-0.76	-0.72
Ω_c^0	-0.89	-0.43	-0.58	-0.65	-1.16
Ξ_{cc}^{++}	-0.12	-0.02	-0.23	-0.00	-0.59
Ξ_{cc}^+	0.82	0.27	0.44	0.47	-0.48
Ω_{cc}^+	0.69	0.23	0.31	0.42	0.71
Λ_c^+	0.37	0.20	0.32	0.30	0.21
Ξ_c^+	0.37	0.19	0.27	0.29	0.69
Ξ_c^0	0.37	0.20	0.28	0.29	0.36
$\langle \Lambda_c^+ \Sigma_c^+ \rangle$	1.61	0.76	1.21	0.99	0.95
$\langle \Xi_c^+ \Xi_c^+ \rangle$	1.41	0.65	0.94	0.90	0.94
$\langle \Xi_c^0 \Xi_c^0 \rangle$	0.20	0.06	0.09	0.07	0.01

results are comparable. However, it will presumably take some time before the magnetic moments of charmed hadrons can be measured. Nevertheless, we present our results now because, there may be other calculations more accessible to experimental tests in which magnetic moments are needed. Also, the decay rates of some of the charmed baryons will depend upon the transition moments which may be of immediate interest.

In the following, the relations among different ratios of the magnetic moments of the baryons of the same multiplet are discussed. However, if we neglect the isospin breaking, i.e. take $\lambda=1$, the following three relations are obtained:

$$\gamma_{\Sigma} = \frac{-5 + 6\gamma_{\Xi}}{11 - 10\gamma_{\Xi}} \quad \dots (7)$$

$$\gamma_{\Sigma_c} = \frac{-5 + 3\gamma_{\Xi_{cc}}}{11 - 5\gamma_{\Xi_{cc}}} \quad \dots (8)$$

$$\gamma_{\Xi_c} = \frac{2\gamma_{\Xi_{cc}} - \gamma_{\Xi}\gamma_{\Xi_{cc}} + \gamma_{\Xi} - 3}{2\gamma_{\Xi_{cc}} - 3\gamma_{\Xi}\gamma_{\Xi_{cc}} + 7\gamma_{\Xi} - 5} \quad \dots (9)$$

$$\text{where } \gamma_{\Sigma} = \frac{\mu(\Sigma^-)}{\mu(\Sigma^+)}, \gamma_{\Xi} = \frac{\mu(\Xi^-)}{\mu(\Xi^0)} \quad \dots (10)$$

$$\text{and } \gamma_{\Sigma_c} = \frac{\mu(\Sigma_c^0)}{\mu(\Sigma_c^{++})}, \gamma_{\Xi_c} = \frac{\mu(\Xi_c^0)}{\mu(\Xi_c^+)} \quad \left. \begin{array}{l} \gamma_{\Xi_{cc}} = \frac{\mu(\Xi_{cc}^+)}{\mu(\Xi_{cc}^{++})} \end{array} \right\} \quad \dots (11)$$

For uncharmed particles, surprisingly both experimental and theoretical values satisfy an approximate equation

$$\gamma_{\Sigma} \approx -\gamma_{\Xi} \quad \dots (12)$$

But we could not arrive at any such conclusion for charmed baryon magnetic moment because of the non-availability of experimental information.

The authors are thankful to Prof. B S Bhargava for providing the necessary facilities in the Department.

References

- 1 Coleman S & Glashow S L, *Phys Rev Lett (USA)*, **6** (1961) 423.
- 2 Beg M A, Lee B W & Pais A, *Phys Rev Lett (USA)*, **13** (1964) 514.
- 3 Choudhary A L & Joshi V, *Phys Rev D (USA)*, **13** (1976) 3115.
- 4 Verma R C & Khanna M P, *Pramana (India)*, **8** (1977) 462.
- 5 Rubinstein H R, Scheck F & Socolow R H, *Phys Rev (USA)*, **154** (1967) 1608.
- 6 Franklin J, *Phys Rev (USA)*, **172** (1968) 1867; **182** (1969) 1607.
- 7 Singh L P, *Phys Rev D (USA)*, **16** (1977) 158.
- 8 Particle data group, *Rev Mod Phys (USA)*, **52** (1980) 1.
- 9 Kamal A N, *Phys Rev D (USA)*, **18** (1978) 3512.
- 10 Singh C P, Verma R C & Khanna M P, *Pramana (India)*, **13** (1979) 261.
- 11 Pandit P N, Singh C P & Khanna M P, *Acta Phys Austr (Austria)*, **53** (1981) 211.
- 12 Verma R C, *Phys Rev D (USA)*, **22** (1980) 1156.
- 13 Rujula A De, Georgi H & Glashow S L, *Phys Rev D (USA)*, **12** (1975) 147.
- 14 Lipkin H J, *Phys Rev Lett (USA)*, **41** (1978) 1629.
- 15 Franklin J, *Phys Rev D (USA)*, **20** (1979) 1742; *Phys Rev Lett (USA)*, **45** (1980) 1607.
- 16 Lichtenberg D B, *Phys Rev D (USA)*, **15** (1977) 345; *Z Phys C (Germany)*, **7** (1981) 143.
- 17 Allen E, *Phys Lett B (Netherlands)*, **57** (1975) 263; Hackman R H et al., *Phys Rev D (USA)*, **18** (1978) 2537.
- 18 Isgur N & Karl G, *Phys Rev D (USA)*, **21** (1980) 3175.
- 19 Theberge S & Thomas A W, *Phys Rev D (USA)*, **25** (1982) 284; Goziliz P et al., *Kaon cloud and baryon magnetic moments*, D Ph T/19, 1982.
- 20 Bohm M, Hwerta R & Zepeda A, *Spin-dependent quark-quark interaction and baryon magnetic moments*, Wurzburg University preprint 1980.
- 21 Bohm A, *Phys Rev D (USA)*, **18** (1978) 2547.
- 22 Tomozawa Y, *Phys Rev D (USA)*, **19** (1979) 1626.
- 23 Das T & Misra S P, *Phys Lett B (Netherlands)*, **96** (1980) 115.
- 24 Teese R B & Settles R, *Phys Lett B (Netherlands)*, **87** (1979) 111.
- 25 Singh C P, *Phys Rev D (USA)*, **23** (1981) 2085.
- 26 Tomozawa Y, *Phys Rev D (USA)*, **25** (1982) 795.
- 27 Cazzoli R G et al., *Phys Rev Lett (USA)*, **34** (1975) 1125, Knapp B. et al., *Phys Rev Lett (USA)*, **37** (1976) 882.

EPR of Cu²⁺ in MgSeO₄.6H₂O Single Crystals

V K JAIN

Department of Physics, M D University, Rohtak 124001

Received 27 November 1982; revised received 27 January 1983

The EPR spectrum of Cu²⁺ ($S = 1/2$, $I = 3/2$) in MgSeO₄.6H₂O consists of two overlapping angle-dependent four-line hyperfine patterns arising from two differently but magnetically equivalent Cu²⁺ complexes located at a specific site. The angular variation of the spectrum indicates that Cu²⁺ substitutes for Mg²⁺ at Y-ion sites only.

In the study of complex crystal structures in which the isomorphic substitution of an impurity ion can occur at a number of different lattice sites, the general methods of crystal chemistry are often inadequate when it comes to predicting which crystallographic position must be occupied by the ion. Many questions pertaining to the introduction and the state of impurity ions can be elucidated from the electron paramagnetic resonance (EPR) spectra. The X-ray analysis of MgSeO₄.6H₂O single crystals has shown that the crystal structure consists of two crystallographically different Mg²⁺ ion sites¹. Subramanian *et al.*² and Jain and Venkateswarlu³ have studied respectively the EPR of Co²⁺ and Mn²⁺ in MgSeO₄.6H₂O single crystals and shown that impurity ions occupy both the sites. The present study deals with the results obtained in the EPR of Cu²⁺ incorporated into MgSeO₄.6H₂O single crystals.

Magnesium selenate hexahydrate (MgSeO₄.6H₂O) crystallizes in monoclinic symmetry with space group $C(2/c)-C_{3h}^6$ ¹. The lattice constants are $a = 10.36 \text{ \AA}$, $b = 7.38 \text{ \AA}$, $c = 25.1 \text{ \AA}$ and $\beta = 98.1^\circ$. The unit cell contains eight formula units. Out of eight Mg²⁺ present in the unit cell, four have the same crystallographic surrounding having point symmetry 2 (X-ions). The other four have point symmetry 1 (Y-ions). The Y-ions form two pairs which are equivalent through reflection in the ac plane. The Mg²⁺ at both the sites are surrounded by a distorted octahedron of water molecules.

Crystals of MgSeO₄.6H₂O doped with Cu²⁺ were grown at room temperature ($\sim 298 \text{ K}$) by slow evaporation of saturated aqueous solution. The Cu²⁺ was introduced into the host lattice by adding a small amount (1% by weight) of cupric sulphate. EPR experiments were performed on a JEOL FE-3X homodyne X-band spectrometer equipped with TE₀₁₁-cylindrical cavity and 100 kHz field

modulation. As a reference for magnetic field strength, the resonance line of DPPH with $g = 2.0036$ was used. The crystals were mounted on quartz rods. The angular variation studies were done using JES-UCR-2X sample angular rotating device.

The EPR spectrum of Cu²⁺ ($S = 1/2$, $I = 3/2$) in MgSeO₄.6H₂O consists of two overlapping angle-dependent four-line hyperfine patterns (Fig. 1) arising from two differently but magnetically equivalent Cu²⁺ complexes located at a specific site. When the magnetic field is along the b axis or in the ac' plane (c' is at 90° to a axis in the ac plane) only a single set of four lines was observed indicating that none of the principal axes lie in ac' plane or along the b axis. The angular variation of the spectra in ab , bc' and $c'a$ plane shows orthorhombic symmetry. The linewidth of the spectrum along the z axis is $\sim 2.0 \text{ mT}$. The spectra at 298 K have been analysed using the spin-Hamiltonian

$$\mathcal{H} = \mu_B S \cdot g \cdot B + S \cdot A \cdot I$$

where the symbols have their usual meaning. The values of the spin-Hamiltonian parameters are: $A_z = 105.8 \pm 1.0$, $A_y = 47.4 \pm 1.0$, $A_x = 16.6 \pm 2.0$, $g_z = 2.400 \pm 0.001$, $g_y = 2.109 \pm 0.002$, $g_x = 2.080 \pm 0.002$, $\theta = 80^\circ \pm 1^\circ$, $\phi = -20^\circ \pm 2^\circ$ where the A values are in units of 10^{-4} cm^{-1} , θ is the angle between the z axis and the b axis and ϕ is the angle between the a axis and the projection of z on the ac' plane. The values of the components of the g -factor indicate that Cu²⁺ in the lattice is surrounded by six water molecules⁴.

If Cu²⁺ enters substitutionally in MgSeO₄.6H₂O, the sites available to it are those of Mg²⁺ and Se⁶⁺. As the valence states of Cu²⁺ and Mg²⁺ do not differ, Cu²⁺ would prefer to occupy Mg²⁺ sites. The crystal structure of MgSeO₄.6H₂O requires that Cu²⁺ oriented arbitrarily in both X- and Y-ions site have four symmetry-related equivalent orientations given by the space group symmetry operations. For X-ions, all are magnetically equivalent for all orientations of the crystal. All Y-ions are chemically equivalent but magnetically equivalent in pairs, showing two sets of quartets for any arbitrary orientation. The angular variation of the spectrum indicates that Cu²⁺

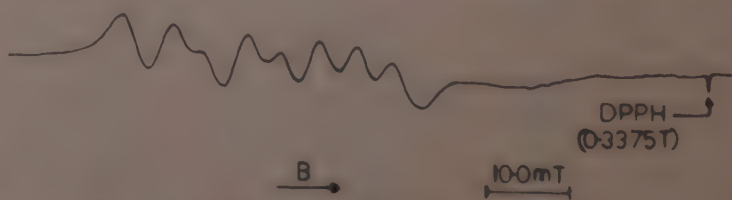


Fig. 1—EPR spectrum of Cu²⁺ in MgSeO₄.6H₂O single crystals at 298 K and at X-band frequencies ($v \sim 9.45 \text{ GHz}$) for B at an angle of 15° to the a axis in the ab plane

substitutes for Mg^{2+} at Y-ion sites only. Because if it only substitutes for X-ion sites, the spectrum should consist of four lines for all orientations of the crystal as required by the space group symmetry operations. Nevertheless, if Cu^{2+} substitutes for both X- and Y-ions sites, one would have observed two sets of four lines for magnetic field in the ac' plane or along the b axis. Further, a comparison of the value of θ and φ obtained experimentally with those calculated from the data of Zalkin *et al.*¹ for different Mg—H₂O bonds indicates that z axis is nearly along the longest Mg(Y-ion)—H₂O bond, i.e. Mg—H₂O(7) ($\theta = 79.0^\circ$, $\varphi = -14.36^\circ$). Thus Cu^{2+} substitutes for Y-sites of Mg^{2+} to form $[Cu(H_2O)_6]^{2+}$ complexes with z axis nearly along the longest Mg—H₂O bond direction. On the other hand, EPR of Co^{2+} and Mn^{2+} in $MgSeO_4 \cdot 6H_2O$ indicates that impurity ions enter the lattice substitutionally at both X- and Y-ions sites^{2,3}.

The $[Cu(H_2O)_6]^{2+}$ ion in the $MgSeO_4 \cdot 6H_2O$ belongs to the point group \bar{I} (C_i), so that the metal part of the ground state wavefunction in the absence of spin-orbit coupling consists of an admixture of all five d orbitals. In fact, the ligand field is composed of a dominant D_{4h} component with an additional perturbation due to the inequivalent bond length along the x and y axes which lowers the point group to D_{2h} and a further lowering of the symmetry to C_i because of the non-planarity of the atoms in each Cu—H₂O unit. In the D_{4h} point group, the metal part of the ground state is $d_{x^2-y^2}$ and lowering of the symmetry to D_{2h} causes this to become contaminated with $d_{3z^2-r^2}$. The further lowering of the symmetry to C_i is accompanied by a change in the nature of the interaction of the water molecules with the metal d_{xy} , d_{xz} , and d_{yz} orbitals and consequent participation of these in the ground state. However, participation of d_{xy} , d_{yz} , d_{xz} orbitals have little effect on the g values. Thus neglecting the participation of d_{xy} , d_{xz} and d_{yz} in the ground state wavefunction, the metal part of which can be written⁵

$$\psi = a|d_{x^2-y^2}\rangle - b|d_{3z^2-r^2}\rangle$$

where $a^2 + b^2 = 1$. The equations for the g shifts are those for a complex of D_{2h} symmetry^{5,6}

$$\Delta g_x = -2(\lambda/E_{yz})k_1^2(a - \sqrt{3}b)^2$$

$$\Delta g_y = -2(\lambda/E_{xz})k_2^2(a + \sqrt{3}b)^2$$

$$\Delta g_z = -8(\lambda/E_{xy})k_3^2a^2$$

where E_i represents the energy of the excited state in which the unpaired electron occupies the orbital denoted by the subscript; λ is the spin-orbit coupling constant (-828 cm^{-1} for Cu^{2+}); and k_1 , k_2 , k_3 are orbital reduction parameters⁷. The net effect of the admixture of the $d_{3z^2-r^2}$ into the ground state is to produce a new wavefunction of the form $\psi |cx^2 + ey^2 + fz^2\rangle$ with unequal lobes along x , y , and z where $c = b + \sqrt{3}a$, $e = b - \sqrt{3}a$, $f = -2b$.⁶

As the electronic spectrum of Cu^{2+} in $MgSeO_4 \cdot 6H_2O$ is unknown the value of E_{xz} , E_{yz} and E_{xy} have been taken as those for $[Cu(H_2O)_6]^{2+}$ complexes in other hydrated crystals⁸, i.e. $E_{xz} = E_{yz} = \sim 12,500\text{ cm}^{-1}$, and $E_{xy} = \sim 10,000\text{ cm}^{-1}$. The parameters c , e and f were calculated with the restriction $k_1 = k_2 = k_\perp$ and $k_3 = k_\parallel$. The parameters c , e and f calculated from the molecular g values are $c = 1.776$, $e = -1.684$, and $f = -0.092$, $k_\parallel^2 = 0.602$, $k_\perp^2 = 0.691$.

This work was supported by CSIR, New Delhi under project 3(502)/81/EMR-II. The author wishes to thank Prof. T S Jaseja for his interest and encouragement.

References

- Zalkin A, Ruben H & Templeton D H, *Acta Crystallogr (Denmark)*, **15** (1962) 1219.
- Subramanian S, Rahman Z & Witters J, *J Chem Phys (USA)*, **49** (1968) 473.
- Jain V K & Venkateswarlu P, *Phys Stat Solidi (Germany)*, (b) **88** (1978) K173.
- Abragam A & Bleaney B, *Electron Paramagnetic Resonance of Transition Ions* (Clarendon Press, Oxford) 1970, 456.
- McGarvey B, *Electron spin resonance of transition metal complexes in Transition Metal Chemistry*, ed. R L Carlin (Marcel-Dekker, New York) 1966, Vol. 3, 160.
- Hitchman M A, *J Chem Soc (GB)*, **A** (1970) 4.
- Gerloch M & Miller J R, *Prog Inorg Chem (USA)*, **10** (1968) 1.
- Hitchman M A & Waite T D, *Inorg Chem (USA)*, **15** (1976) 2150.

Twyman Green Interferometer with Curved Mirrors

M V R K MURTY† & R P SHUKLA*

Spectroscopy Division, Bhabha Atomic
Research Centre, Tromay,
Bombay 400 085

Received 25 August 1982; revised received 11 October 1982

Twyman Green interferometer with curved mirrors is described. It is found that the end mirrors in the Twyman Green interferometer need not be necessarily plane but must be identical in figure.

Twyman Green interferometer¹ is used for testing the optical homogeneity of prisms, lenses and parallel plates in optical testing laboratories. It is essentially a modification of the Michelson interferometer where the extended source of light is replaced by a point source at the focus of a well corrected lens and consequently a collimated beam of light is used in the interferometer. The fringes obtained are therefore straight and equidistant for the case when the real mirror and the virtual mirror are making a small wedge angle. Fringe-free field is obtained for the case when the real and virtual mirrors are parallel to each other. When one of the mirrors in it is replaced by a slightly curved (convex or concave) spherical mirror, a set of circular fringes is obtained in the field of view due to the interference of the plane and curved wavefronts. The number of fringes depends on the amount of curvature present in the mirror. This type of arrangement is not suitable for testing the parallel plates and prisms. It is interesting to see the nature of the fringe pattern when both the plane mirrors are replaced by slightly curved (convex or concave) spherical mirrors which are identical in shape. Such type of arrangement is shown schematically in Fig. 1. The mirrors are chosen to be about 2.5 wavelengths convex and placed at equal distances from the beam dividing surface. The reflected wavefronts from both the mirrors are identical in nature. When the interfering beams are parallel to each other, a uniform illumination is obtained over the aperture. In order to obtain straight fringes a slight tilt between the beams can be introduced. Fig. 2 shows the photograph of nearly straight fringes obtained with the arrangement shown in Fig. 1. The result shows that it is not necessary

to make the mirrors perfectly plane but efforts must be made to make both the figures identical.

The maximum amount of curvature that can be tolerated on the mirrors can be derived from Figs.(3a) and (3b). Fig. 3a shows the situation when the two mirrors are not located at equal distances from the beam divider. This happens while testing the ruby rods, thick parallel plates, etc. The image of the mirror M_2 in the beam divider is separated by an amount t from the mirror M_1 . The reflected wavefronts have their foci at F_1 and F_2 . The interference takes place between two wavefronts, whose foci are displaced longitudinally and therefore the illumination will not be uniform over the whole aperture. The variation of optical path difference (δ) over the aperture is given by

$$\delta \approx \frac{y^2}{R} - \frac{Y^2}{(R+2t)} = \frac{2tY^2}{R^2} - \frac{Y^2}{R}$$

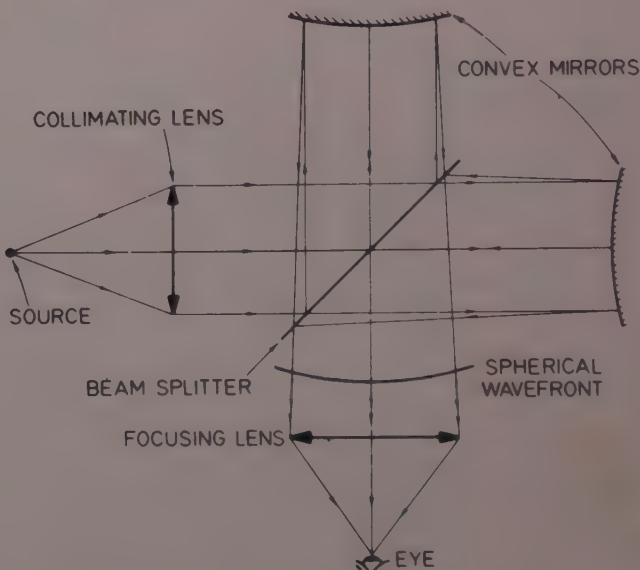


Fig. 1—Schematic diagram of Twyman Green interferometer with curved mirrors; the mirrors in the conventional Twyman Green interferometer have been replaced by slightly convex mirrors



Fig. 2—Photograph of the nearly straight fringes obtained with the arrangement of Fig. 1

*Present address: Centro De Investigaciones En Óptica, A.C.
Apartado Postal 948, Passage Del Consuelo, 120-201, Leon, GTO.
Mexico

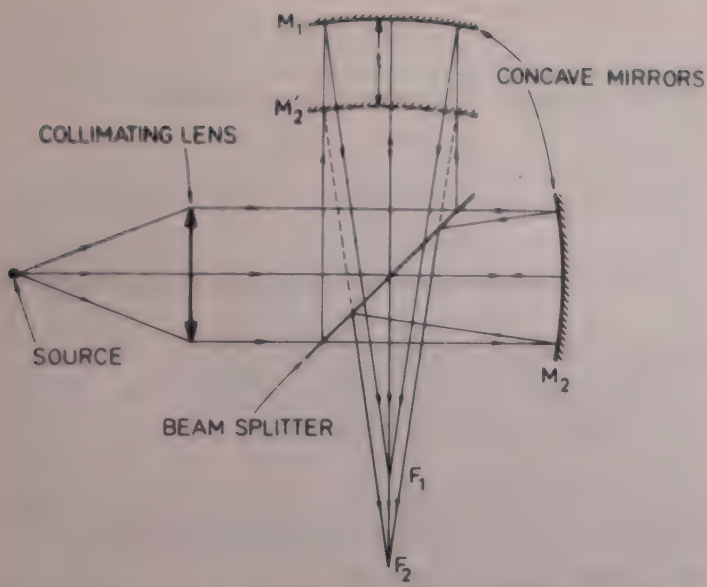


Fig. 3a—Schematic diagram of Twyman Green interferometer with curved mirrors; the mirrors are placed at unequal distances from the beam splitter

where R is the radius of curvature of the mirrors and Y the distance of the point on the mirror measured from the optical axis.

For $\delta \leq \frac{\lambda}{20}$, $t = 500$ mm, $Y = 50$ mm, we get $R \geq 281.1$ m taking $\lambda = 6328$ Å.

The sag of the mirror is about 7λ .

Hence the mirrors can tolerate the curvature corresponding to a sag of 7λ concave or convex for maximum variation of δ by $\lambda/20$ over 100 mm aperture.

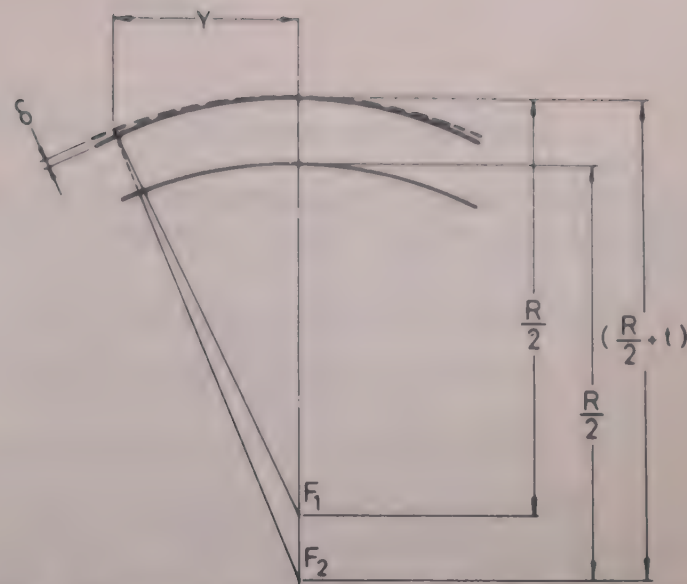


Fig. 3b—Schematic diagram showing the paths of the reflected wavefronts from the two mirrors. The continuous line curves show the actual wavefronts of radii of curvature $R/2$ with foci F_1 and F_2 separated by the distance t . The broken line curve of radius of curvature $[(R/2)+t]$ has been drawn with F_2 as its centre to find out the variation of δ with aperture and t

The authors are indebted to Dr S L N G Krishnamachari, Head, Spectroscopy Division, for his suggestions and encouragement throughout the course of this work. We also thank Mr S Bhattacharya for the drawings and Mr R Srinivasan for typing the manuscript.

References

- Candler C. *Modern interferometers* (Hilger & Watts, London), 1951, Chaps. 6&7.

Papers Accepted for Publication

The following papers have been accepted for publication in the journal and will be published in due course with necessary editorial changes.

Optical Absorption & Thermoluminescence of Gd- or Sm-Doped CaF_2 Single Crystals Irradiated with X-rays

R K Chaudhary, A V Krishna Rao & K V Rao

Homo & Lumo-Energy Values for Bases of Nucleic Acids

K B Lal, V K Agrawal, A K Srivastava & B Krishna

Optical Absorption of Some Irradiated Sodium-Silicate Glasses Containing Chromium

N A Ghoneim, F A Moustaffa, H A El Batal, A H Zahran & F M Ezz El Din

Ultrasonic Studies of Some Electrolytic Solutions

B Manikam & A V Narasimham

On the Random Electrodynamics of Nonlinear Systems: Part II—The Hydrogen Atom

S Sachidanandam & I V V Raghavacharyulu

Unified Kinematics in Eight-Dimensions

H C Chandola & B S Rajput

Effect of Bi Doping on the Properties of PEC Cells Formed with CdS:Bi Films

A U Warad & S H Pawar

Substituted Benzenes: Part I—Normal Coordinate Analysis of Mono Fluoronitrobenzenes

P Muralidhar Rao & G Ramana Rao

Substituted Benzenes: Part III—Normal Coordinate Analysis of Mono Bromonitrobenzenes

P Muralidhar Rao & G Ramana Rao

Substituted Benzenes: Part VII—Normal Coordinate Analysis of Out-of-plane Vibrations of Mono Chloronitrobenzenes

P Muralidhar Rao & G Ramana Rao

Study of ${}^{16}\text{O}$ -Ion Tracks in Makrofol Polycarbonate Plastic Track Detector

S M Farid & A P Sharma

Effect of Melt Composition on Growth & Properties of LiNbO_3 Crystals

K N Srivastava, J R Gangarh, M V Rishi & B Singh

Thermal Properties of the Binary Glass System $\text{V}_2\text{O}_5-\text{GeO}_2$

A A El-Sharkawy, A M Sanad & M S Zaghloul

Dielectric Studies of Some Mixed Oxide Thin Films

G Narayana, J Siva Kumar, M Chandra Shekar, U V Subha Rao & V Hari Babu

Electronic & Laser Raman Spectra & Thermodynamic Functions of Some Di-Substituted Pyridines

R K Goel & S K Sharma

Vibrational Assignment of Acetanilide, *p*-Bromoacetanilide & *p*-Aminoacetanilide

Syed Tariq, Naushad Ali & P K Verma

Study of Tachyon-Bradyon Electromagnetic Interactions

O P S Negi & B S Rajput

On the Mechanism of High Field Electroluminescence of ZnS:Pr, Cl & ZnS:Cu, Pr, Cl Phosphors

R C Maheshwari & R K Tripathi

Small Angle X-ray Scattering from Tubular Structures

P S Mukherjee, G D Nigam & S Bhattacherjee

Rotational Barrier Height & Off-center of Mass Displacement of Hydroxyl Ion in Alkali Halide Crystal Matrices

Lallan Jha & Hare Krishna Jha

Perturbed Solutions in Two-Channel Dirac Equations

Sheilly Mehta & L K Sharma

Meson Spectroscopy for the Superposition of Linear-cum-Logarithmic Potential with a Modified Coulomb Potential

Anuradha Bhargava & L K Sharma

Magnetic Interactions of $J=0$ Hadrons

R Sagar & Ramesh C Verma

Lattice Properties of Some Ionic Crystals

D D Shukla, Y S Sainger, R M Misra, Ram Singh, B P Misra & M N Sharma

INSTRUCTIONS TO AUTHORS

SCOPE

The journal welcomes, for publication, full papers and short notes, reporting significant new results of research, in all areas of physics except space physics. The applied fields covered are electronics, electrical engineering, instrumentation and applied mathematics. However, papers in applied mathematics with emphasis on only derivation and proofs and having no direct physical significance, will not be considered. Review articles are not published normally.

SUBMISSION OF MANUSCRIPT

Manuscripts for consideration should be submitted, *in duplicate*, to Editor, Indian Journal of Pure & Applied Physics, Publications & Information Directorate, Hillside Road, New Delhi 110 012. They should neither have been already published nor be under consideration elsewhere.

Manuscripts should be in English and typewritten on only one side of good quality paper, in double space, with adequate margin on all four sides. One original and one carbon or photo-copy, each complete in all respects including abstract, illustrations, appendixes, etc. are to be submitted.

PREPARATION OF MANUSCRIPT

Authors may consult recent issues of the Journal to familiarize themselves with the general style and practices adopted in regard to the various elements of a paper.

General

Manuscript should be presented in as concise a form as possible. Good attention should be given to spelling and grammar. In giving names of chemical compounds and structures, abbreviations of units of measurements, symbols and notations, the style and practices recommended by the IUPAP and IUPAC, should be followed.

Frequently repeating combinations of words, e.g. electric field gradient (EFG), junction field effect transistor (JFET), stimulated Raman emission (SRE), should be abbreviated subsequently, indicating the abbreviated form in parenthesis, as shown, at the place of their first occurrence.

Pages should be numbered consecutively and arranged in the following order: Title, authors' names with their institutional affiliations and abstract, along with relevant footnotes whenever necessary (on a separate sheet); introduction; experimental details/theory/method/analysis; results; discussion; conclusion(s); acknowledgement; references and appendixes. Tables, captions for figures (with legends) and appendixes should be typed on *separate sheets* and attached at the end of the manuscript.

Title

The title should be neither too brief/general nor unnecessarily long. It should reflect the content of the paper so as to derive the maximum advantage in indexing. If a paper forms part of a general series, a specific subtitle, indicating the particular aspect of the work covered in the paper, should be provided.

A short running title for the paper, the broad subject heading under which it should be classified in the contents page (authors may consult recent numbers of the journal for this purpose), and the author (indicated by an asterisk on the relevant author's name) and address for correspondence, should also be provided on the title page.

Abstract

The abstract, usually not exceeding 200 words, should indicate the scope and significant content of the paper,

highlighting the principal findings and conclusions. It should be in such a form that abstracting periodicals can use it without modification.

Introduction

Long and elaborate introduction should be avoided. It should be brief and state the exact scope of the study in relation to the present status of knowledge in the field. Literature review should be limited strictly to what is necessary to indicate the essential background and the justification for undertaking the study.

Materials, methods, apparatus, etc.

The sources of materials and their purity, methods of preparation, procedure for measurements and their accuracies, etc. should be clearly stated to enable any other worker to repeat the work if necessary. New methods, techniques, theories, etc. should be described in adequate detail; but if they are well known, a mere literature reference to them will do; differences from standard ones, improvements or innovations should, however, be clearly mentioned.

Results

Only such primary data as are essential for understanding the discussion and main conclusions emerging from the study should be included. All secondary data as are of interest to a specific category of readership *should not be included* in the paper. Such data should be retained by the authors for supply, on request, to any interested research worker. A footnote to this effect may be inserted at the relevant place in the paper.

The results must be presented in a coherent sequence in a unified logical structure, avoiding repetition or confusion. Limitations of the results should be clearly stated.

The same data should not be presented in both tabular and graphic forms. Only such tables and figures as are essential should be included. Simple linear plots that can easily be discussed in the text, should not be included. Infrared, ultraviolet, NMR and other spectra, DTA curves, etc. should be included only if they pertain to new compounds and/or are essential to the discussion; otherwise only significant numerical data should be given in the text or in a table.

Discussion

Long rambling discussion should be avoided. The discussion should deal with the interpretation of results without repeating information already presented under results. It should relate new findings to the known and include logical deductions. A separate section on 'conclusions' can be given only when they are well established and of outstanding significance. Mere observation of qualitative trends of results should be distinguished from firm conclusions. Also, limitations, if any, to the conclusions should be clearly pointed out.

Mathematical portions

Special attention should be given to the mathematical portions of the paper. Equations must be well separated from the text and written clearly with good separation between the successive lines. The usual norms of breaking long mathematical expressions should be adhered to. Equations should be numbered consecutively in Arabic numerals with the number in parenthesis near the right hand margin. Superscripts and subscripts should be clearly indicated in pencil by V and A sign respectively. Capital and small letters,

particularly of the same letter when both occur, as well as letters or symbols likely to be confused one for the other, should be clearly distinguished. Special characters (e.g. Greek, script, vector, tensor, etc.) required must be indicated by marginal notes. Letters and symbols which should appear in bold face must be clearly indicated. To simplify typesetting: (i) long and complicated mathematical expressions which are frequently repeated should be replaced with single letter/symbol, without clashing with the others used in the paper; (ii) the "exp" form of complex exponential functions should be used; and (iii) to simplify fractions, the solidus (/) is to be used and fractional exponents are to be used instead of root signs, e.g.

write $\exp\{-i\omega_0(t_1 - t_2)/2\}$ and not $e^{-i\omega_0(t_1 - t_2)/2}$

write $(4\omega_{pl} K_{3\lambda}^2/\tilde{\omega} K_D^2)^{1/2}$ and not $\sqrt{\frac{4\omega_{pl} K_{3\lambda}^2}{\tilde{\omega} K_D^2}}$

Tables

Tables should be numbered consecutively in Arabic numerals and should bear brief titles. Column headings should be brief. Units of measurement should be abbreviated and placed below the headings. Nil results should be indicated and distinguished clearly from absence of data. Inclusion of structural formulae inside the tables should be avoided as far as possible. Tables should be referred to in the text by numbers and not by terms like 'above', 'below', 'preceding' or 'following'. Results should not be presented to a greater accuracy than that of the method employed.

Illustrations

The number of illustrations should be kept to the minimum. Wherever possible, e.g. a number of individual analogous figures referring to different variables, substances, molecules, etc. may be combined into one composite figure. All illustrations should be numbered consecutively in Arabic numerals. Captions and legends to the figures should be self-explanatory. Line drawings should be made with Indian ink on white drawing paper/cellophane sheet/tracing cloth, and drawn to approximately twice the printed size.

The lettering should be uniform, preferably in stencil, so as to be not less than 1.5 mm after reduction widthwise to full page size (165 mm) or column size (80 mm). The size of geometrical shapes (used to distinguish different graphs), dots, lines, etc. should be sufficiently large to permit the necessary reduction without loss of detail. In the case of photographs, prints must be on glossy paper and contrasty. If an illustration is taken from another publication, reference to the source should be given and prior permission secured. Illustrations should be referred to in the text by numbers and not by terms like 'above', 'following' etc.

Acknowledgement

Acknowledgements should not be exuberant and must be made only to real assistance rendered in connection with the work reported in the paper.

References

References cited should be limited to the absolute minimum (particularly in the case of short notes) based on their essential relevance. In the text, references to literature should be numbered consecutively, in the order of their first occurrence, and should be indicated by superscript Arabic numbers at the relevant places; as far as possible the placement of references on numerals or other symbols should be avoided; in such cases the reference may be given in parenthesis in running text, e.g. "this yielded for n a value of 2.3 (Ref. 5)". Full bibliographic details for all the references mentioned in the text should be listed in serial order at the end of the paper.

In citing references to research papers, names and initials of authors should be followed, in order, by the title of the periodical in the abbreviated form (underlined), the volume number (two lines underneath), the year within circular brackets and the page number [e.g. Chandra B P & Shrivastava KK, *J Phys & Chem Solids (GB)*, 39 (1978) 939]. For names of periodicals, the abbreviations followed by the *Physics Abstracts* should be used. For periodicals not covered by *Physics Abstracts*, the title abbreviations should be according to the *Bibliographic Guide for Editors and Authors*, 1974, published by the American Chemical Society, Washington DC, USA; additionally the country from which the journal is published should be given in parenthesis immediately after the title abbreviation. If a paper has been accepted for publication, the names of the authors and the journal (with volume number and year, if known) should be given followed by the words "in press" [e.g. Wahi P K & Patel N D, *Can J Spectrosc (Canada)*, in press.]

In references containing up to four authors, the names of all the authors with their respective initials should be given. The abbreviations *et al.*, *idem* and *ibid* should be avoided. When there are more than four authors, only the names of the first three authors with their respective initials should be given, followed by the words '*et al.*'

Reference to a book should include details in the following order: name and initials of authors, the title of the book (underlined), name of publisher and place of publication within circular brackets and year and page (s) [e.g. Clayton G B, *Operational amplifiers* (Newnes-Butterworths, London), 4th Edn, 1977, 26]. If the reference is to the work of an author published in a book by a different person, the fact that it is cited from the source book should be clearly indicated [e.g. Turnhout Van J, 'Thermally stimulated discharge of electrets' in *Topics in applied physics*: Vol. 33—*Electrets*, edited by C M Sessler (Springer Verlag, Berlin), 1980, 130].

Proceedings of conferences and symposia should be treated in the same manner as books. Reference to a paper presented at a conference, the proceedings of which are not published, should include, in the following order, names and initials of authors, title of the paper (underlined), name of the conference, and where and when it was held (e.g. Herczeg P, *Symmetry-violating kaon decays*, paper presented to the International Conference on High Energy Physics and Nuclear Structure, Vancouver, Canada, 13-17 August 1979).

Reference to a thesis should include the name of the author, title of the thesis (underlined), university or institution to which it was submitted and year of submission (e.g. Mehrotra S N, *Many-body techniques and their applications to interacting bosons*, Ph D thesis, Ranchi University, 1976).

Reference to a patent should include names of patentees, country of origin (underlined) and patent number, the organization to which the patent has been assigned (within circular brackets), date of acceptance of the patent and reference to an abstracting periodical where available [e.g. Labes M M, *US Pat.* 4,066,567 (to Temple University), 3 January 1978; *Chem. Abstr.*, 88 (No. 20) (1978), 138350 n].

PROOFS & REPRINTS

Authors will receive galley proofs and a reprint order form. The galley proofs, indicating the essential corrections, should be returned to the Editor without delay, enclosing the reprint order form. Authors are given 25 free reprints for each paper. Extra reprints can be had at cost. If the reprint order is not received with the corrected proofs, it will be presumed that the author needs no extra reprints. Later requests for more reprints cannot be complied with. Covers for reprints cannot be provided.

THE WEALTH OF INDIA

An Encyclopaedia of Indian Raw Materials and Industrial Products, published in two series:
(i) Raw Materials, and (ii) Industrial Products.

RAW MATERIALS

The articles deal with Animal Products, Dyes & Tans, Essential Oils, Fats & Oils, Fibres & Pulps, Foods & Fodders, Drugs, Minerals, Spices & Flavourings, and Timbers and other Forest products. Names in Indian languages, and trade names are provided.

For important crops, their origin, distribution, evolution of cultivated types, and methods of cultivation, harvesting and storage are mentioned in detail. Data regarding area and yield and import and export are provided. Regarding minerals, their occurrence and distribution in the country and modes of exploitation and utilization are given. The articles are well illustrated. Adequate literature references are provided.

Eleven volumes of the series covering letters A-Z have been published.

Vol. I(A-B) Rs. 80.00; Vol. II (C) Rs. 95.00; Vol. III (D-E) Rs. 105.00; Vol. IV (F-G) Rs. 65.00; Vol. IV: Suppl. Fish & Fisheries Rs. 40.00; Vol. V (H-K) Rs. 75.00; Vol. VI (L-M) Rs. 90.00; Vol. VI: Suppl. Livestock Rs. 60.00; Vol. VII (N-Pc) Rs. 30.00; Vol. VIII (Ph-Re) Rs. 86.00; Vol. IX (Rh-So) Rs. 104.00; Vol. X (Sp-W) Rs. 152.00; Vol. XI (X-Z) Rs. 102.00.

INDUSTRIAL PRODUCTS

Includes articles giving a comprehensive account of various large, medium and small scale industries. Some of the major industries included are: Acids, Carriages, Diesel Engines, Fertilizers, Insecticides & Pesticides, Iron & Steel, Paints & Varnishes, Petroleum Refining, Pharmaceuticals, Plastics, Ship & Boat-building, Rubber, Silk, etc.

The articles include an account of the raw materials and their availability, manufacturing processes, and uses of products, and industrial potentialities. Specifications of raw materials as well as finished products and statistical data regarding production, demand, exports, imports, prices, etc., are provided. The articles are suitably illustrated. References to the sources of information are provided.

Nine volumes of the series covering letters A-Z have been published:

Part I(A-B) Rs. 54.00; Part II (C) Rs. 64.00; Part III (D-E) Rs. 25.00; Part IV (F-H) Rs. 25.00; Part V (I-L) Rs. 30.00; Part VI (M-Pi) Rs. 28.00; Part VII (Pl-Sh) Rs. 60.00; Part VIII (Si-Ti) Rs. 66.00; Part IX (To-Z) Rs. 80.00.

HINDI EDITION: BHARAT KI SAMPADA—PRAKRITIK PADARTH

Vols. I to VI and two supplements of Wealth of India—Raw Materials series in Hindi already published.

Published Volumes:

Vol. I (अ-ओ) Rs. 38; Vol. II (क) Rs. 36; Vol. III (ख-न) Rs. 36; Vol. IV (प) Rs. 83; Vol. V (फ-मेरे) Rs. 60; Vol. VI (मेरल-रु) Rs. 80.

Supplements:

Fish & Fisheries (Matsya & Matsyaki) Rs. 49;
Livestock (Pashudhan aur Kukkut Palan) Rs. 34.

Vols. VII to XI under publication.

Please contact:

Manager (Sales & Advertisement)

PUBLICATIONS & INFORMATION DIRECTORATE, CSIR
Hillside Road, New Delhi 110012

CSIR PUBLICATIONS

WEALTH OF INDIA

An encyclopaedia of the economic products and industrial resources of India issued in two series

RAW MATERIALS SERIES—contains articles on plant, animal and mineral resources

	Rs	\$	£
Vol. I (A-B)	80.00	30.00	13.00
Vol. II (C)	95.00	33.00	17.00
Vol. III (D-E)	105.00	32.00	20.00
Vol. IV (F-G)	65.00	27.00	12.00
Supplement (Fish & Fisheries)	40.00	16.00	7.00
Vol. V (H-K)	75.00	28.00	12.50
Vol. VI (L-M)	90.00	34.00	15.00
Supplement (Livestock)	60.00	18.00	6.00
Vol. VII (N-Pe)	30.00	9.00	3.00
Vol. VIII (Ph-Re)	86.00	32.00	14.00
Vol. IX (Rh-So)	104.00	35.00	19.00
Vol. X (Sp-W)	152.00	65.00	23.00
Vol. XI (X-Z)	102.00	42.00	20.00

INDUSTRIAL PRODUCTS SERIES—deals with major, small-scale and cottage industries

	Rs	\$	£
Part I (A-B)	54.00	20.00	9.00
Part II (C)	64.00	24.00	11.00
Part III (D-E)	25.00	7.50	2.50
Part IV (F-H)	25.00	7.50	2.50
Part V(I-L)	30.00	9.00	3.00
Part VI (M-Pi)	28.00	8.00	2.80
Part VII (Pi-Sh)	60.00	18.00	6.00
Part VIII (Si-Ti)	66.00	27.00	10.00
Part IX (To-Z)	80.00	34.00	12.00

BHARAT KI SAMPADA (Hindi Edition of Wealth of India, Raw Materials):

	Rs	\$	£
Vol. I (अ-ओ)	38.00	16.00	6.50
Vol. II (क)	36.00	15.00	6.00
Vol. III (ख-न)	36.00	15.00	6.00
Vol. IV (प)	83.00	34.00	16.00
Vol. V (फे-मेरे)	60.00	22.00	10.00
Vol. VI (ये-ल-ह)	80.00	27.00	13.00
Livestock (Kukkut Palan)	34.00	15.00	6.00
Fish & Fisheries (Matsya aur Matsyaki)	49.00	21.00	8.00
A Dictionary of Generic & Specific Names of Plants and Animals Useful to Man with their English and Latin pronunciation in Devanagari.	30.00	11.00	5.00

OTHER PUBLICATIONS

	Rs	\$	£
Proceedings seminar on primary communications in Science & Technology in India by Sh. R.N. Sharma & S. Seetharama	52.00	17.50	9.00
Flora of Delhi by J.K. Maheshwari	28.00	8.00	2.80
Indian Fossil Pteridophytes by K.R. Surange	23.00	8.00	2.30
Indian Thysanoptera by T.N. Ananthakrishnan	26.00	8.00	2.60
The Millipede Thyropygus by G. Krishnan	12.00	3.50	1.20
Drug Addiction with special reference to India by R.N. Chopra & I.C. Chopra	12.00	3.50	1.20
Glossary of Indian Medicinal Plants by R.N. Chopra & I.C. Chopra	35.00	13.00	6.00
Fluidization & Related Processes	12.00	4.00	1.20
Evolution of Life by M.S. Randhawa, A.K. Dey, Jagjit Singh & Vishnu Mitre	22.50	7.00	2.25
Collected Scientific Papers of Meghnad Saha	30.00	9.00	3.00
Proteaceae by C. Venkata Rao	34.00	11.00	3.40
Pinus by P. Maheshwari & R.N. Konar	30.00	11.00	5.00
Cellulose Research I	3.00	0.90	0.30
Cellulose Research II	6.00	1.75	0.60
Chemical Process Design	9.00	2.50	0.90
Low Temperature Carbonization of Non-coking Coals & Lignites & Briquetting Coal Fines:			
Vol. I	17.50	5.50	1.75
Vol. II	17.50	5.50	1.75
Nucleic Acids	10.00	3.00	1.00
IGY Symposium: Vol. I	9.00	2.50	0.90
IGY Symposium: Vol. II	9.00	2.50	0.90
CNS Drugs	16.50	5.00	1.65
Kinetics of Electrode Processes & Null Points of Metals	2.50	0.75	0.25
Indian Sardines by R.V. Nair	22.00	7.00	2.20
Termite Problems in India	9.00	3.00	0.90
Loranthaceae by B.M. Johri & S.P. Bhatnagar	32.00	11.00	3.20
Abies and Picea by K.A. Chowdhury	14.00	6.00	2.10
Gnetum by P. Maheshwari and Vimla Vasil	20.00	6.00	2.00
Aquatic Angiosperms by K. Subramanyam	20.00	6.00	2.00
Supplement to Glossary of Indian Medicinal Plants by R.N. Chopra, I.C. Chopra & B.S. Varma	18.00	7.00	3.00
Herbaceous Flora of Dehra Dun by C.R. Babu	144.00	60.00	22.00
Diosgenin and Other Steroid Drug Precursors by Y.R. Chadha & Miss L.V. Asolkar	36.00	13.00	6.00
Research & Development Management by Inder Dev	25.00	10.00	—
Rural Development and Technology—A Status Report-cum-Bibliography by P.R. Bose & V.N. Vashist	100.00	38.00	17.00

Packing and Postage extra

Please contact:

Manager (Sales & Advertisement)

PUBLICATIONS & INFORMATION DIRECTORATE, CSIR

Hillside Road, New Delhi 110012